DISSERTATION

SODIUM LIDAR OBSERVED VARIABILITY IN MESOPAUSE REGION TEMPERATURE AND HORIZONTAL WIND: PLANETARY WAVE INFLUENCE AND TIDAL-GRAVITY WAVE INTERACTIONS

Submitted by
Tao Li
Department of Physics

In partial fulfillment of the requirements
For the Degree of Doctor of Philosophy
Colorado State University
Fort Collins, Colorado
Summer 2005

COLORADO STATE UNIVERSITY

July 7, 2005

WE HEREBY RECOMMEND THAT THE DISSERTATION PREPARED UNDER OUR SUPERVISION BY TAO LI ENTITLED "SODIUM LIDAR OBSERVED VARIABILITY IN MESOPAUSE REGION TEMPERATURE AND HORIZONTAL WIND: PLANETARY WAVE INFLUENCE AND TIDAL-GRAVITY WAVE INTERACTIONS" BE ACCEPTED AS FULFILLING IN PART REQUIREMENTS FOR THE DEGREE OF DOCTOR OF PHILOSOPHY.

Committee on Graduate Work

John Harton

Han-Li Liu

M T Montgomery
Michael Montgomery

David A. Krueger
Co-Advisor David A. Krueger

Chiao-yao She
Advisor Chiao-Yao She

David A. Krueger
Department Head David A. Krueger

ABSTRACT OF **DISSERTATION**

SODIUM LIDAR OBSERVED VARIABILITY IN MESOPAUSE REGION TEMPERATURE AND HORIZONTAL WIND: PLANETARY WAVE INFLUENCE AND TIDAL-GRAVITY WAVE INTERACTIONS

The CSU sodium lidar system at Fort Collins, CO (40.6N, 105W), after a decade of mesopause temperature observation was upgraded in 1999 from a one-beam system to a two-beam system, capable of simultaneous and continuous observations of mesopause region temperature, zonal wind, and meridional wind, over full diurnal cycles, weather permitting. The regular observation under this operation mode started in May 2002. The valuable datasets could be used to study not only the tidal day-to-day variability but also planetary waves and gravity waves.

Analysis of our longest dataset near fall equinox in 2003 (September 2003 campaign) reveals the dramatic tidal day-to-day variability with 2-fold increase in tidal amplitudes in all three fields during UT day 267 and 268. Further TIME-GCM (Thermosphere-Ionosphere-Mesosphere-Electrodynamics General Circulation Model) study and comparison between lidar observed temperature and the SABER observed global temperature field suggest that both tidal/planetary wave interactions and tidal/gravity wave interactions play an important role for the tidal amplitude enhancement. Though detailed causes for tidal variability require further study, we have demonstrated that substantial information on MLT dynamics may be obtained from a comprehensive long-period data set. Three near 80hr continuous datasets in consecutive summers of 2002, 2003, 2004 give us the opportunities to study summer quasi-two-day waves (QTD) with the possible modulation of Quasi-Biannual Oscillation (QBO) on QTD wave amplitude. Comparisons between the QTD wave amplitudes of temperature observed by lidar and SABER for all three campaigns show very good agreement. A strong winter mesospheric temperature inversion layer (MIL) was observed by our sodium lidar in December 2004 campaign. Studies of this event reveal the strong MIL which is consistent with mean state and tidal/gravity wave interactions. The observed dramatic tidal amplitude increase in day 338 is the result of such wave-wave interactions.

Tao Li
Department of Physics
Colorado State University
Fort Collins, CO 80523
Summer 2005

Acknowledgement

Firstly, I would like to express my appreciation to my advisor, Chiao-Yao (Joe) She and my co-advisor, David A. Krueger for their guidance, support, encouragement during the past four years. They developed a model of dedication and enthusiasm to the lidar research at Colorado State University. Many thanks are also given to Joe's wife, Lucy for the delicious Chinese foods, and Dave's wife, Mini, for the delicious disserts.

Secondly, I would like to thank all the lidar group members, Dr. Bifford P. Williams, Dr. Joe D. Vance, Dr. Tao Yuan, Mr. Philip Acott, Mr. Jia Yue, and Mr. Sean Harrell for their contributions to this dissertation.

Thirdly, I would like to thank all the committee members, Dr. John Harton, Dr. Hanli Liu, Dr. Mike Montgomery, and Dr. Azer Yalin for their help to meet the graduate school deadlines and to improve this dissertation considerably.

Fourthly, I thank our colleagues, Dr. Chris Mertens at NASA for providing TIMED/SABER data, and Dr. Scott Palo at University of Colorado and Dr. Qian Wu at National Center for Atmospheric Research for providing August quasi-two-day wave plots, respectively from SABER temperatures and TIDI winds .

Finally, I would like to thank my family, especially to my wife, Jia Hu, my newborn son, Andrew H. Li, my father, Daochun Li, my mother, Nanying Tao, my father-in-law, Huanling Hu, and my mother-in-law, Xiangshuang Qiu, for their endless support for my education, which makes this research and dissertation possible.

Table of Contents

List of Figures:

Figure 2.11 Schematic diagram of Faraday Filter.

Figure 2.12 Measured transmission function of Faraday Filter

Figure 2.13 Schematic diagram of electronics and timing subsystem. The red dash lines denote the BNC cables and blue solid lines denote 9-pin connector connecting NI BNC-2090 board with PLD box. Connectors pointed by red and blue arrows are input. Connectors without arrow pointing are output. NI BNC-2090 board is connected with a DAQ-6024E card in the Labview computer.

Figure 2.14 Timing diagram for most of the signals with corresponding pulse frequency and width. The blue number to the left of each signal is used to number the BNC connected to the signal in question.

Figure 2.15 schematic diagram of synchronization. Black solid lines denote the BNC cables. Blue solid thin lines denote the 9 pins from PLD box to BNC-2090 board.

Figure 2.16 Schematic diagram of the BNC connectors on the front panel of PLD box. Red connectors represent input, and blue connectors represent output. Connectors and associated BNC cables are labeled by number for easily checking purpose

Figure 2.17 Schematic timing diagram of Spectra-Physics pulse Nd:YAG laser [Spectra-Physics Nd:YAG laser manual]

Figure 2.18 Schematic diagram of Programmable Logic Device chirp with three inputs and three outputs. Red connectors are inputs in the left side. Blue connectors are outputs in the right side. Green box denotes the whole chip including two logic units for different logic purposes.

Figure 3.1 Energy-level diagram of atomic sodium in three different models. Basic Model is only a two-level system. In intermediate model, the electron spin is included, and the excited state is split to 2 levels. The final model includes the nuclear spin interactions, which gives a hyperfine splitting of the energy-levels. [She and Yu, 1995]

Figure 3.2 Na D_2 absorption spectrum with (a) various temperatures for radial wind velocity = 0m/s, and (b) various radial wind velocities for temperature = 200K. Arrows mark the positions of D_{2a} peak, D_{2b} peak and Crossover. Vertical lines point out the 630MHz downshift and upshift frequencies from D2a peak. CSU lidar system will transmit laser beam into atmosphere at these 3 frequencies.

Figure 3.3 Absorption Cross sections of sodium D2 transition. Solid line is calculated from Voigt functions which include the effects of Doppler broadening and natural line broadening. Dash line is approximately calculated from Gaussian function.

Figure 3.4 2D calibration curves constructed from numerical calculations. The temperature and wind ratios are both theoretical computed from spectrum of laser induced sodium fluorescence. Solid lines are calculated from exact spectrum of Voigt function, whereas the dash lines are calculated from approximate spectrum of Gaussian function. Calibration curves may be used to retrieve temperature and radial wind velocity by using the experimental temperature and wind ratios.

Figure 3.5 Vertical profiles of raw photons with 2-minute integration (a) at nighttime and (b) at daytime. Three colors represent three frequencies with green for D2a peak, blue for +630MHz, and red for -630MHz. Daytime profiles are much noisier than nighttime profiles due to higher background in the daytime even using Faraday filter to dramatically reduce the skylight background. At the same time, the Faraday filter decreases the return signal by a factor of 4.

Figure 4.1 the plot of eigenvalue ε_n of wave modes of zonal wave number s = 1 vs. normalized frequency σ/Ω. Waves with positive (negative) frequencies propagate eastward (westward). Figure adapted from Volland [1988].

Figure 4.2 Symmetric Hough functions for migrating solar diurnal tides. (Adapted from Lindzen [1967])

Figure 4.3 Perturbation vorticity field and induced velocity field (dashed arrows) for a sinusoidal displacement of a chain of fluid parcels from its mean latitude. Heavy wavy line denotes original perturbed position; light line denotes the westward displacement caused by advection of the pattern by the induced meridional velocity field. Positive sign means the induced vorticity points out of paper, visa versa. (Taken from Holton and Alexander [2000])

Figure 5.1 Contour plots of temperature, zonal wind, and meridional wind observed by CSU sodium lidar between UT day 264 and UT day 272 of 2003. Diurnal and semidiurnal oscillations are clearly shown in all three fields with downward phase progression. Day-to-day variability of tides can also be clearly seen with tidal enhancement on UT day 267 and 268.

Figure 5.2a Vertical profiles of diurnal tidal amplitudes and phases of temperature, zonal wind, and meridional wind in the mesopause region for both 9-day continuous dataset and 14-day duration datasets. The predictions of both GSWM00 and GSWM02 are also plotted for comparison.

Figure 5.2b Vertical profiles of semidiurnal tidal amplitudes and phases of temperature, zonal wind, and meridional wind in the mesopause region for both 9-day continuous dataset and 14-day duration datasets. The predictions of both GSWM00 and GSWM02 are also plotted for comparison.

Figure 5.3 Normalized Lomb power contours of temperature, zonal wind, meridional wind based on the 9-day continuous dataset are shown with the contour lines corresponding to 0.1% (solid line) and 1% (dot line) probability resulting from random noise marked..There is only a $1\text{x}10^{-5}\%$ probability that a Lomb power of 20 would be generated by Gaussian noise for our observation times and the frequencies investigated.

Figure 5.4 Filtered meridional wind contours by a band-pass filter with sharp cutoffs at 30 and 200 hours.

Figure 5.5 Variability in diurnal (a, b, c) and semidiurnal (d, e, f) amplitudes (top) and phases (bottom) of temperature (a, d), zonal wind (b, e), and meridional wind (c, f) during 9-day observation. Notice scale differences.

Figure 5.6 Semidiurnal tidal amplitude and phase variability of the temperature, zonal wind, and meridional wind at 94km during 9-day continuous observation.

Figure 5.7 the time series change of vertical profiles of temperature (upper panel), zonal wind (middle panel), and meridional wind (bottom panel) with vertical resolution of 2km and temporal resolution of 15min for nighttime and 30min for daytime in UT day 267. Red and blue lines alternate in time. Note that 1 day is scaled to 200K for temperature and 500m/s for wind.

Figure 5.8 the time series change of vertical profiles of temperature (upper panel), zonal wind (middle panel), and meridional wind (bottom panel) with vertical resolution of 2km and temporal resolution of 15min for nighttime and 30min for daytime in UT day 268. Note that 1 day is scaled to 200K for temperature and 500m/s for wind.

Figure 5.9 the SABER latitude versus longitude orbit for UT day 267

Figure 5.10 the vertical temperature profiles of lidar (blue solid line) and SABER (red dot line) at UT time around UT 8:00am (LT 1:00am)

Figure 5.11 Contour plots of longitudinal distribution of SABER ascending and descending temperature by averaging over 10° of latitude from 35°N to 45°N in UT day 267.

Figure 5.12 SABER footprint Over America continents (left panel) in UT day 267 and Contour plots of latitudinal distribution of SABER temperature for one ascending orbits marked as red dots and one descending orbits marked as blue dots.

Figure 5.13 Contour plots of longitudinal distribution of SABER ascending and descending temperature by averaging over 10° of latitude from 35°N to 45°N in UT day 268.

Figure 5.14 SABER footprint Over America continents (left panel) in UT day 268 and Contour plots of latitudinal distribution of SABER temperature for one ascending orbits marked as red dots and one descending orbits marked as blue dots.

List of Tables:

Chapter 1: Introduction

In this chapter, lidar remote sensing for atmospheric research will be reviewed followed by the description of science in the mesopause region (80-105km), where the temperature, zonal wind, and meridional wind can be observed simultaneously for more than 24hr continuously by the CSU sodium lidar system at Fort Collins, CO (40.5N, 105W). The CSU sodium lidar has been developed for more than 15 years since the first observation in 1989 [She, 1990]. The history of lidar research at Colorado State University follows. Finally, the structure of this thesis will be listed according to different chapters.

1.1 Lidar remote sensing for atmospheric research

LIDAR is an acronym for LIght Detection And Ranging, using electromagnetic waves in the visible or near-visible spectrum to remotely investigate properties of a medium [Measures, 1984]. Since it is the optical equivalent of the microwave radar, lidar is often referred to as laser radar. Generally, the lidar transmits a pulse of laser light into atmosphere, and selected information along the path of laser beam may be retrieved from the backscattered signals which are collected by a telescope, measured by a photodetector, and digitized using a computer/recording system. The time for the light to travel out to the scatterers and back to the lidar is used to determine the range to the scatterers. Currently there are several types of lidar systems used for atmospheric study, such as DIAL Lidar (Differential Absorption Lidar), Resonant Fluorescence Lidar, Mie (aerosol) lidar, Raman Lidar, Rayleigh Lidar, and Doppler Lidar [Grant et al., 1997].

DIAL lidar is used to measure chemical concentrations (such as ozone, water vapor, pollutants) in the atmosphere. A DIAL lidar uses two different laser wavelengths which are selected so that one of the wavelengths is absorbed by the molecule of interest whereas the other wavelength is not. The difference in intensity of the two return signals can be processed to deduce the range resolved concentration of the molecule being investigated [Schotland, 1964]. Resonant Lidar system is used to detect the fluorescence from naturally occurring metal species (Na, K, Fe, Ca, etc.) to deduce the density of species as well as winds and temperature in the mesopause region between 80km and 105km. The CSU Lidar system is a sodium resonant fluorescence lidar system, which can be used to determine Na density, temperature, zonal wind and meridional wind in the mesopause region of the atmosphere [She et al., 2004]. Raman scattering is light scattered by molecules, where the wavelength is changed by the scattering. The change in wavelength depends on the temperature of the air and the type of molecule from which the scattering takes place. The Raman lidar technique has become a standard procedure for nighttime ground-based measurement of water vapor up to 8 km and daytime up to 3 km [Whiteman et al., 1992]. Rayleigh scattering is simply light scattering by molecules, where the wavelength is essentially unchanged. The Rayleigh Lidar technique is used to study the thermal structure of the middle atmosphere through the creation of density and temperature profiles [Kent and Wright, 1970]. Doppler lidar is used to measure the velocity of a scatterer. When the light transmitted from the lidar hits a scatterer moving towards or away from the lidar, the wavelength of the light backscattered off the scatterer will be changed slightly. The atmosphere contains many microscopic dust and aerosol particles which are carried by the wind. These are the targets of interest to us as they are small and light enough to move at the true wind velocity and thus enable a remote measurement of the wind velocity [Huffaker et al., 1970].

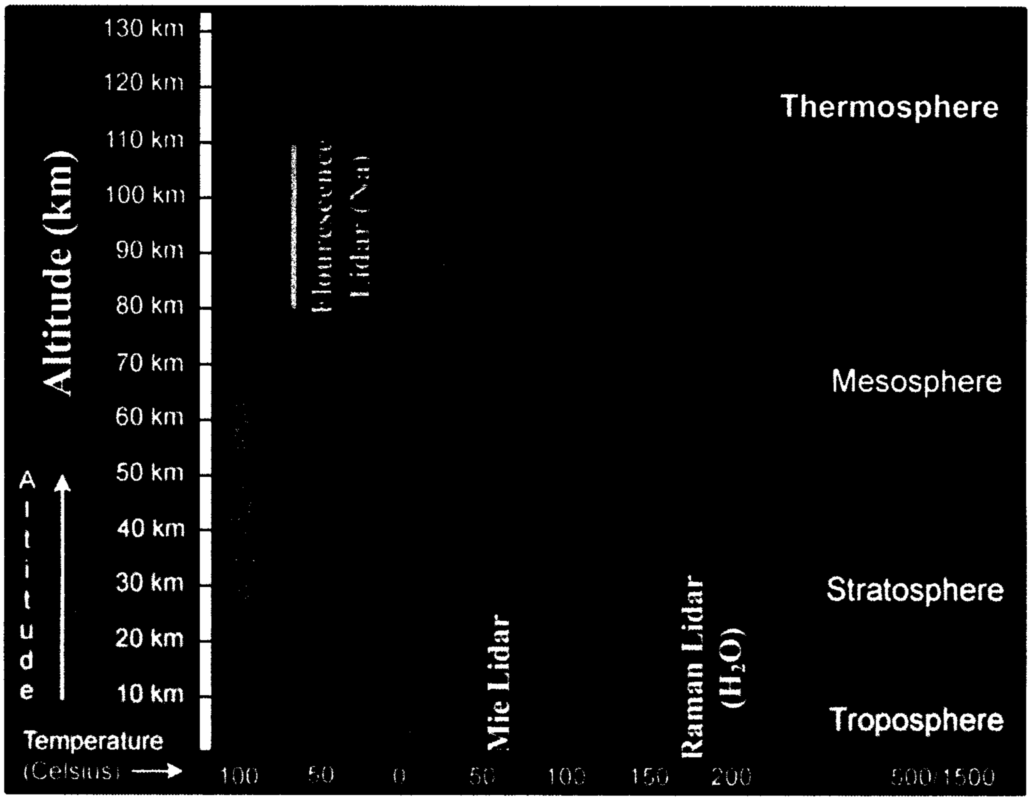

Figure 1.1 Temperature vertical profile from ground to the thermosphere with applicable altitude ranges for different lidar systems.

Shown in figure 1.1 is the plot of the temperature vertical profile from ground to the thermosphere with applicable altitude ranges for different lidar systems. According to the temperature structure, the atmosphere is divided into different layers. The measurement range of Rayleigh lidar system can be extended beyond 80km dependent on the power of transmitter, the size of receiving telescope, and the integration time interval. Due to exponential decrease of the air density and 15 orders smaller cross section of Rayleigh scattering compared to that of resonant scattering, Rayleigh lidar is almost impossible to use to study the dynamics in the mesopause region [She, 2004]. Therefore, we can only depend upon resonance scattering (or laser induced fluorescence) to probe atmospheric temperature and wind in the mesopause region. The resonant fluorescence lidar can use a relatively small telescope and weak output power to achieve the necessary signal-to-noise ratio to obtain accurate temperature and winds. But we will see in the chapter 2, the electronics control system and transmitter system of our lidar system is much more complicated than other types of lidar systems.

Lidars are valuable instruments for atmospheric research because they provide an active remote sensing technique that can probe atmospheric regions inaccessible to other instruments at high spatial and temporal resolution [Grant et al, 1997]. Lidars operating from ground and space provide complementary information: where satellite-borne lidars provide global coverage but at lower horizontal resolution, ground-based instruments reveal the fine detail required for atmospheric process research.

1.2 Mesopause region (80-105km)

The mesopause region of the atmosphere lies between 80km and 105km where the temperature is lowest in the Earth's atmosphere. The temperatures in this region vary in seasons with warmer in the winter and cooler in the summer, suggesting that the heating source is not solar flux but rather dynamical or chemical processes [She et al., 1995; She and Von Zahn, 1998]. All the wave types, including gravity waves, tides, and planetary waves, are most important for the dynamic processes in the mesopause region. The gravity waves propagating into the region from the lower atmosphere dissipate, depositing their energy and momentum and drive a residual circulation from the summer to winter hemispheres with upwelling and downwelling over the respective poles [Fritts et al., 2003]. Large and ubiquitous solar atmospheric tidal variations characterize the large-scale dynamics near the mesopause region. The thermosphere-ionosphere-mesosphere electrodynamics general circulation model (TIME-GCM) [Roble et al., 1994] reveals that the mesopause region is extremely sensitive to thermal, chemical, and dynamical forcing originating at lower levels. For example, a doubling of CO_2 and CH_4 can produce temperature reductions (due to CO_2 radiative cooling at 15μm) of 5-10°C in the mesosphere and 10-20°C in the lower thermosphere, as compared to less than 1°C changes near the earth's surface.

There exists the layer of atomic metals (e.g. Na, K, Ca, Fe…) in the mesopause region which are most likely due to the vaporization of meteors when they enter the earth’s atmosphere. The peak density of these neutral Na atoms of 10^9 to 10^{10} m^{-3} typically occurs around 92km, providing an ideal tracer for fluorescence measurements in this region of the atmosphere [She, 1990]. Sodium lidar system takes the advantage of the large fluorescence cross-sections of sodium atoms in the visible spectrum, and is capable of precision measurements of sodium density, temperature, and winds, which are the most important parameters for studying the dynamics in the mesopause region.

1.3 Sodium Lidar research at Colorado State University

In 1989, Colorado State's first Sodium resonance lidar with two-frequency setup for the measurements of temperature and sodium density in the mesopause region was constructed in collaboration with scientists from the University of Illinois [She et al., 1990; Bills et. al., 1991]. The routine observations for temperature and sodium density in two-frequency mode were started afterwards, followed by introduction of a third frequency using an acousto-optic modulator for measurement of wind in the mesopause region by Yu [1994]. The daytime operation under sunlit condition was achieved by using a Faraday Filter in 1996, along with the first 24-hour observations of temperature and density above Fort Collins [Chen et. al., 1996]. The tidal studies based on many campaigns of 24 or more hours were conducted by S. Chen [1999]. A frequency monitor based on an iodine optical absorption cell for correcting the observed wind velocity was first added to the lidar transmitter by White [1999], and further improved by Sherman [2002]. The system was upgraded with two-beam setup in 1999, and then the nighttime simultaneous T, U, V measurements were started. In 2002, the stability of the Faraday filters was improved by Yuan [2004], making the filters robust enough for long-period observations.

The CSU sodium lidar system at Fort Collins, CO, after a decade of mesopause temperature observation [She et al., 2000], was upgraded from a one-beam system to a two-beam system, capable of simultaneous and continuous observations of mesopause region temperature, zonal wind, and meridional wind, over full diurnal cycles, weather permitting. Regular observations in this mode of operation began May, 2002. By the end of summer 2005, our sodium lidar will have 3 years of good day-night datasets. Using these datasets, we could study not only the seasonal variations of tides, but also the tidal day-to-day variability as well as planetary waves and gravity waves. In September 2003, an unusually long dataset of 14-day duration was acquired between Sep 18 and Oct 01 including a 9-day continuous observation [She et al., 2004]. This dataset is very valuable for study the tidal day-to-day variability, tidal/planetary and tidal/gravity wave nonlinear interactions, which will be discussed in details in chapter 5. In addition, the concurrent observations of a mesospheric bore by OH imager and sodium lidar suggests, for the first time, that atmospheric dynamic instability is associated with the a transition of an undular mesospheric bore to a turbulent bore [She et al., 2004]. Concurrent OH imager and sodium temperature/wind lidar observation of localized ripples [Li et al., 2005] not only confirmed that ripples are indeed signatures of atmospheric instability but also provide a meaningful association with current theoretical simulations [Fritts et al., 1996].

1.4 Structure of this thesis

Chapter 2 discusses the details of the CSU sodium lidar system setup, and provides the overview on the lidar transmitter subsystem, receiving subsystem, and control and timing electronics subsystem. The description of these subsystems is concentrated on their functionality.

Chapter 3 briefly and qualitatively discusses atomic sodium hyperfine spectrum. The discussion mainly focuses on the concepts necessary to understand the 3-frequency lidar measurements of temperature and wind. Then the lidar equation for a sodium lidar system follows. The calculations of theoretical temperature and wind ratios as well as 2-D calibration curve are presented. The procedures used in the data analysis for converting returned fluorescence photon counts into temperature and wind profiles are discussed in the end of this chapter.

Chapter 4 presents brief reviews of the atmospheric solar tides, planetary waves, and gravity waves, as well as their interactions.

Chapter 5, the kernel of this thesis, firstly presents the dramatic tidal day-to-day variability based on our longest campaign (14 day duration with 9-day continuous observation) near fall equinox. The tidal/planetary wave interactions and tidal/gravity waves interaction are discussed in details related to tidal variability. TIME-GCM modeling for tidal/planetary wave interactions is also discussed. Then we present our 3 August datasets respectively in 2002, 2003, and 2004. The considerable tidal day-to-day variability was observed along with the significant two-day wave activities. Observations of two-day waves by our lidar and SABER on board TIMED satellite are in good agreement. Finally in this chapter, the observed strong winter temperature inversion is discussed. The related causes of the strong temperature inversion are also presented as well as the tidal day-to-day variability.

Chapter 6 provides a brief conclusion with possible future work.

Reference:

Bills, R. E., C., S. Gardner, and C. Y. She, Narrowband Lidar Technique for Sodium Temperature and Doppler Wind Observations of the Upper Atmosphere, *Opt. Eng.*, 30, 13-21, 1991.

Byer, R. L., Remote air pollution measurement. Opt. Quant. Electron., 7, 147-177, 1975.

Chen, H., M. A. White, D. A. Krueger, and C. Y. She, Daytime Mesopause Temperature Measurements using a Sodium-Vapor Dispersive Faraday Filter in a Lidar Receiver, *Opt. Lett.*, 21, 1093-1095, 1996.

Chen, H., A Sodium Fluorescence Lidar for Daytime Operation Using a Dispersive Faraday Filter, *PhD Dissertation*, Colorado State University, 1997.

Chen, S., 24 Hour Lidar Campaigns and Tidal Analysis, *PhD Dissertation*, Colorado State university, 1999.

Collis, R. T. H., and E. E. Uthe, Mie scattering techniques for air pollution measurement with lasers, Opto-electronics, 4, 87-99, 1972.

Fritts, D. C., J. F. Garten, Ø. Andreassen (1996), Wave breaking and transition to turbulence in stratified shear flows, *J. Atmos. Sci.* 53, 1057-1085.

Fritts, D. C., and M. J. Alexander, Gravity wave dynamics and effects in the middle atmosphere, *Rev. Geophys.*, 41(1), 1003,doi:10.1029/2001RG000106, 2003.

Grant, William B., Edward V. Browell, Robert T. Menzies, Kenneth Sassen, Chiao-Yao She, Volume MS 141, p. xiii – xxiv, 1997Selected Papers on Laser Applications in Remote Senssing, SPIE Milestone Series.

Huffaker, R. M., A. V. Jelalian, J. A. L. Thomson, Laser-Doppler System for Detection of Aircraft Trailing Vortices, *Proceedings of the IEEE*, 58(3), 322-326, 1970.

Kent, G. S., R. W. H. Wright, A review of laser radar measurements of atmospheric properties, J. Atmos. Terr. Phys., 32, 917-943, 1970.

Li, T., C. Y. She, B. P. Williams, T. Yuan, R. L. Collins, L. Kieffabar, and A. Peterson, Concurrent OH imager and sodium temperature/wind lidar observation of localized ripples over Northern Colorado, *J. Geophys. Res.*, in press, 2005.

Measures, Raymond M., Laser remote sensing: fundamentals and applications, New York, Wiley, 1984.

Roble, R., E. C. Ridley, A Thermosphere-Ionosphere-Mesosphere-Electrodynamics General Circulation Model (TIME-GCM), *Geophys. Res. Lett.*, 21, 417-420, 1994.

Schotland, R. M., The Determination of the Vertical Profile of Atmospheric Gases by Means of a Ground Based Optical Radar, *Proceedings of the Third symposium on Remote sensing of the Environmental*, October 1964 (University of Michigan, Ann Arbor, 1965).

She, C. Y., Remote Measurements of Atmospheric Parameters: New Applications of Physics with Lasers, *Contemp. Phys.*, 31, 247-260, 1990.

She, C. Y., J. R. Yu, D. A. Krueger, R. Roble, P. Keckhut, A. Huchecorne, M-L. Chanin, Vertical Structure of the Midlatitude Temperature From Stratosphere to Mesopause (30-105km), *Geophys. Res. Lett.*, 22, 377-380, 1995.

She, C. Y., S. S. Chen, Z. L. Hu, J. Sherman, J. D. Vance, V. Vasoli, M. A. White, J. R. Yu, and D. A. Krueger, Eight-year climatology of nocturnal temperature and sodium density in the mesopause region (80 to 105 km) over Fort Collins, CO (41oN, 105oW), *Geophys. Res. Lett.*, 27, 3289 – 3292, 2000.

She, C. Y., Optical Processes and Spectroscopy for atmospheric monitoring, notes of PH793BV (Seminar: Laser Spectroscopy/Quantum Electronics), Spring 2004.

She, C. Y., T. Li, B. P. Williams, T. Yuan, and R. H. Picard, Concurrent OH imager and sodium temperature/wind lidar observation of a mesopause region undular bore event over FortCollins/Platteville, Colorado, *J. Geophys. Res.*, 109, D22107, doi:10.1029/2004JD004742, 2004.

She, C. Y., T. Li, R. L. Collins, T. Yuan, B. P. Williams, T. Kawahara, J. D. Vance, P. Acott, D. A. Krueger, H.-L. Liu and M. E. Hagan, Long-period lidar observation of mesopause region temperature and wind vector over Ft. Collins, CO (40°N, 105°): Study of tidal-period perturbation and variability, *Geophys. Res. Lett.*, 31, L24111, doi:10.1029/2004GL021165, 2004.

Sherman, J. P., Mesopause Region Thermal and Dynamical Studies Based on Simultaneous Temperature, Zonal and Meridional Wind Measurements with an Upgraded Sodium Fluorescence Lidar, *PhD Dissertation*, Colorado State University, 2002.

Tipler, Paul A., 1969, Foundations of Modern Physics. In *The Quantization of Electricity, Light, and Energy* (New York: Worth Publishers, Inc.). pp. 103-144.

White, M. A., A Frequency-agile Na Lidar for the Measurement of Temperature and Velocity in the Mesopause Region, *PhD Dissertation*, Colorado State University, 1999.

Whiteman, D. N., S. H. Melfi, and R. A. Ferrare, Raman lidar system for the measurement of water vapor and aerosols in the Earth's atmosphere, *Appl. Opt.*, 31, 3068-3082, 1992.

Yu, J. R., A Sodium Wind/Temperature Lidar and Observed Mesopause Thermal Structure over Fort Collins, CO, *PhD Dissertation*, Colorado State University, 1994.

Yuan, T., Seasonal variations of Diurnal and semidiurnal tidal-period perturbations in mesopause region temperature and zonal and meridional winds above Ft. Collins, CO (40°N, 105°W) based on Na-Lidar observation over full diurnal cycles, *PhD Dissertation*, Colorado State University, 2004.

Chapter 2: Colorado State University Sodium Lidar System

The Colorado State University sodium lidar system at Fort Collins, Colorado has been gradually improved and upgraded since its first light (observations) in August 1989 [She, 1990]. Currently this system is operating routinely in 3 frequencies with 2-beam setup to simultaneously observe temperature, zonal wind, and meridional wind in the mesopause region (80-105km) on 24hr continuous basis. Similar to all other lidar systems, the CSU sodium lidar system includes a transmitter subsystem, a receiver subsystem, and an electronics and timing subsystem. As a resonant fluorescence and high spectral resolution lidar system for simultaneous temperature/wind measurements, the CSU sodium lidar system requires a more complicated transmitter and electronics subsystems than other types of lidar systems.

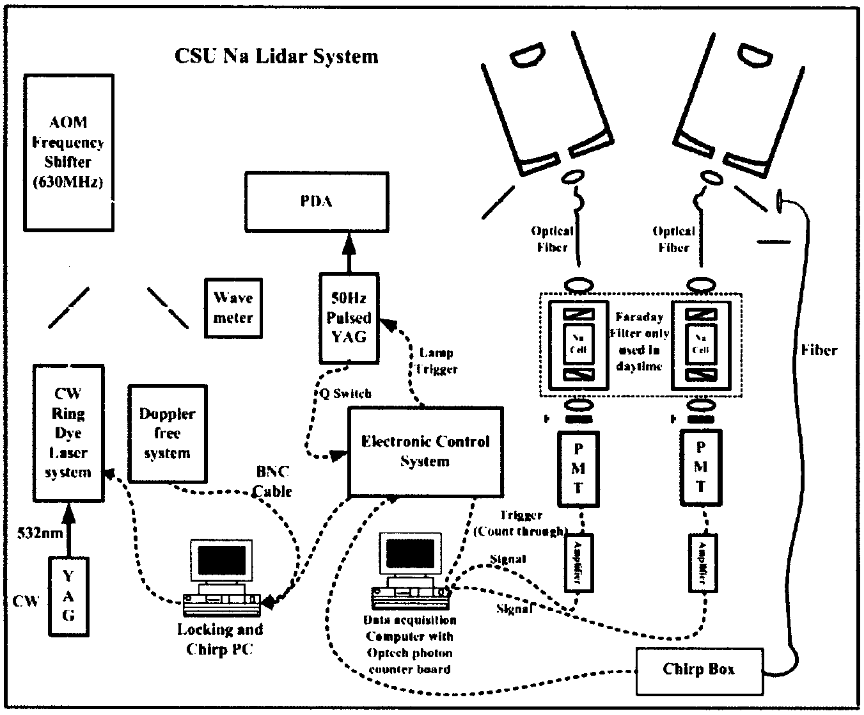

Figure 2.1 Schematic diagram of CSU sodium lidar system. Yellow lines with arrows denote laser beam with propagation direction. Black solid lines denote optical coupling fiber. Dash lines denote electronic connections.

This chapter will describe the CSU lidar system in details starting with the transmitter subsystem, followed by the receiver subsystem, finally by the electronics and timing subsystem. The description of these subsystems emphasizes their functionality. The schematic diagram of CSU sodium lidar system is shown in figure 2.1.

2.1 CSU sodium lidar transmitter subsystem

Sodium lidar observations of temperature and wind in the mesopause region depend upon measurements of relative lidar returns induced by 3 specified frequencies within the Doppler width of the Na D_2 transition, ν_0 = the sharpest feature in the D_{2a} transition, $\nu_+ = \nu_0 + 630$ MHz, $\nu_- = \nu_0 - 630$ MHz. The absolute value of these frequencies must be maintained, robust and stable throughput the course of lidar operation. Therefore to produce high quality laser beam with stability and high spectral resolution is the main challenge of the CSU sodium lidar system. Stringent requirements dictate that the lidar transmitter subsystem, in this case, uses three lasers, one pulse dye amplifier, a Doppler-free spectroscopy monitoring system for precision locking and control of the CW Ring laser frequency to the D_{2a} peak, ν_0, and an Acoustic Optic Modulator to produce the desired 3 frequencies, ν_0, ν_+ and ν_-. Figure 2.2 shows the schematic diagram of the lidar transmitter.

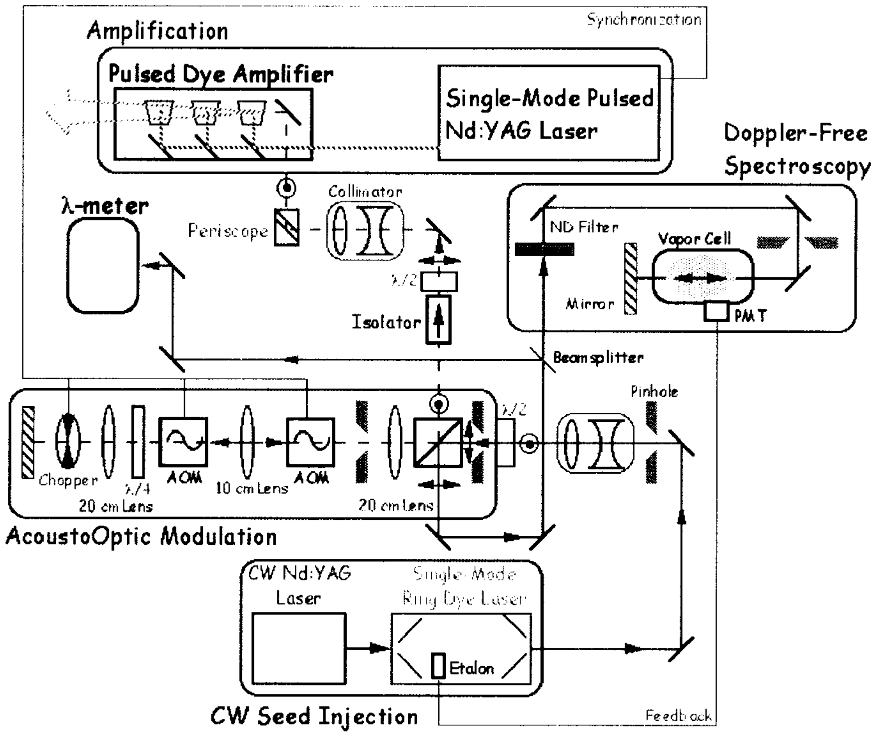

Figure 2.2 Schematic diagram of the CSU sodium lidar transmitter. A CW Ring Dye laser which is pumped by a CW Nd:YAG laser outputs a single mode beam. The Doppler-free spectroscopy is used to dynamically lock the laser frequency at c/589.158nm of sodium D2a peak. The acousto optic modulator shifts the CW seed frequency up and down by 630MHz and forms the frequency sequence of D2a peak, +630MHz, -630MHz. The CW seed beam is injected into a Pulsed Dye Amplifier, which is pumped by a single-mode pulse Nd:YAG, to generate amplified pulse beam (~1W) at seed frequencies.

2.1.1 CW lasers as seed injection

CW seed of the lidar transmitter consists of a pump laser of double-frequency CW Nd:YAG (Spectra Physics Millennia-V), which is operated at 532nm with regular output power of 3.5 to 4W, and a CW single-mode Ring Dye Laser (Coherent 899-21), which is the heart of lidar transmitter. The reference cavity of CW Ring Dye Laser provides the error signal for frequency stabilization to within 500 KHz rms. The cavity length of the 899-21 is actively stabilized by low-frequency corrections to the vertex Brewster plate and by high-frequency corrections to a PZT-mounted fold mirror (or tweezer). Generally, the CW Ring Dye Laser is able to generate a single-mode, narrow band (<1MHz) output beam with power up to 500mW and frequency tunable range of more than 20GHz. During routine data acquisition, the Ring Dye Laser is actively locked to the deepest Lamp-dip located at D_{2a} peak at ~589.159nm in the Doppler-free fluorescence spectrum. The detailed description of active locking will be discussed below.

2.1.2 Doppler-free system for absolute frequency locking

Since our sodium lidar system collects the backscattered photons of laser-induced fluorescence of sodium atoms in the mesopause region, the derivation of temperature and wind from return signals is highly dependent on the absolute laser frequencies. In order to determine the frequency of output laser beam from the ring dye laser to an accuracy of a few MHz, we use Doppler-free saturation spectroscopy [She and Yu, 1995] method involving a laboratory Na vapor cell which is heated to 70°C. Setup of the Doppler-free system is shown in figure 2.3.

When the sodium cell is maintained at typical temperature of 70°C, the sodium vapor density inside the cell is sufficient for easy detection. However the width of the sodium absorption spectrum due to Doppler broadening is about 1.4GHz at 70°C, which is too broad to be used as frequency reference to lock the ring laser frequency [She et al., 1992]. Fortunately, the Doppler-free saturation spectrum provides us the unique Lamp-dip feature at D_{2a} peak which is ideally suitable for actively and stably locking of Ring laser frequency to within 2MHz. To generate the Doppler-free saturation spectrum, we counter propagate two laser beams with nearly equal intensity (~140μW two beam total) overlapping in the heated sodium cell. The fluorescence light is collected by a PMT at the side of the cell. The fluorescence signal voltage output from PMT is read by Labview computer, and then a feedback voltage is sent out from computer to the external scan port of the ring laser control box to actively lock laser at Lamp-dip of the D_{2a} peak. Shown in figure 2.4 is the typical Doppler-free saturation spectrum scanned over a wide range covering D_{2a}, crossover, and D_{2b}. Figure 2.5 shows Lamb dips at D_{2a} peak.

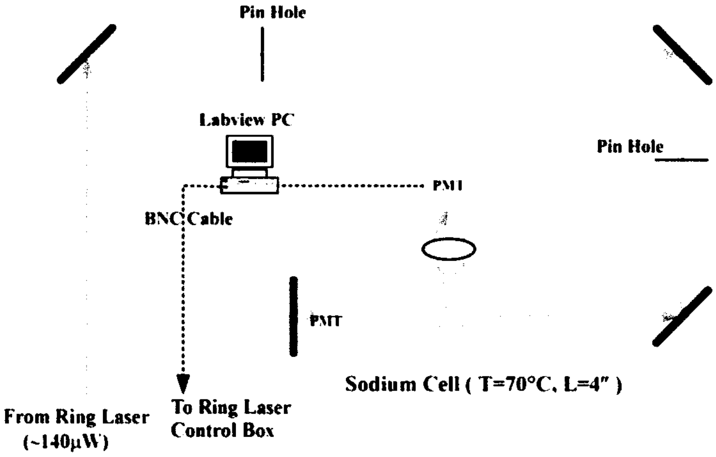

Figure 2.3 Schematic diagram of Doppler-free system. The orange solid lines with arrows denote the sodium laser beams and their propagation direction. The beam enters into a sodium cell (4cm diameter), and then is reflect back into the cell by a mirror. A PMT is placed in the side of cell to collect the laser-induced fluorescence. The black dash lines are the BNC cables. The Labview computer reads the voltage from PMT and then sends a feedback voltage back to the ring laser control box to actively lock laser frequency at deepest Lamp-dip of D_{2a} peak.

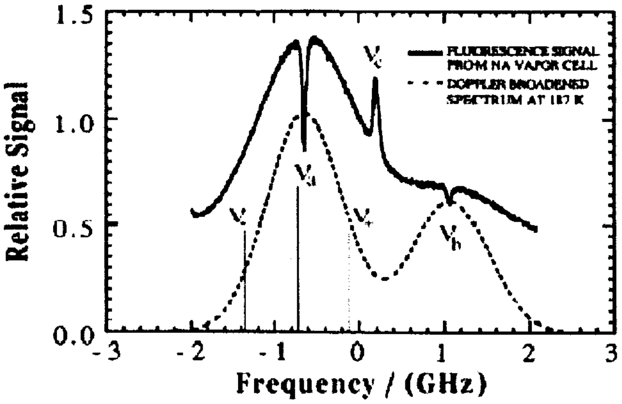

Figure 2.4 the typical Doppler-free saturation spectrum scanned over a wide range covering D_{2a}, crossover, and D_{2b} [Arnold and She, 2003]

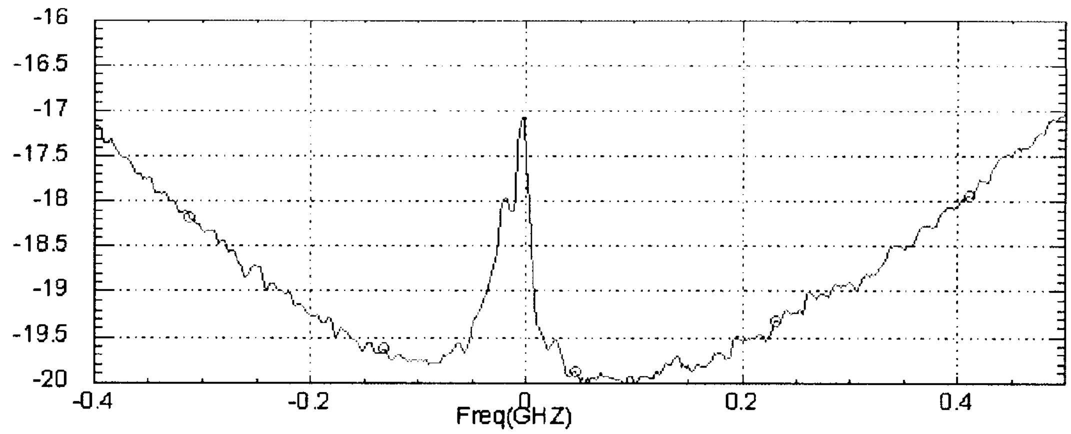

Figure 2.5 Zoom-in scan for lamb dips at D2a peak. [Yuan, 2004]

2.1.3 Acoustic-Optic Modulator (AOM) for precise frequency shifting

Since the frequency of ring dye laser is always actively locked at Lamp-dip of D_{2a} peak frequency, ν_0, in the Doppler-free saturation spectrum, the required two side bands, up must be generated by up and down shift of 630 MHz from ν_0. The AOM consists of two crystals. It is external triggered by a TTL pulses to launch traveling acoustic waves to one or the other crystal to convert the CW beam at D_{2a} peak frequency to + or - sideband for a 10 ms duration, long enough to ensure that the pump pulse of the PDA will occurred in this window. The TTL triggers are arranged, at a rate of 50 Hz to be in synchronization with the rate of the pulsed Yag laser, to send acoustic wave cyclically to neither, to the up-shifter crystal, and down-shifter crystal. The resulting light at the 3 frequencies is sent into the pulse dye amplifier (PDA), and the amplified pulses (~ 7ns in width) in the cyclical order are then sent into the atmosphere. To initiate the sequence, the chopper wheel inside the AOM (described below) rotating at 50/3 Hz is used to chop the CW beam to square wave ~ 10 ms wide. The chopper wheel on the one hand initiates 50 Hz laser shot signal and 50/3 Hz reset reference signal (to be discussed later) for timing control, and on the other hand to spatially block the residual un-shifted light from entering the PDA when AO is operated in the + and – shift cycles [White, 1999].

When the piezo-electric transducer on one side of AO crystal receives a sinusoidal electrical voltage, it will apply a strain to the crystal, create a traveling acoustic wave (315MHz for our lidar system) which traverses the crystal, and vary the index of refraction inside the crystal. If a laser beam is incident into the crystal, it will interact with the acoustic wave and then be partly diffracted. The resulting diffracted beam will have different frequency from incident beam in accordance with conservation of energy and momentum. From conservation of energy the frequency of diffracted beam will be shifted by the amount of the acoustic wave frequency whereas the conservation of momentum defines the diffraction angle 2θ, and depending on the propagation direction of the acoustic wave, determines whether the frequency of the diffracted wave will be up-shifted or down-shifted. According to the first-order of Bragg diffraction condition, the incident angle θ is given by $\sin\theta = \lambda_i/2\lambda_a$, where λ_i is wavelength of incident beam and λ_a is wavelength of acoustic wave [Tipler, 1969].

In order for the beam to exit the AOM and enter into the Pulse Dye Amplifier with the same path independent of the final frequency, our current AOM setup shown in figure 2.6 uses a double-pass configuration with two AO crystals separated by imaging lens. The double-pass configuration is illustrated in figure 2.7. When both transducers on the side of crystals are turned off during 0-20ms, the beam will be reflected back to beam splitter

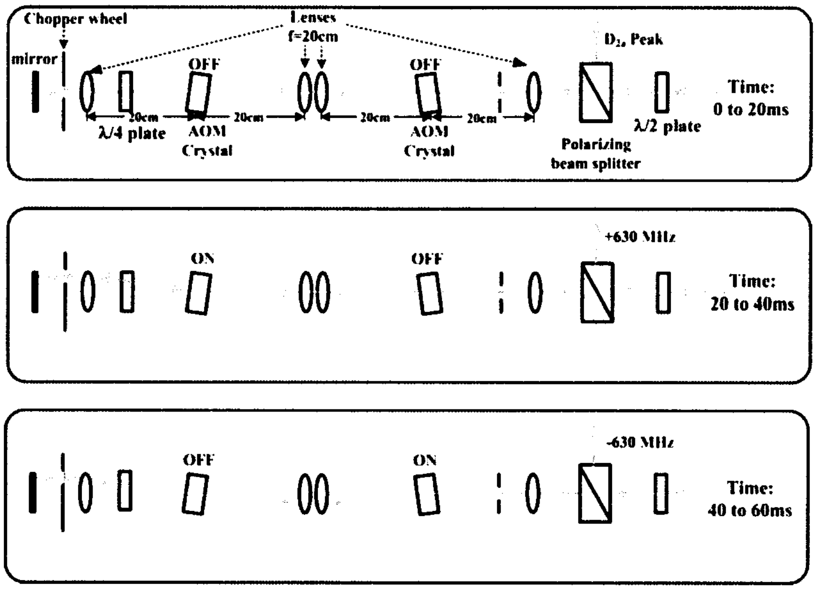

Figure 2.6 Schematic diagram of Acoustic-Optic Modulator unit used in our sodium lidar system. During the three different time periods, the beam paths inside the AOM are different and demonstrated separately in three boxes. [White, 1999]

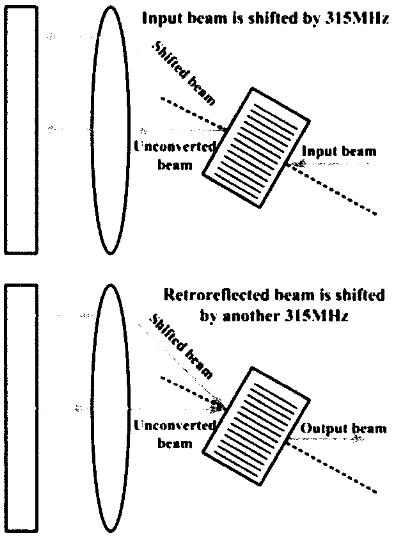

Figure 2.7 Double pass configuration leading to a net of twice frequency shift

without frequency change. The reflected beam exits beam splitter in a perpendicular direction to the incident beam due to 90° polarization change when passing through quarter wave plate twice. When only the left side crystal is active during 20-40ms, the incident beam will be diffracted twice, leading to net frequency upshift of 630MHz.

When only the right side crystal is active during 40-60ms, the reflected beam will be downshifted by 630MHz.

2.1.4 Pulse Dye Amplifier

The pulse Dye Amplifier (PDA) pumped by a pulse Nd:YAG laser is the last stage of the transmitter. The c.w. beam with a power of 100-120mW (unshifted, for shifted beam ~ 60% of this value) exits from AOM and enters into PDA for power amplification to produce narrowband (~120MHz) output beam of ~12ns (FWHM) pulse with an average power of ~1W and beam divergence of ~1mrad. As mentioned earlier, the c.w. beam is chopped into 10 ms square waves to avoid gain saturation in the dye between pulses. There are three dye cells, where the chopped beam and pulse beam interact with each other, for three stages of amplification inside PDA. The gain medium circulated by a pump through the dye cells is a mixture of Rhodamine 640 (9.16mg, 1.9mg respectively for first stage, second and third stage) and Kiton Red 620 (44.3mg, 14.3mg respectively for first stage, second and third stage) dissolved in 1000ml methanol (first stage has different concentration of dye from second and third stages). The Amplified Spontaneous Emission (ASE), which is the natural result of dye pumped by a pulsed Nd:YAG and is broadband without direction preference, could contaminate the purity of output beam with Gaussian shape centered at the seed frequency. However, with careful alignment of PDA, the ASE can be reduced typically to less than 2% of total output power. Figure 2.8 shows the measured line shape of output beam from PDA.

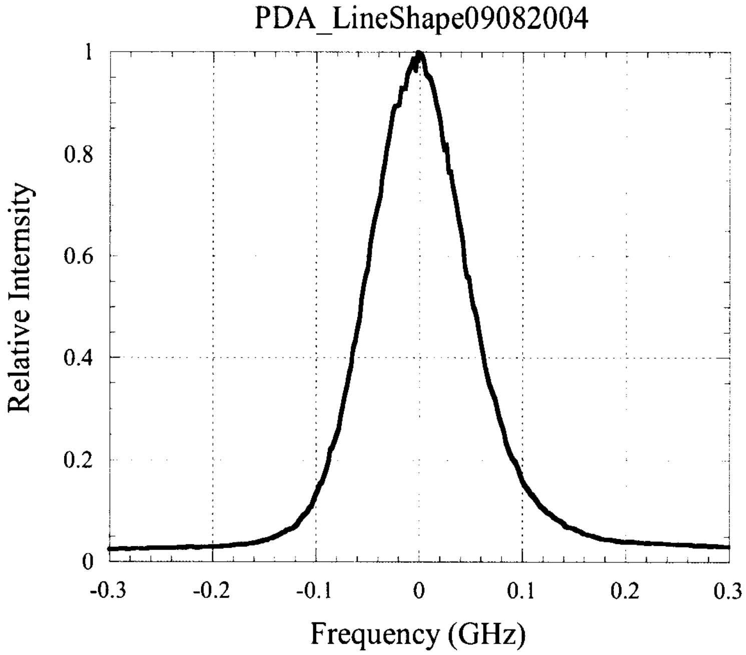

Figure 2.8 PDA pulse lines shape as measured by a 750MHz (FSR), finesse 70 confocal interferometer. The shape is nearly Gaussian. 0GH frequency is the center of mass of the pulse.

2.1.5 Chirp frequency monitor for PDA output beam

Frequency chirp and shift resulting from a nonlinear amplification process produces a (centroid) frequency shift of PDA output beam from the frequency of seed beam. This could introduce an bias in the radial wind measurements. Since the linear Doppler shift relates LOS wind speed, V_c in m/s to Doppler shift $\Delta\nu_c$ in MHz as $V_c = -0.589158\times\Delta\nu_c$, if the output laser frequency shifts 1MHz from the seed frequency $\Delta\nu_c$ = 1MHz, it could induce a wind bias of ~0.6m/s which should be removed from the measured radial wind velocity. In order to determine $\Delta\nu_c$ experimentally, a “chirp” box containing an iodine cell heated up to 80°C is used in the current lidar system by measuring the iodine transmission at each of three frequencies. The pulse iodine transmission, the correlation of CW iodine transmission with pulse line shape (shown in figure 2.8), is used to extract the real-time frequency offset $\Delta\nu_c$. The detailed discussion of chirp can be found in the previous dissertations [White 1999; Sherman, 2002]. Shown in figure 2.9 is the CW iodine transmission with its corresponding pulse transmission.

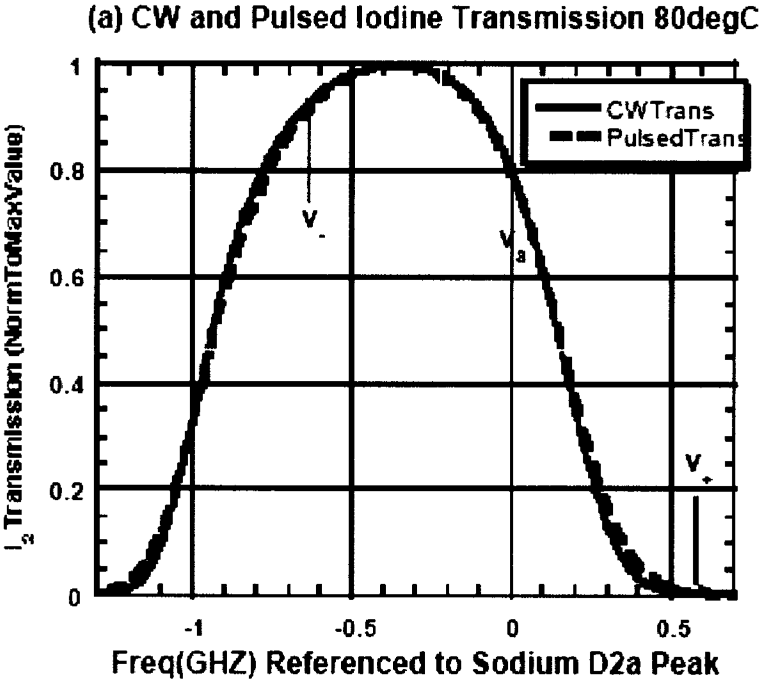

Figure 2.9 Iodine transmissions at 80°C for a CW beam and for a pulsed beam [Sherman, 2002]

2.2 CSU sodium lidar receiver subsystem

As shown in the schematic diagram of the CSU sodium lidar system in figure 3.1, two-beam setup is used for temperature and wind measurements. One beam is pointing 30° from zenith toward the east for temperature and zonal wind measurements. Another beam is pointing 30° from zenith toward north for temperature and meridional wind measurements. Backscattered photons are received by two 14 inch Schmidt-Cassegrain telescopes with each parallel to one of two beams. Then the collected photons are coupled into fibers and sent into the detection system for processing. Before photons are converted into electric pulses in the PMT, they need pass through an interference filter with 3nm bandwidth centered at 589nm to cut the background levels (In the daytime the Faraday filter is placed in front of interference filter to effectively reject scattered skylight). The PMT output electric pulses are amplified by a preamplifier (×100) and then sent into a discriminator with a voltage threshold set to reject most noise (currently set to ~600 mV). The discriminator also converts electric pulses to 10ns TTL pulses which are finally recorded by a photon counter board (FDC-700M) in the "Optech" computer yielding range-resolved raw data profile. Figure 2.10 shows the schematic diagram of the optics of the lidar receiver subsystem.

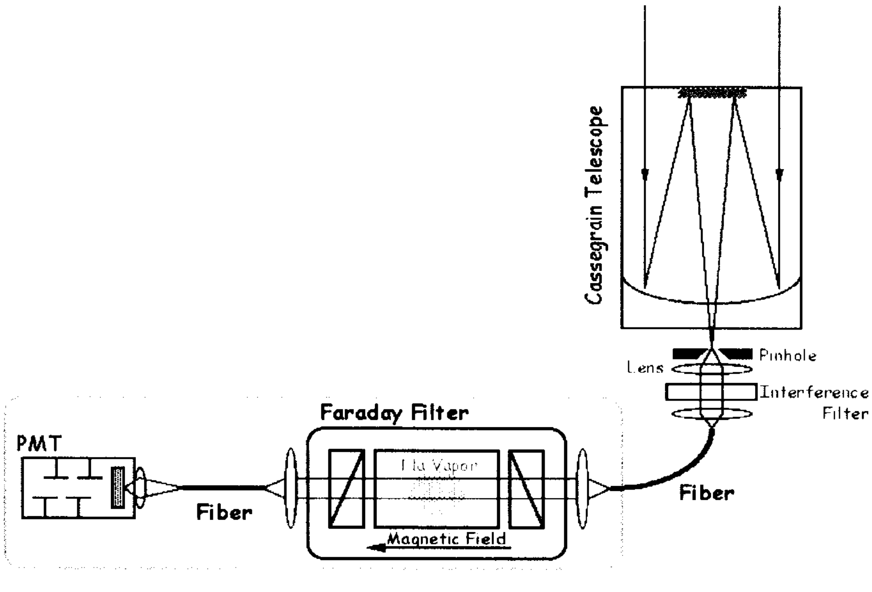

Figure 2.10 Schematic diagram of receiving system.

2.2.1 Fiber coupled telescope

The receiving telescopes used in our lidar system are 14-inch diameter Schmidt-Cassegrain optical design (Celestron 14 commercially available) with a focal length of

3.91m (f/11). The backscattered photons received by telescope will be coupled into a fiber which is 1mm diameter with a numeric aperture of 0.116 by a lens with 5cm focal length. The positions of the lens and fiber relative to the focal point of telescope are decided by considering the conservation of etendue for all the optics. In our case, the output laser beam with nearly circular cross section and a full divergence of 1mrad is sent into atmosphere. In the mesopause region (~100 km), the diameter of laser beam is ~100m, and the image size of scatters at the focal plane of the telescope is ~4mm. The system etendue could be calculated by the equation $Etendue = NA \bullet Diameter$, which is 0.175 mm for our system. In order to conserve this quantity, the fiber is facing approximately 4cm from the focusing lens and fitted into a 3-dimensional translating mount for easy adjustment. Due to the bi-axis setup between telescope and laser beam, the total overlap altitude is about 20km. The Rayleigh signals at 20-40km will be used to normalize the powers at three frequencies, and signals at 30 km are used as reference for sodium density calculations. We will discuss details in the next chapter.

2.2.2 Faraday filter for daytime measurement

In the nighttime observation, the interference filter with 3-nm bandwidth is adequate enough to reduce the background levels due to city lights, moon, and stars. However, in the daytime observation, very strong skylight background needs to be effectively rejected in order to extract weak embedded sodium signals. An innovative ultra-narrowband Na vapor filter utilizing the anomalous dispersion (Faraday Effect) was developed for CSU lidar group in 1993 by H. Chen [Chen et al., 1993], then modified by S. Chen [Chen, 1999], and finally improved by T. Yuan [Yuan, 2004] with better stability. The 85% transmission at the line center of the Na D_2 transition (λ=589.158nm) with a FWHM of 1.9GHz (0.002nm) and a background transmission of 2×10^{-5} has been achieved for Na Faraday filters. The current CSU Faraday filter includes a sodium vapor cell heated up to 150°C with an axial magnetic field of 1850 Gauss and placed between two crossed polarizers. Schematic diagram of Faraday filter is shown in figure 2.11. The measured transmission curve is shown in figure 2.12.

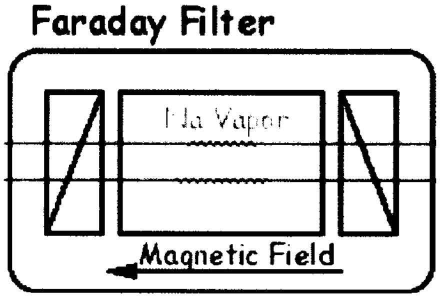

Figure 2.11 Schematic diagram of Faraday Filter.

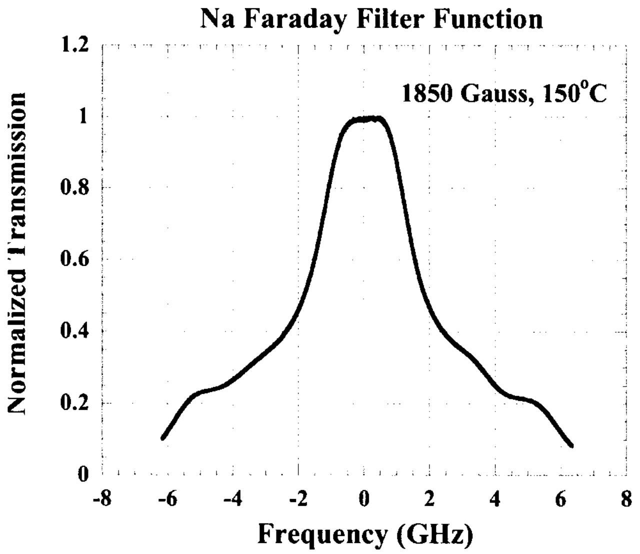

Figure 2.12 Measured transmission function of Faraday Filter

For simplicity, let's assume sodium to be a two-level system (L = 0, and L = 1 for ground and excited states) with transition frequency ν_0 [Arnord and She, 2003]. In an axial magnetic field, it is natural to choose the z-axis of atomic wave functions parallel to the magnetic field. The Zeeman effect will split the allowed transitions, with magnetic quantum number selection rule, $\Delta m = 0, \pm 1$ [Corney, 1977] into a triplet with transition frequencies, ν_0, ν_0^+ and ν_0^-, each with a specific polarization. The linear polarized sodium light coming out from first polarizer with frequency at ν_0 could be decomposed to two components, right circular polarized light and left circular polarized light. The circular birefringence resulting from the Zeeman-effect-induced difference in dispersion between two circular polarizers produces a phase difference between two circularly polarized components as they reach the second polarizer. Understandably, this phase difference depends on the sodium density (or cell temperature), magnetic field, length of cell, and wavelength of the light. If the two components end up out of phase (phase difference = 180°), the resultant linearly polarized light will be rotated 90° from initial linearly polarized light, and will be transmitted the second polarizer without loss, if the magnetic field is strong enough so that the Zeeman absorption sidebands, ν_0^+ and ν_0^- shift from ν_0 more than the Doppler width of the transition. Skylight with frequency outside the bandwidth of the Faraday filter (2 GHz or 10 GHz) will almost totally be rejected mostly by the two crossed polarizers.

2.3 CSU sodium lidar electronics and timing subsystem

As a very important part in our sodium lidar system, the electronics and timing subsystem controls all the system and collects the data. Since our lidar operates at three frequencies of D_{2a} peak, +630MHz, and -630MHz (laser frequency is shifted on a shot-by-shot basis) with 2-beam setup, and collects data with only one 2-channel Optech counter board, the operating frequency cycling with proper order must be maintained, once the counter is triggered. In the other word, to make certain that the photons collected at each laser frequency are being correctly sorted and integrated, we require more complicated electronics to control and monitor the whole system than other types of lidar systems, to our knowledge. The schematic diagram of electronic and timing subsystem is shown in figure 2.13, which includes one Programmable Logic Device (PLD) box (the heart of electronics), two Boxcars for chirp measurements, one PMT impedence matching device and one National Instrument BNC-2090 board connected with a Data Acquisition (DAQ) card in the Labview computer. There are also some other components not included in this drawing, such as chopper wheel controller, AOM controller, radar sky safety system, etc.

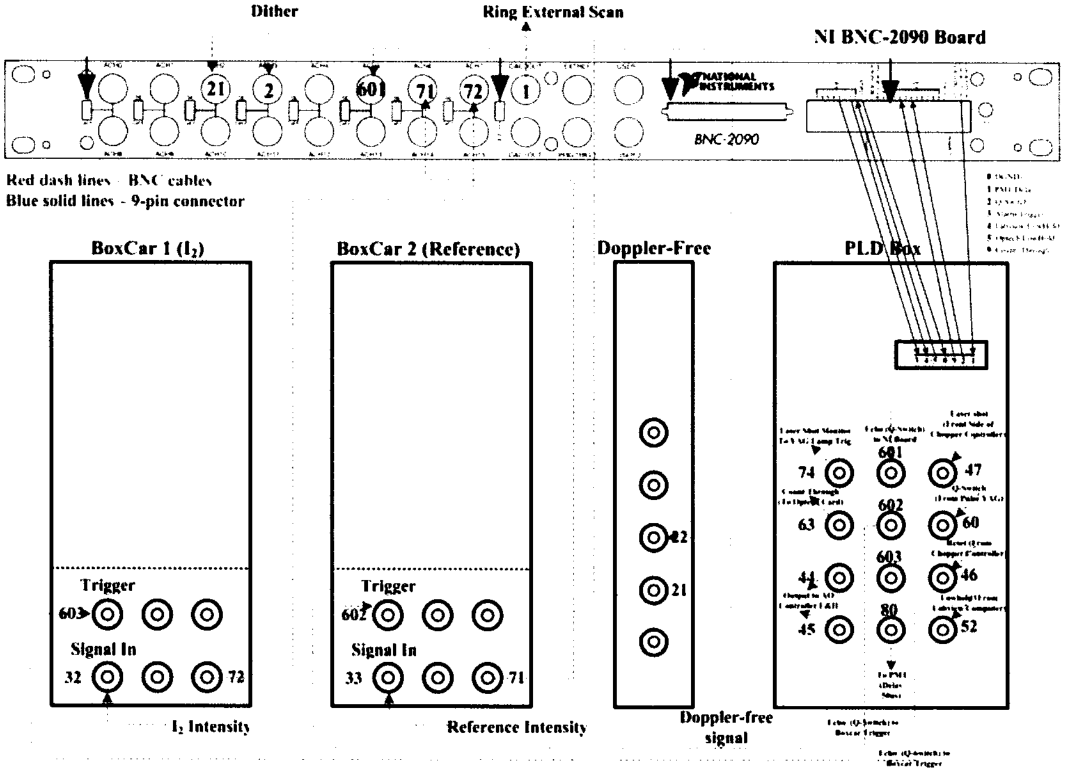

Figure 2.13 Schematic diagram of electronics and timing subsystem. The red dash lines denote the BNC cables and blue solid lines denote 9-pin connector connecting NI BNC-2090 board with PLD box. Connectors pointed by red and blue arrows are input. Connectors without arrow pointing are output. NI BNC-2090 board is connected with a DAQ-6024E card in the Labview computer.

2.3.1 Timing diagram and required signal

We present the timing diagram and nomenclature for each required control signal in figure 2.14 with a brief explanation in table 2.1. The schematic diagram of synchronization is shown in figure 2.15. After some familiarity is gainded, the need and implementation of these signals will discussed along with electronics components.

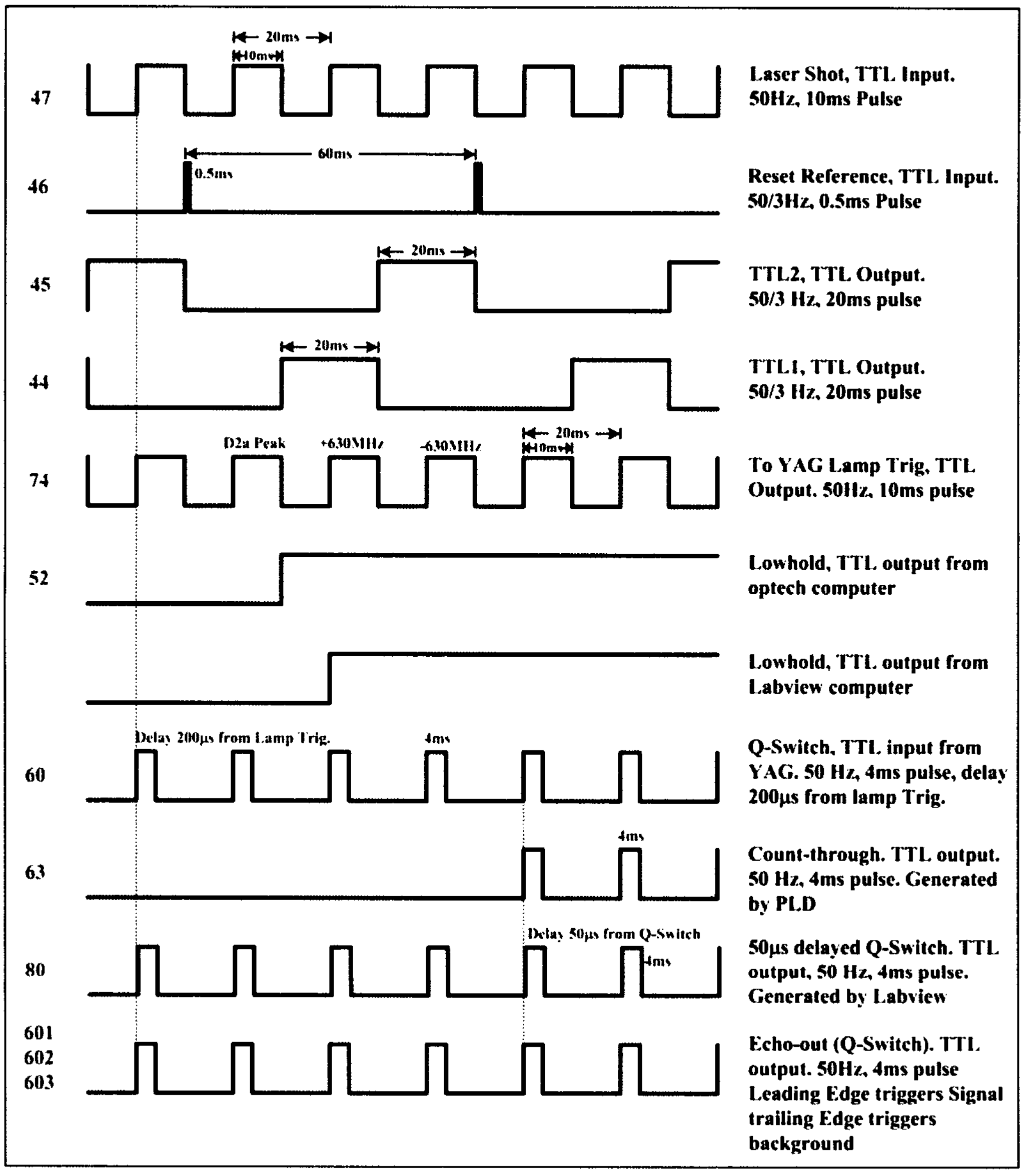

Figure 2.14 Timing diagram for most of the signals with corresponding pulse frequency and width. The blue number to the left of each signal is used to number the BNC connected to the signal in question.

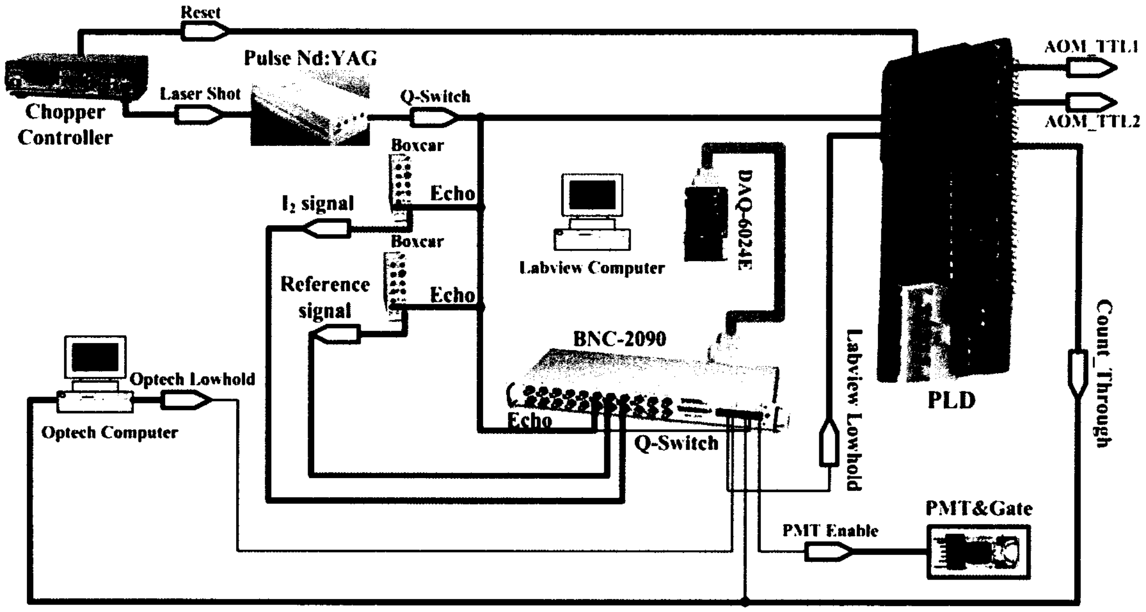

Figure 2.15 schematic diagram of synchronization. Black solid lines denote the BNC cables. Blue solid thin lines denote the 9 pins from PLD box to BNC-2090 board.

Table 2.1 summarization of signals used in our sodium lidar system

Signals	Generated by	From	To	Purpose
Laser Shot	Chopper Wheel	Chopper controller	Pulse YAG lamp trigger	Trigger Pulse YAG
Reset	Chopper Wheel	Chopper controller	PLD chip	To generate count_through and AOM_TTL1 and AOM_TTL2
AOM_TTL1 & AOM_TTL2	PLD	PLD chip	AOM controller	Control the phases of two AOM crystals
Optech Lowhold	Optech computer	Optech computer	BNC-2090	Tell labview computer whether Optech computer is ready to take data
Labview Lowhold	Labview computer	Labview computer	PLD chip	To Generate count_through
Q-Switch	Pulse YAG	Pulse YAG	PLD chip	To generate count_through and AOM_TTL1 and AOM_TTL2
Count_through	PLD	PLD chip	Optech trigger	Trigger Optech counter board
PMT enable	Labview	BNC-2090	PMT	Open PMT gate
Echo	Q-Switch	Q-Switch	Boxcars, and BNC-2090	Trigger Boxcars, and distinguish signal and background of chirp data

2.3.2 Programmable Logic Device (PLD) box

The Programmable Logic Device (PLD) box is the central interface for most input and output signals. It also generates several important TTL signals by a PLD chip inside this box, such as count_through signal for triggering Optech counter board, AOM1_TTL1 and AOM_TTL2 for controlling the activation timing of two AOM crystals. Shown in figure 2.16 is the schematic diagram of the BNC connectors on the front panel of PLD box. The 9-pin connector (only 7 pins are used) going from NI BNC-2090 to PLD box isn't shown in this diagram.

Hubert's Box (PLD Box)

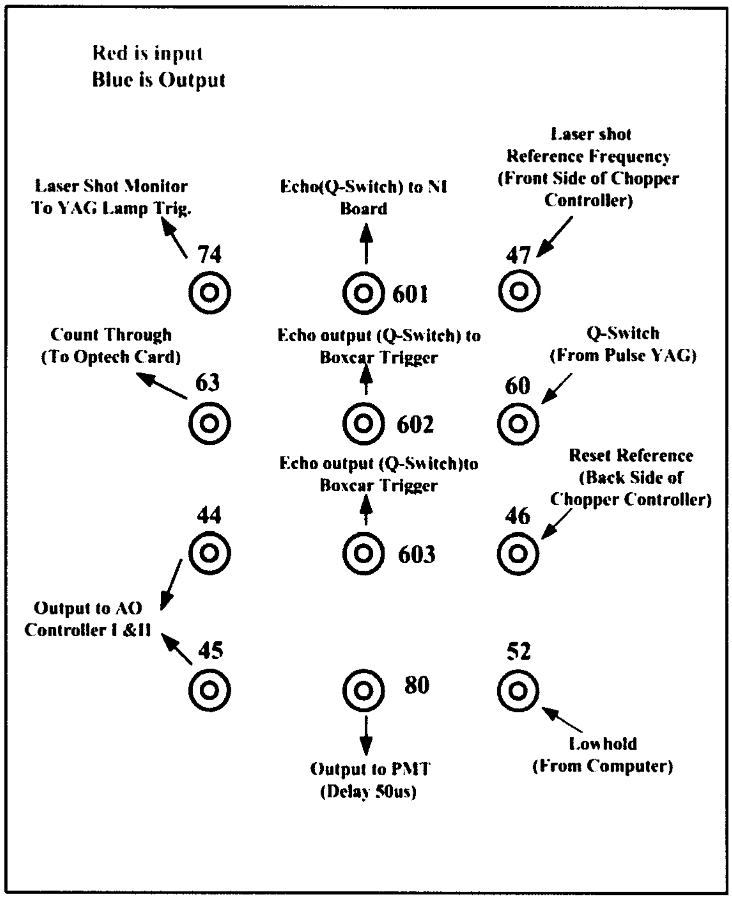

Figure 2.16 Schematic diagram of the BNC connectors on the front panel of PLD box. Red connectors represent input, and blue connectors represent output. Connectors and associated BNC cables are labeled by number for identification purpose

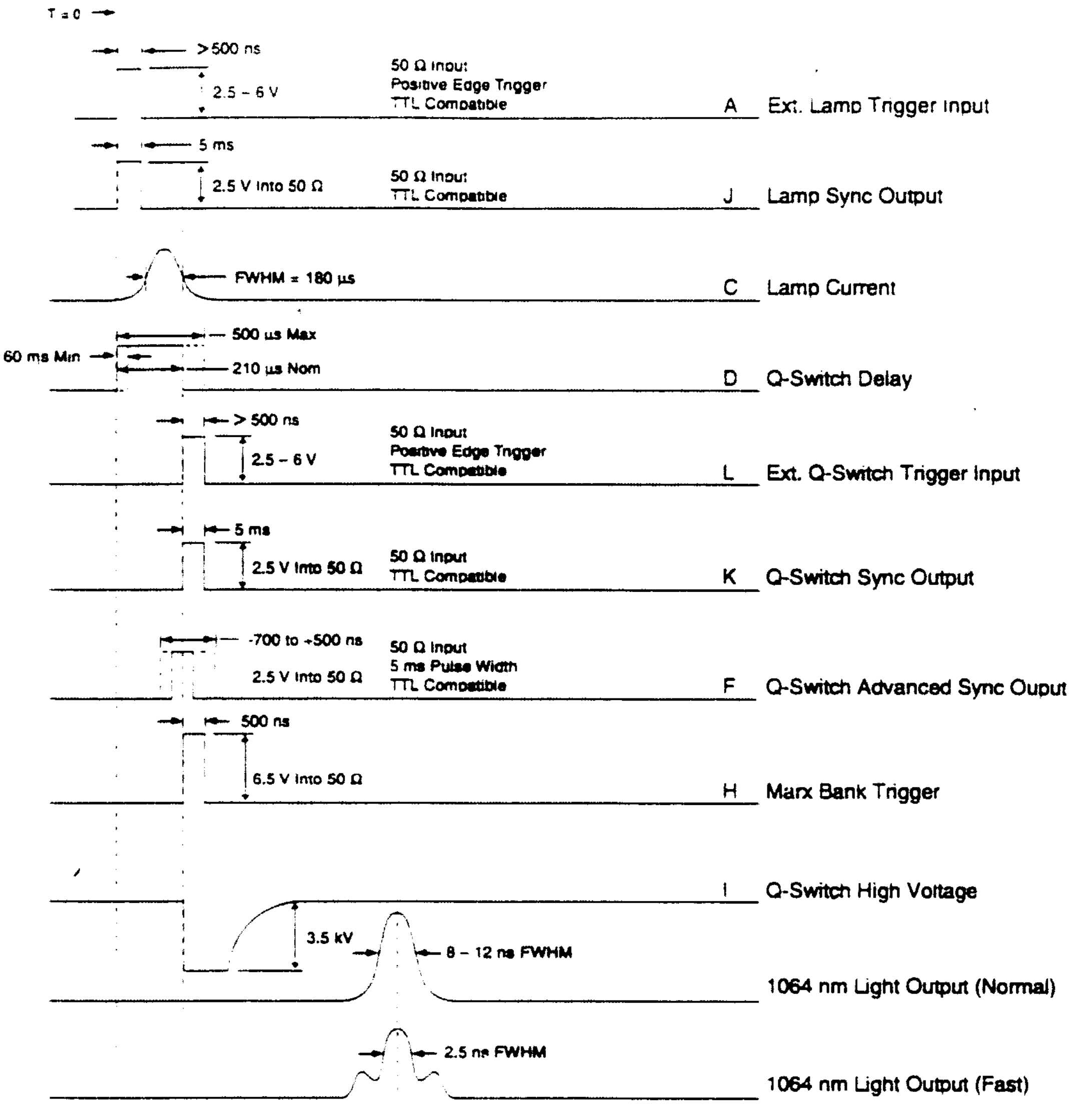

Figure 2.17 Schematic timing diagram of Spectra-Physics pulse Nd:YAG laser [Spectra-Physics Nd:YAG laser manual]

In figure 2.16, four BNC connectors at the right column are input, and the rest of connectors are all output. Four input connectors are laser shot, Q-Switch, Reset, and Optech Lowhold. The laser shot, a TTL signal with 50 Hz and 10 ms width, is generated from chopper wheel controller; and its rising edge is used to trigger the lamp of the pulse YAG. The Q-Switch signal from pulse YAG is used as a reference from which the time of flight is measured, and the return counts are binned. Since the frequency is shifted on a shot-by-shot basis, the data must be parsed to maintain the correct ordering. The optech program assumes that the 1st pulse it receives after labview low_hold goes high is an unshifted pulse (D_{2a} peak), then upshifted (+630MHz) and downshifted (-630MHz) occur and the process repeats. There is a small delay (200μs) between the lamp trigger which is laser shot signal and Q-Switch. Shown in the figure 2.17 is the timing diagram of pulse Nd:YAG laser. Reset signal, which is the TTL at 50/3 Hz with a width of 0.5 ms and also generated by chopper wheel controller, is used to start a frequency cycle. The chopper wheel system in the AOM thus becomes the synchronizing clock source for the entire lidar system. Optech Lowhold signal is generated by Optech computer. The Optech Lowhold is low when the Optech computer is not yet ready to acquire data and high when it is ready. This Lowhold signal will be sent into BNC-2090 board through 9-pin connector and read by Labview program.

It turns out that we need another Lowhold signal in current system, which is generated by Labview program. It is also sent into PLD box through 9-pin connector. Once the Optech computer completes its preset number of pulses (usually set 6000), the Optech Lowhold goes low. When Labview sees this change, it sets the Labview Lowhold to low, and begins its inter-file scan for D_{2a} peak spectrum and then locked to the D_{2a} peak. At this point, the Labview waits for the Optech to be ready and Lowhold to go high. Once the Labview sees that the Optech Lowhold is high (and the laser is locked to the D_{2a} peak), the Labview Lowhold goes high, and initiate the count_through signal, and trigger the Optech counter board in the Optech computer for data acquisition.

There are three identical TTL signals (in fact just duplicated Q-Switch) output from PLD box. Two are used to trigger the boxcars for taking chirp reference diode signals and I_2 diode signals. Another TTL will be sent into BNC-2090 board and read by Labview program to mark the 20μs time interval for signal and background. The Labview program uses background subtracted reference and I_2 signal for chirp calculation and display. The PMT enable signal (50μs delayed from Q-Switch) is generated through digital counter of BNC-2090 by Labview program and sent into PLD box through 9-pin connector. Due to very strong backscattering of aerosol and Rayleigh in the lower atmosphere which could saturate the PMT, the PMT's dynode is set at lower value at first 50μs (the first 7.5km of the atmosphere from ground) after pulse YAG laser fires. This signal will be sent out from PLD box to PMT circuit to open PMT gate and start taking data.

Count_through signal, AOM_TTL1 signal, and AOM_TTL2 signal are generated by PLD chip inside the box from three other input signals (Reset, Q-Switch, and Labview Lowhold). The schematic diagram of PLD chirp with inputs and outputs is shown in figure 2.18. Count_through is generated through logic unit 1 of PLD by using all three inputs. In fact this signal is identical to Q-Switch, except that it starts immediately after the first reset and when Labview Lowhold is high. Both AOM_TTL1 and AOM_TTL2 are generated through logic unit 2 of PLD by Reset and Q-Switch. They are used to control the phases of AOM crystals. During the first 20 ms after Reset (a total of 60 ms between two Resets), AOM_TTL1 and AOM_TTL2 both are low in order to let unshifted beam pass through. During the second 20 ms, AOM_TTL1 is high, but AOM_TTL2 is low. The frequency of the laser beam is up-shifted by +630MHz. During the last 20 ms, AOM_TTL1 becomes low, whereas AOM_TTL2 becomes high. The frequency of the beam is down-shifted by -630MHz.

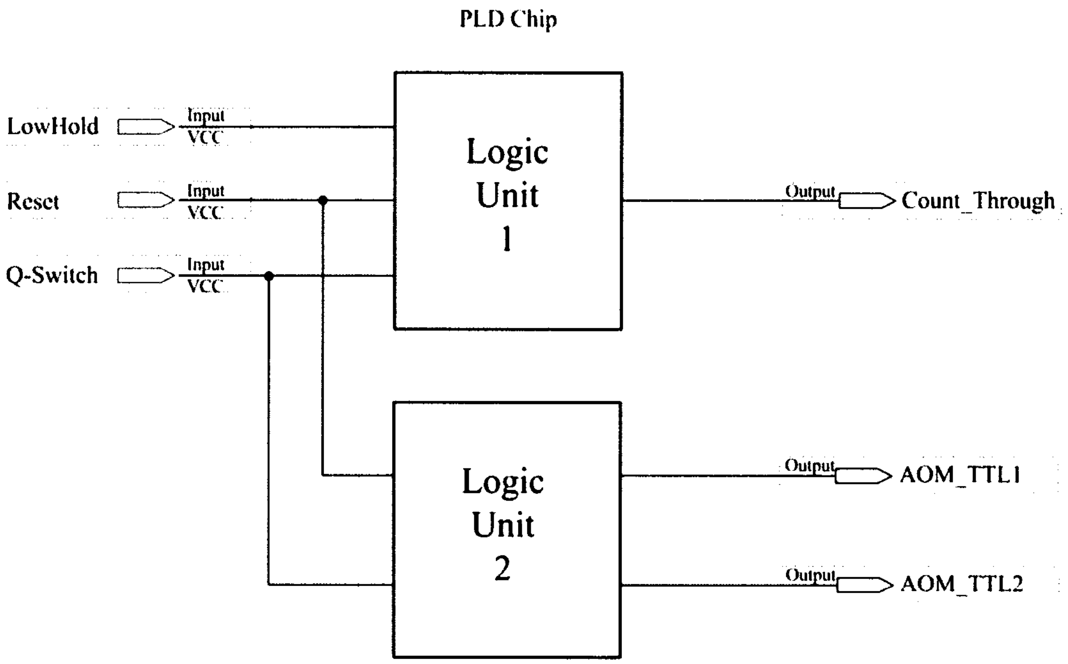

Figure 2.18 Schematic diagram of Programmable Logic Device chirp with three inputs and three outputs. Red connectors are inputs in the left side. Blue connectors are outputs in the right side. Green box denotes the whole chip including two logic units for different logic purposes.

The PLD device used in the current system is the Intro-FPGA setup from HVW Technologies. It is programmed through a parallel port connection to the labview computer by Altera's free MAX+PLUS II Baseline software version 10.2 with a graphical schematic-drawing interface. Since this device is very sensitive to ground connections and easily distroyed by statics, it is not as robust as what we would like it to be. Once the electronics and timing system doesn't work, the one who does trouble-shooting should first look this device by checking all the inputs and outputs. If all the inputs are working well but one or more outputs are not, one needs to replace the chip inside the PLD box and reprogram it with MAX+PLUS II.

2.3.3 BNC-2090 board controlled by Labview program

The National Instrument BNC-2090 board simplifies the connection of analog signals and digital signals to the DAQ card controlled by Labview program. As shown in figure 2.13, there are five analog inputs and one analog output as well as several digital inputs and outputs. The five analog inputs are Doppler-free signal for dynamic locking Ring laser frequency at D_{2a} peak, dither signal for fast tuning the Ring laser frequency and generating zero-crossing locking point, chirp I_2 signal integrated by boxcar, chirp reference signal integrated by boxcar, and echo signal (Q-Switch) as reference. A feedback voltage generated by labview program through Doppler-free spectrum and dither signal is sent out to external scan input of the Ring laser control box for actively locking laser frequency. This feedback voltage is updated in every 0.4s (total 300 times in 6000 shots). Chirp data are averaged over 6000 shots and calculated by Labview program to give the real time chirp velocity. The digital signals of Optech Lowhold, Labview Lowhold are input/output through DIO channels. Count_through is input through PFI2 channel to configure the clock for locking subroutine. The PMT enable signal for opening PMT circuit gate is generated by a Pulse-Train function in the Labview program. Its rising edge is delayed by 50μs from the rising edge of the Q-Switch pulse. This signal is output from Counter Out #1 (CTR1OUT) to PLD box through 9-pin connector.

When Optech computer is taking data, the Labview computer keeps actively locking laser frequency by outputting a feedback voltage to the external scan input of the Ring control box. Once Optech computer finishes 6000 shots and saves data, Optech Lowhold goes low. Then the Labview computer stops locking subroutine and starts scanning routine which does inter- scan for D_{2a} peak. When Labview finishes its inter-scan and also Optech computer is ready to take data (Optech Lowhold goes high), the locking subroutine is restarted for active locking and Optech computer starts data taking. This procedure repeats every 6000 shots (2 minutes).

2.3.4 Other components

Two SR250 boxcars are gated integrators, used to process the reference and I_2 signals from the "chirp" box. By connecting the gate output and signal output of the boxcar to oscilloscope, we can monitor relative position between two signals, and by adjusting to make sure the entire signal pulse is within the set gate width. The integrated signals are output from last sample, sent into BNC-2090 board, and then read by Labview program.

Since the lidar transmitter sends out 2 laser beams into the atmosphere, each with averaged power of around 0.5W which is not considered eye-safe in the troposphere, it is required to monitor the air craft traversing the beam path according to the FAA guidelines on air safety. In order to automatically monitor air craft flying into the beam path, we deployed two marine radar systems by pointing the scanning vertical, one for monitoring north beam path, and another for monitoring both east and zenith by rotating the radar transmitter. The guard alarm functions on the two radars could be set up to guard a particular region of altitude. During the typical lidar operation, the guard zone is set from near ground to an altitude of 16km, above which the eye safe is not an issue. If either of radars detects the aircraft entering into guard zone, it will send out a signal through external customized interlock circuit to automatically and instantly turn off the pulse Nd:YAG laser.

Reference:

Arnold, K. S., C. Y. She, Metal fluorescence lidar (light detection and ranging) and the middle atmosphere, *Contemp. Phys.*, 44, 35-49, 2003

Chen, H, C. Y. She and Eric Korevaar, Na Vapor Dispersive Faraday Filter, *Opt. Lett.,* 18, 1019-1021, 1993.

Chen, S., 24 Hour Lidar Campaigns and Tidal Analysis, *PhD Dissertation*, Colorado State university, 1999.

Corney, A., *Atomic and Laser Spectroscopy*, Oxford, 39, 1977.

She, C. Y., Remote Measurements of Atmospheric Parameters: New Applications of Physics with Lasers, *Contemp. Phys.*, 31, 247-260, 1990.

She, C. Y., J. R. Yu, H. Latifi, R. E. Bills, High-spectral-resolution Fluorescence Light Detection and Ranging for Mesospheric Sodium Temperature Measurements, *Appl. Opt.*, 31, 2095-2106, 1992.

She, C. Y., and J. R. Yu, Doppler-free saturation fluorescence spectroscopy of Na atoms for atmospheric application, *Appl. Opt.*, 34(6), 1063-1075, 1995.

Sherman, J. P., Mesopause Region Thermal and Dynamical Studies Based on Simultaneous Temperature, Zonal and Meridional Wind Measurements with an Upgraded Sodium Fluorescence Lidar, *PhD Dissertation*, Colorado State University, 2002.

Tipler, Paul A., 1969, Foundations of Modern Physics. In *The Quantization of Electricity, Light, and Energy* (New York: Worth Publishers, Inc.). pp. 103-144.

White, M. A., A Frequency-agile Na Lidar for the Measurement of Temperature and Velocity in the Mesopause Region, *PhD Dissertation*, Colorado State University, 1999.

Yuan, T., Seasonal variations of Diurnal and semidiurnal tidal-period perturbations in mesopause region temperature and zonal and meridional winds above Ft. Collins, CO (40°N, 105°W) based on Na-Lidar observation over full diurnal cycles, *PhD Dissertation*, Colorado State University, 2004.

Chapter 3: Sodium Lidar Theory and Data Analysis

Firstly, this chapter will briefly and qualitatively discuss the atomic sodium hyperfine spectrum, its fluorescence induced by laser, and their temperature and wind dependence. Since many details of quantum mechanics have been presented by Corney [Corney, 1977] and in the PhD dissertations [H. Chen, 1997; S. Chen, 1999; M. White, 1999], we will focus more on the concepts to understand the 3-frequency lidar measurements of temperature and wind. Then the sodium lidar equation will be presented in detail. Experimental wind and temperature ratios constructed from raw photon counts are connected to the ratios of sodium cross sections by this lidar equation. Theoretical sodium cross sections are calculated from the sodium hyperfine spectrum. As a result, the 2D calibration curves are formed and used to retrieve the temperature and wind from experimental ratios. Finally, we discuss the processing of raw photon data to obtain temperature, wind, and sodium density.

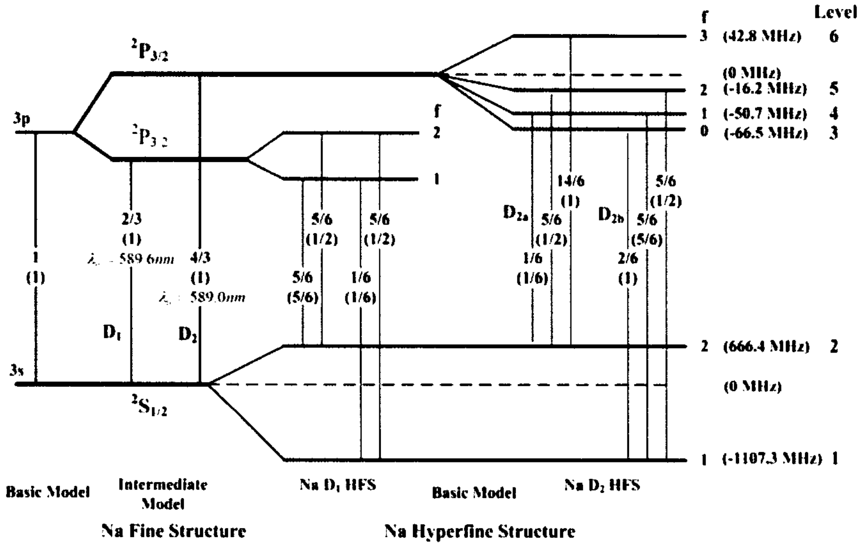

Figure 3.1 Energy-level diagram of atomic sodium in three different models. Basic Model is only a two-level system. In intermediate model, the electron spin is included, and the excited state is split to 2 levels. The final model includes the nuclear spin interactions, which gives a hyperfine splitting of the energy-levels. [She and Yu, 1995]

3.1 Sodium fluorescence hyperfine spectrum

Sodium D_2 transition near 589nm, especially D_{2a} transition at 589.158nm, is of primary interest for the CSU 3-frequency sodium lidar system. Since the lidar receives backscattered sodium fluorescence photons excited by the laser beam sent into atmosphere, we also need to consider the laser induced sodium fluorescence. Figure 3.1 shows an energy-level of atomic sodium in three models [She and Yu, 1995].

3.1.1 Sodium resonant D transition

To better understand the Na D transitions physically, we describe the relevant atomic structure in terms of a hierarchy of three related physical models [She and Yu, 1995]. The basic model is for one electron outside a nucleus plus a core of electrons. This gives a hydrogen-like two-state system labeled in figure 3.1 by the orbital angular momentum L, e.g. 3s and 3p with degeneracy of 1 and 3 respectively. This basic model only considers the orbital angular momentum without electron spin angular momentum. In the intermediate model (Na fine structure), electron spin (s=1/2) is included, and degeneracy of energy state is doubled. Spin-orbit coupling ($j=|\ell \pm s|$) splits the excited state 3p into 2 states, a doublet $^2P_{1/2}$ and a quartet $^2P_{3/2}$ and leaves ground state at $^2S_{1/2}$. Sodium D_1 and D_2 transitions are the emission lines from $^2P_{1/2}$ and $^2P_{3/2}$ to the ground state $^2S_{1/2}$ at 589.6nm and 589.0nm respectively (589.7nm and 589.158nm respectively in the vacuum). In the final model (Na hyperfine structure), the Na nuclear spin angular momentum (s_n=3/2) is included into the total angular momentum. The interactions between the electron and the nucleus (f = | j ± s_n |) further split the energy levels into hyperfine structure. The degeneracy then increases by another a factor of 4. Meanwhile the ground state $^2S_{1/2}$, and excited states $^2P_{1/2}$ and $^2P_{3/2}$ are split into 2, 2, and 4 hyperfine levels respectively, labeled by the total atomic angular momentum, F, in figure 3.1 with degeneracy of 2f+1. According to the selection rule, $\Delta f = 0, \pm 1$, the D_2 transition is separated by hyperfine splitting into D_{2a} and D_{2b}, each associated with the transitions from three of four upper excited states to one of two ground states. The frequencies (relative to the weighted center) and relative strength of six discrete D_2 transition lines (3 D_{2a} lines and 3 D_{2b} lines), which contribute to the D_2 fluorescence spectrum, are well known [Hartig et al., 1973, Weise et al., 1969] and listed in table 3.1.

Table 3.1 Frequencies and relative strength of sodium D_2 transition lines

Transition	$^2S_{1/2}$	$^2P_{3/2}$	D_2 line name	offset ν_n (GHz)	Label	S_n (strength)
D_{2b}	f = 1	f = 0	$D_{2b,0}$	$\nu_0 = 1.0408$	ν_{31}	2/6
		f = 1	$D_{2b,1}$	$\nu_1 = 1.0566$	ν_{41}	5/6
		f = 2	$D_{2b,2}$	$\nu_2 = 1.0911$	ν_{51}	5/6
D_{2a}	f = 2	f = 1	$D_{2a,1}$	$\nu_3 = -0.7150$	ν_{32}	1/6
		f = 2	$D_{2a,2}$	$\nu_4 = -0.6806$	ν_{42}	5/6
		f = 3	$D_{2a,3}$	$\nu_5 = -0.6216$	ν_{52}	14/6

3.1.2 Line Broadening

Although the sodium D_2 transition includes only six discrete resonant lines, the transition spectrum is continuous due to various line broadening mechanisms. There exist several types of broadening mechanisms, including natural broadening, pressure broadening, and Doppler broadening. Natural broadening arises from the uncertainty in energy of the states involved in the transition. Natural broadening is homogeneous and produces

Lorentzian line shapes with Full Width Half Maximum (FWHM) of $1/2\pi\tau$ where τ is the lifetime of excited states. For the sodium atom, τ=16.4 ns [Corney, 1977], and the natural broadening will produce the line width of only ~10MHz. Pressure broadening, arising from the collision between atoms, produces the same Lorentzian line shape as natural broadening, and further increases the overall line width of sodium D_2 transition spectrum. However, in the mesopause region where parameters are observed by CSU sodium lidar, the pressure is very low, only ~0.1mbar. Therefore, the line width due to pressure broadening is negligible [Yu, 1995]. Doppler broadening is the broadening of a spectral line as a result of the random thermal motion of sodium atoms, and is therefore highly dependent on temperature. Compared to natural broadening and pressure broadening, Doppler broadening has far more significant impact on the overall line width of sodium D_2 transition in the mesopause region and produces a Gaussian line shape. For a typical temperature of 200K in the mesopause region, Doppler broadening introduces a ~1GHz line width [White, 1999]. Since Doppler broadening is the dominant source of the sodium transition line width in the mesopause region, we can approximately ignore other line broadening sources from analysis. In section 3.3, we will discuss the sodium spectrum without and with natural line broadening included and also discuss the effect on the 2D calibration curve.

With the random thermal motion of the sodium atoms (the center of mass for the given volume is stationary) and assuming environmental equilibrium for the sodium atoms in the mesopause region, different groups of atoms moving with different speed υ toward the detector will experience different transition frequencies due to Doppler shift from the certain group of atoms at rest. The speed distribution of sodium atoms is determined by Maxwell-Boltzmann distribution at given temperature T, and given by equation 3.1:

$$N(\upsilon)d\upsilon = 4\pi N_{tot}\left(\frac{m}{2\pi k_B T}\right)^{3/2} \upsilon^2 e^{-m\upsilon^2/2kT} d\upsilon \qquad (3.1)$$

where

$N(\upsilon)$: number density of sodium atoms with speeds between υ and $\upsilon+d\upsilon$

N_{tot}: total number density of sodium atoms in a given volume

T: absolute temperature

m: mass of sodium atom

k_B: Boltzmann's constant

3.1.3 Doppler Shifting

In laser induced fluorescence, a moving atom first excited by absorbing a photon from the transmitting laser beam. The excited atom then emits a photon that may be detected by the lidar receiver. Since, as to be discussed shortly, the combined effects leave the frequency of the detected photon independent of the motion of the atoms, we discuss the Doppler shift associated with the absorption process. In order for an atom traveling with a velocity υ in the direction of the laser beam to resonantly absorb a photon, the frequency of the laser beam must be higher by Doppler shift and satisfy equation 3.2:

$$\nu = \left(1 + \frac{\upsilon}{c}\right)\nu_0 \qquad (3.2)$$

where ν_0 is the absorption frequency of a stationary atom. The velocity υ is the line-of-sight (LOS) velocity with positive sign when moving along the direction of the transmitting laser beam and negative sign when moving against it.

3.1.4 Sodium fluorescence spectrum

Consider a given volume of sodium atoms in the mesopause region with random thermal motion but with fixed center of mass probed by a monochromatic laser beam at frequency ν, The line shape function (fractional population of a velocity group) of each of six sodium D_2 transition lines due to the Doppler broadening could be derived from equation 3.1 by replacing the velocity with frequency following equation 3.2, i.e., $\upsilon = (\nu - \nu_0)\lambda_0$ with the resonance absorption wavelength $\lambda_0 = c/\nu_0$. The FWHM of line shape is given in equation 3.3:

$$\Delta\nu_D = \nu_0\left(\frac{8k_BT\ln 2}{mc^2}\right)^{1/2} \tag{3.3}$$

where c is the speed of light.

If in addition to the random thermal motion of sodium atoms, the center of mass of the given volume also moves with mesopause region neutral wind with LOS velocity in the direction of the laser beam, V, the required laser frequency would be even higher due to Doppler effect. Now, we would substitute υ in Eq. (3.2) by the net velocity, the atom moves in respond to the collective (wind) and random forces, $\upsilon' = \upsilon + V$, or $\upsilon = \lambda_0(\nu - \nu_0 - V/\lambda_0)$.

Combining the line shape due to Doppler broadening and line shape of Doppler shifting due to wind velocity, we can write down the equation for line shape function of sodium D_2 absorption spectrum by summing each of six transition line shape function together. The final format is expressed in equation 3.4 [Theon et al., 1972; She, 1992].

$$g(\nu,T,V)=\left(\frac{D}{\pi T}\right)^{1/2}\sum_{n=1}^{6}S_n\exp\left[\frac{-D(\nu-\nu_n-V/\lambda_0)^2}{T}\right]=\sum_{n=1}^{6}S_n g_n(\nu,T,V) \qquad (3.4)$$

where

$$g_n(\nu,T,V)=\left(\frac{D}{\pi T}\right)^{1/2}\exp\left[\frac{-D(\nu-\nu_n-V/\lambda_0)^2}{T}\right]$$

$$D=\frac{m\lambda_0^2}{2k_B}=497.8825Kns^2$$

S_n: Relative line strength (from table 3.1)

T: Temperature

ν_n: Line center frequency (6 discrete frequencies at table 3.1)

λ_0: line center of D_2 resonant transition (589.158nm)

Na fluorescence spectra calculated from equation 3.4 with various temperatures and radial wind velocities are shown in figure 3.2. The figure demonstrates that the width of the fluorescence spectrum increases as the temperature increases and the whole spectrum is shifted by a frequency determined by radial wind velocity. It is also clearly shown in the figure 3.2 that the intensity at some frequencies are more sensitive to temperature change and others are more sensitive to radial wind change. In section 3.2 and section 3.3 we form the temperature ratio and wind ratio, and show that we can determine the temperature and LOS wind from backscattering photons received by telescope.

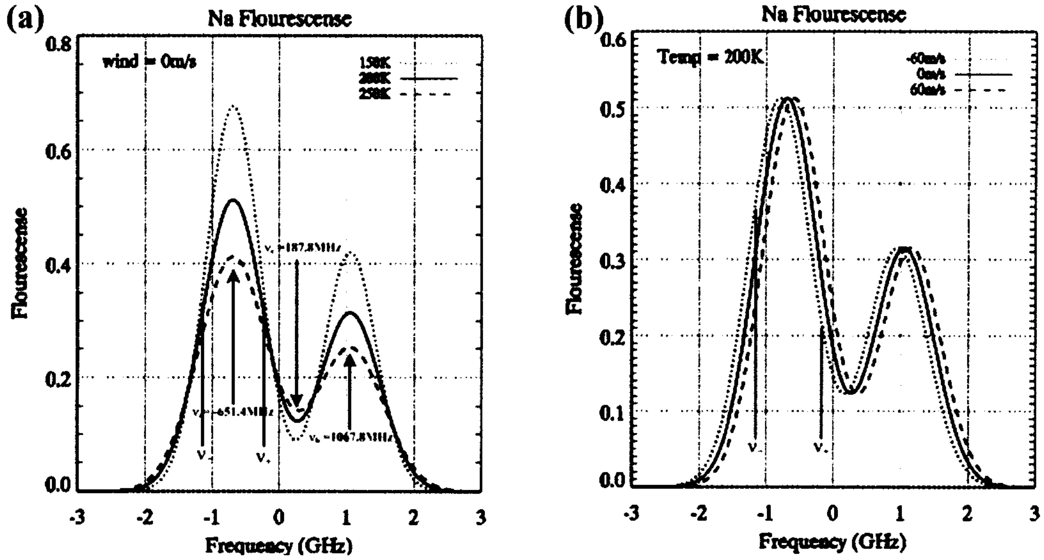

Figure 3.2 Na D_2 absorption spectrum with (a) various temperatures for radial wind velocity = 0m/s, and (b) various radial wind velocities for temperature = 200K. Arrows mark the positions of D_{2a} peak, D_{2b} peak and Crossover. Vertical lines point out the 630MHz downshift and upshift frequencies from D2a peak. CSU lidar system will transmit laser beam into atmosphere at these 3 frequencies.

3.1.5 Laser induced fluorescence (LIF) spectrum

As mentioned above, the sodium absorption spectra calculated from equation 3.4 and plotted in figure 3.2 are idealized by assuming a monochromatic laser beam. Since we are using a pulsed laser in our sodium lidar system with an output laser beam of nearly Gaussian shape and FWHM of ~120MHz [Spectra-Physics Nd:YAG Laser Manual], the effect of laser line width on the absorption (or induced fluorescence) spectrum must be included in the calculation. The spectrum taken the laser lineshape into account is obtained from the correlation of pulsed laser line shape L(ν) with the thermal Doppler-broadened Na D_2 fluorescence spectrum g(ν) [She, et al., 1992], and given by:

$$g_L(\nu,T,V) = Corr(L,g) = \int_{-\infty}^{\infty} L(\nu')g(\nu+\nu',T,V)d\nu' \tag{3.5}$$

Comparison of the theoretical sodium absorption spectrum with that accounting for laser linewidth is plotted in figure 3.3 in section 3.3. It is clearly shown that there is a small, almost negligible difference between the two curves. It is noted that the equation 3.4 is only an approximation of the Voigt function, equation 3.5. In section 3.3 we will calculate the 2D calibration curve from the laser induced fluorescence spectrum derived from the correlation of laser line shape with Voigt function.

3.2 Sodium lidar equation

The lidar equation is the basic equation of importance in the field of lidar remote sensing. It governs the mathematical processes that are used to derive the atmospheric parameters from the backscattering signals received by telescope.

3.2.1 Lidar equation

For sodium fluorescence lidar system, the lidar equation could be explained term by term as below in word format and written down in single pulse format.

(Number of Photons Received) = (Number of Photons Transmitted into atmosphere per Pulse) × (System Efficiency & Atmospheric Transmission below Na Layer) × (Probability of Backscattering per range Δz, per solid angle) × (Solid angle of the receiving telescope) × (Upward & Downward transmission in the Na layer) + (Background Noise & PMT Dark Counts)

$$N(z,\nu_L,T,V)=\left(\frac{E_L}{hc/\lambda_L}\right)\times\left(\eta T_A^2\right)\times\left(\rho_{Na}(z)\sigma_{SB}(\nu_L,T,V)\Delta z\right)\times\left(\frac{A_R}{z^2}\right)\times\left(T_\uparrow T_\downarrow\right)+N_B \quad (3.6)$$

where

$N(z, \nu_L, T, V)$: Number of photons received by telescope from the range ($z-\Delta z/2$, $z+\Delta z/2$), including Na backscattering photons and background noise.

z: Altitude (m)

ν_L: Transmitter laser frequency

T: Temperature (K)

V: Wind velocity (m/s)

E_L: Transmitted laser pulse energy (J)

h: Planck's constant

c: Speed of light

λ_L: Laser wavelength

hc/λ_L: Energy of one photon at wavelength λ_L

η: System efficiency

T_A^2: 2-way atmospheric transmission below Na Layer (below 70km)

ρ_{Na}: Na number density (m^{-3})

σ_{SB}: Na differential backscattering cross section ($m^2\ sr^{-1}$)

Δz: Range resolution or bin size (m)

A_R: Receiving telescope aperture area (m^2)

$T_\uparrow$: Upward transmission in the Na layer

$T_\downarrow$: Downward transmission in the Na layer

N_B: Number of Photons per range interval Δz per pulse due to background noise and dark counts

The left side of the equation is the total number of sodium fluorescence photons received by telescope in a time $2\Delta z/c$, that is, the final photons recorded in a range bin by photon counter board. The first term on the right side of the equation gives the total number of photons transmitted into atmosphere per pulse. They will be attenuated by the lower atmosphere aerosol and air molecules as well as the receiving system efficiency when backscattered photons are received by lidar receiving system, which is expressed in second term in the lidar equation. When the transmitted photons reach the sodium layer, they will interact with sodium atoms resonantly. The interaction will reemit photons in all directions. The third term will tell you of the fraction reemitted photons scattered back from the atoms in a range of Δz, which is the probability of backscattering. Since this probability of backscattering per unit of solid angle, we need consider what fraction of backscattered photons will be finally collected by telescope, which is expressed in the fourth term. When the laser beam travels to the sodium layer, both upward and downward attenuation due to the sodium absorption should not be neglected. Finally the total recorded photons also include the counts due to sky background and PMT dark noise.

3.2.2 Upward and Downward transmissions in sodium layer

Now let us consider a sodium atom in resonance which is moving with an instantaneous velocity υ' away from the lidar station. Once it absorbs a photon at the apparent frequency $\nu_{01} = \nu_L - \upsilon'/\lambda$, it is in the excited state. When this atom fluoresces, it emits a photon with frequency ν_{02} in its rest frame. Since this atom is moving away from the lidar station (in the direction of laser beam) with speed υ', the frequency observed by the lidar receiver is $\nu_{02} - \upsilon'/\lambda = \nu_{01} + \nu_{02} - \nu_L = \nu_k$, which is, surprisingly, independent of υ'. In general, the emission observed by lidar system includes a total of 10 frequencies arising from ten different channels available in sodium D_2 LIF transition. These emission frequencies are listed in table 3.2.

Table 3.2 Frequencies relative to the weighted center of D_2 transition

Ground states	Channel k	ν_k (MHz)
Lower ground state: 1	0	$2\nu_{31}-\nu_L = 2081.6-\nu_L$
	1	$2\nu_{41}-\nu_L = 2113.2-\nu_L$
	2	$2\nu_{51}-\nu_L = 2182.1-\nu_L$
	3	$\nu_{41}+\nu_{42}-\nu_L = 341.6-\nu_L$
	4	$\nu_{51}+\nu_{52}-\nu_L = 410.5-\nu_L$
Upper ground state: 2	5	$2\nu_{32}-\nu_L = -1430-\nu_L$
	6	$2\nu_{42}-\nu_L = -1361.1-\nu_L$
	7	$2\nu_{52}-\nu_L = -1243.2-\nu_L$
	8	$\nu_{42}+\nu_{41}-\nu_L = 341.6-\nu_L$
	9	$\nu_{52}+\nu_{51}-\nu_L = 410.5-\nu_L$

When emitted photons travel downward from a level at z, they are attenuated by the sodium layers below. Therefore the downward transmission includes the transmissions at a total of ten terms (eight different frequencies), whereas the upward transmission is only at the laser frequency ν_L. A layer of width Δz at an altitude of z will attenuate the upward beam at the laser frequency and the downward beam at one of ten frequencies by factors:

$$T_{\uparrow}(z+\Delta z,T,V) = T_{\uparrow}(z,T,V)\exp[-\rho_{Na}(z)\sigma_{SA}(\nu_L,T,V)\Delta z] \qquad (3.7)$$

$$T_{\downarrow}^{k}(z+\Delta z,T,V) = T_{\downarrow}^{k}(z,T,V)\exp[-\rho_{Na}(z)\sigma_{SA}(\nu_k,T,V)\Delta z] \qquad (3.8)$$

where

σ_{SA}: The sodium total absorption cross section.

k: Index for one of ten channels (0, 1, …., 9)

Usually we start z at 70km and set the transmission in the Na layer below 70km as unity. Then we compute the upward and downward transmissions from a range bin at altitude z to Na bottom layer at z_b = 70km. The total effective downward transmission can be calculated by summing the transmissions at ten frequencies weighted by a branching ratio (the probability of a resonantly backscattered photon emitted through the kth channel), and given by:

$$T_{\downarrow Eff} = \sum_{k=0}^{9} \frac{\sigma_{SB}(\nu_k, T, V)}{\sigma_{SB}^{total}(\nu_L, T, V)} T_{\downarrow}^{k} \tag{3.9}$$

where

$\sigma_{SB}^{total}(\nu_L, T, V) = \sum_{k=0}^{9} \sigma_{SB}(\nu_k, T, V)$: The total sodium backscattering cross section

$\frac{\sigma_{SB}(\nu_k, T, V)}{\sigma_{SB}^{total}(\nu_L, T, V)}$: Branching ratio

In the daytime when the Faraday filter effectively blocks sky background, the backscattered photons received by telescope will also be attenuated when passing through the filter. As a result, the frequency dependent transmission through Faraday filter must be included in the total effective downward transmission.

$$T_{\downarrow Eff} = \sum_{k=0}^{9} \frac{\sigma_{SB}(\nu_k, T, V)}{\sigma_{SB}^{total}(\nu_L, T, V)} T_{\downarrow}^{k} T_{filter}^{k} \tag{3.10}$$

3.2.3 Rayleigh backscattering lidar equation

Below the Na layer (usually below 70km), the photons received by telescope arise from the Rayleigh and aerosol backscattering. For our case, we are interested in the Rayleigh return signals at 20-40km, which will be used to do normalization of the powers at three operating laser frequencies and also to calculate the sodium density. The Rayleigh backscattering signals received by telescope are governed by Rayleigh lidar equation, which is given by:

$$N_R(z,\nu_L)=\left(\frac{E_L}{hc/\lambda_L}\right)\left(\eta T_A^2(z)\right)\left(\rho_{air}(z)\sigma_{RB}(\nu_L)\Delta z\right)\left(\frac{A_R}{z^2}\right)+N_B \tag{3.11}$$

Where

$T_A^2(z)$: 2-way atmospheric transmission below altitude z

ρ_{air}: Number density of air molecules (m^{-3})

σ_{RB}: Rayleigh backscattering cross section ($m^2\ sr^{-1}$)

In order to simplify the calculation of sodium density, we reasonably assume that the atmospheric transmission between 30 km to sodium bottom layer (70km) is 1. We will discuss the sodium density calculation in detail in section 3.3.

3.2.4 Theoretical number of Photons

Now it is supposed that we are observing the sodium fluorescence backscattered photons in the laboratory without the necessity to consider atmospheric conditions between telescope and sodium layer. In the other words, there are no background and no Na extinction, and photons received by telescope are also normalized to the sum of the Rayleigh signals at 20km-40km. The photons obtained in this way are called "background subtracted and Rayleigh normalized received photons" or "theoretical photons" and at the three frequencies are labeled as $N_{0,+,-}$. For historical reason, in the 3-frequency CSU sodium lidar system, we are using N_0 for theoretical photons at D_{2a} peak frequency, N_+ at + 630MHz frequency, and N_- at –630 MHz frequency, respectively, labeled by indices 1, 0, and 2 in our analysis program.

$$N_j = \frac{\left(N(z,\nu_j,T,V) - N_{Bj}\right)}{\left(T_{\uparrow j} T_{\downarrow Effj}\right) \sum_{z_R=20km}^{40km} \left(N_R\left(z_R,\nu_j\right) - N_{Bj}\right)} \tag{3.12}$$

where

j = 0, +, -, for the frequencies of ν_{D2a}, ν_+, ν_-

The theoretical number of photons at 3 laser operating frequencies collected by sodium lidar system will be used to construct the experimental temperature and wind ratios. Whereas the equation above can also be used to derive the theoretical temperature and wind ratios related to backscattering cross section and form the 2D calibration curves for determination of temperature and wind. We will discuss them in the following.

3.3 Experimental ratios and 2D calibration curves

3.3.1 Temperature and wind ratios

Since at a given incident frequency, the absorption and backscattering cross sections, calculated from laser induced sodium fluorescence spectrum, depend on both temperature and wind, we should be able to retrieve atmospheric temperature T and wind V from these cross sections. It is desirable to conduct ratio measurements in sodium lidar system, rather than scanning laser frequency across the sodium spectrum. In order to determine two unknown, T and V, with ratio measurements, one needs to probe the atmosphere with three independent observations. Therefore CSU sodium lidar system sends out three frequencies at D_{2a} peak ν_{D2a}, +630MHz ν_+, and -630MHz ν_-, and receives photons from each of these frequencies separately. Two signal ratios are formed, the temperature ratio R_T which is most sensitive to temperature change, and the wind ratio R_V which is most sensitive to radial wind velocity change. The experimental ratios can be expressed in terms of the ratios of theoretical number of photons at 3 frequencies by:

$$R_T(T,V) = \frac{N_+ + N_-}{2N_0} = \frac{\sigma_{SB}^{total}(\nu_+,T,V) + \sigma_{SB}^{total}(\nu_-,T,V)}{2\sigma_{SB}^{total}(\nu_0,T,V)} \tag{3.13}$$

$$R_V(T,V) = \frac{N_+ - N_-}{N_0} = \frac{\sigma_{SB}^{total}(\nu_+,T,V) - \sigma_{SB}^{total}(\nu_-,T,V)}{\sigma_{SB}^{total}(\nu_0,T,V)} \tag{3.14}$$

where N_+, N_0, N_-: theoretical number of photons at frequencies of ν_+, ν_{D2a}, ν_-

According to the equations 3.6, 3.11 and 3.12, the theoretical temperature and wind ratios are also expressed in terms of the ratio of total backscattering cross sections, which depend only on frequency, temperature, and wind and not on the extinctions. Since we know frequencies very well, comparison between experimental ratios and theoretical ratios will allow determination of temperature and radial wind velocity.

3.3.2 2D calibration curve

The Na spectrum function expressed in equation (3.4) is the approximate form considering only Doppler broadening and assuming the natural line width $\Delta\nu \ll \Delta\nu_D$. If the natural line broadening is included into Gaussian function of Na spectrum, the exact Na spectrum function can be given in terms of Voigt function by:

$$g_n\left[\left(\nu - \frac{V}{\lambda_0} - \nu_n\right), T\right] = \int G\left(\frac{\upsilon}{\lambda_0}, T\right) g_n\left(\nu - \frac{V}{\lambda_0} - \nu_n - \frac{\upsilon}{\lambda_0}\right) d\left(\frac{\upsilon}{\lambda_0}\right) \qquad (3.15)$$

where

$$G\left(\frac{\upsilon}{\lambda_0}, T\right) = \left(\frac{D}{\pi T}\right)^{1/2} \exp\left[\frac{-D(\upsilon/\lambda_0)^2}{T}\right]$$

$$g_n\left(\nu - \frac{\upsilon + V}{\lambda_0} - \nu_n\right) = \frac{\Delta\nu_n}{2\pi\left[\left(\nu - \frac{\upsilon + V}{\lambda_0} - \nu_n\right)^2 + \left(\frac{\Delta\nu_n}{2}\right)^2\right]}$$

υ: Thermal velocity

V: LOS Wind velocity

ν: Frequency

ν_n: One of six discrete frequencies in D_2 transition

$\Delta\nu_n$: Line width of Lorentzian line shape

Correlation of Voigt function with laser line shape must be done by using equation (3.5) before the absorption cross section is obtained. The total absorption cross section is expressed by [She et al., 1992]:

$$\begin{aligned}\sigma_{SA}(\nu,T,V)&=A_0\left(\frac{g_2}{g_1}\right)\left(\frac{\lambda_0^2}{8\pi}\right)g_L(\nu,T,V) \qquad (3.16)\\ &=\frac{\lambda^2}{8\pi}\{\frac{N_1}{N}[2g_{31L}(\nu-\frac{V}{\lambda}-\nu_{31},T)+5g_{41L}(\nu-\frac{\mathrm{V}}{\lambda}-\nu_{41},T)+5g_{51L}(\nu-\frac{\mathrm{V}}{\lambda}-\nu_{51},T)]\\ &+\frac{N_2}{N}(\frac{3}{5})[g_{32L}(\nu-\frac{\mathrm{V}}{\lambda}-\nu_{32},T)+5g_{42L}(\nu-\frac{\mathrm{V}}{\lambda}-\nu_{42},T)+14g_{52L}(\nu-\frac{\mathrm{V}}{\lambda}-\nu_{52},T)]\}\frac{\mathrm{A}_0}{6}\end{aligned}$$

where

A_0: Einstein coefficient for Na D_2 transition ($0.06289\mathrm{ns}^{-1}$)

g_2/g_1: Degeneracy ration ($g_2/g_1 = 2$ for D2 transition)

N_1, N_2, and N: lower, upper, and total ground state population, $N = N_1 + N_2$

$$\frac{N_1}{N}=\frac{3}{3+5\exp\left(-\frac{0.08502656}{T}\right)}; \quad \text{and} \quad \frac{N_2}{N}=\frac{5\exp\left(-\frac{0.08502656}{T}\right)}{3+5\exp\left(-\frac{0.08502656}{T}\right)}$$

The total absorption cross sections of sodium D_2 transition at 0 wind velocity and 200K temperature calculated from equation (3.16) exactly with Voigt function and approximately with corresponding Gaussian function are shown in figure 3.3. The 2 curves look almost identical, except the peaks of approximation curve are a little higher than those of exact curve. It is a good approximation to replace the Voigt function by Gaussian function if one wants to reduce the complexity of sodium D_2 spectrum. Notice that the cross section is temperature dependent, and at 200K, absorption cross section at the higher peak is approximately 9.5×10^{-16} m^2 and the corresponding differential cross section is 7.6×10^{-17} m^2sr^{-1}.

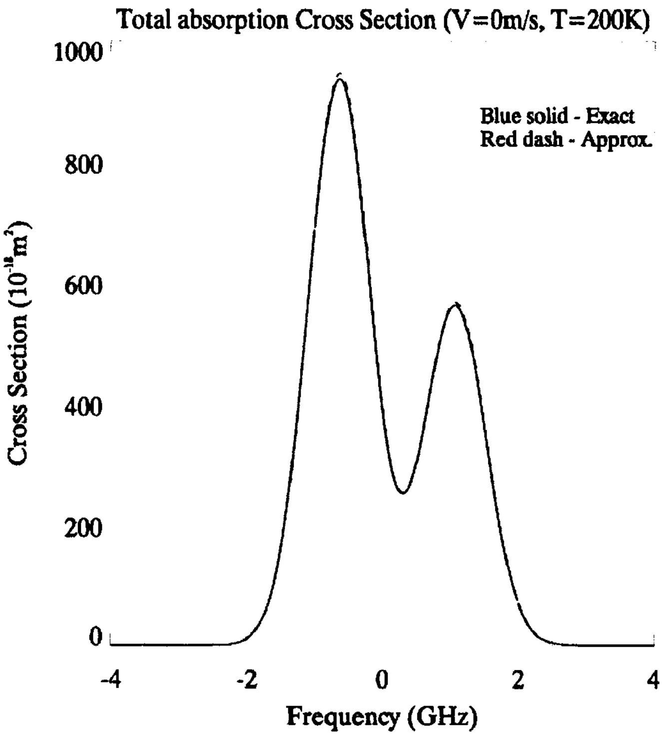

Figure 3.3 Absorption Cross sections of sodium D_2 transition. Solid line is calculated from Voigt functions which include the effects of Doppler broadening and natural line broadening. Dash line is approximately calculated from Gaussian function. Notice the slight difference in the extrema.

The total backscattering cross section $\sigma_{SB}^{total}(\nu_L,T,V)=\sum_{k=0}^{9}\sigma_{SB}(\nu_k,T,V)$ used in the theoretical ratios in equations (3.13) and (3.14) could be calculated from the absorption cross section by equation $\sigma_{SB}(\nu_k,T,V)=\frac{\sigma_{SA}(\nu_k,T,V)}{4\pi}HF^k$ where HF stands for Hanle factor, and $HF^k = 1$ for no Hanle effect. Including the Hanle effect [Corney, 1977] HF^k is the constant for each channel to account for the effect of spherical symmetry broken by the presence of laser electric field [Chen, 1997]. Due to different populations of two ground states, N_1 and N_2, in the sodium D_2 transition which are dependent on temperature and assuming thermal equilibrium, the backscattering cross section used here is in fact the effective cross section, a multiplication of backscattering cross section by probability of a sodium atom excited from one of two ground states. Table 3.3 shows the backscattering cross section at ten path ways, with HF^k accounted for in the last column. Using equations (3.13) and (3.14), $\sigma_{SB}^{total}(\nu_L,T,V)=\sum_{k=0}^{9}\sigma_{SB}(\nu_k,T,V)$ and Table 3.3, we can construct the 2-dimensional calibration curve, shown in figure 3.4, relating the theoretical temperature and wind ratios, R_T and R_V, to temperatures and LOS winds.

Table 3.3 Effective backscattering cross section at ten channels with Hanle effect included [She, private communication, 2005]

Ground states	Channel k	ν_k (MHz)	Effective backscattering Cross section
Lower ground state 1	0	$2\nu_{31}-\nu_L$ $=2081.6-\nu_L$	$\left(\frac{\lambda_0^2}{8\pi}\right)\left(\frac{N_1}{N}\right)\left[2g_{31}\left(\nu_L-\frac{V}{\lambda_0}-\nu_{31}\right)\right]\left(\frac{A_0}{6}\right)$
	1	$2\nu_{41}-\nu_L$ $=2113.2-\nu_L$	$\left(\frac{\lambda_0^2}{8\pi}\right)\left(\frac{N_1}{N}\right)\left[5.5g_{41}\left(\nu_L-\frac{V}{\lambda_0}-\nu_{41}\right)\right]\left(\frac{A_0}{6}\right)$
	2	$2\nu_{51}-\nu_L$ $=2182.1-\nu_L$	$\left(\frac{\lambda_0^2}{8\pi}\right)\left(\frac{N_1}{N}\right)\left[5g_{51}\left(\nu_L-\frac{V}{\lambda_0}-\nu_{51}\right)\right]\left(\frac{A_0}{6}\right)$
	3	$\nu_{41}+\nu_{42}-\nu_L$ $=341.6-\nu_L$	$\left(\frac{\lambda_0^2}{8\pi}\right)\left(\frac{N_1}{N}\right)\left[5.5g_{41}\left(\nu_L-\frac{V}{\lambda_0}-\nu_{41}\right)\right]\left(\frac{A_0}{6}\right)$
	4	$\nu_{51}+\nu_{52}-\nu_L$ $=410.5-\nu_L$	$\left(\frac{\lambda_0^2}{8\pi}\right)\left(\frac{N_1}{N}\right)\left[5g_{51}\left(\nu_L-\frac{V}{\lambda_0}-\nu_{51}\right)\right]\left(\frac{A_0}{6}\right)$
Upper ground state 2	5	$2\nu_{32}-\nu_L$ $=-1430-\nu_L$	$\left(\frac{\lambda_0^2}{8\pi}\right)\left(\frac{N_2}{N}\right)\left(\frac{3}{5}\right)\left[0.98g_{32}\left(\nu_L-\frac{V}{\lambda_0}-\nu_{32}\right)\right]\left(\frac{A_0}{6}\right)$
	6	$2\nu_{42}-\nu_L$ $=-1361.1-\nu_L$	$\left(\frac{\lambda_0^2}{8\pi}\right)\left(\frac{N_2}{N}\right)\left(\frac{3}{5}\right)\left[5g_{42}\left(\nu_L-\frac{V}{\lambda_0}-\nu_{42}\right)\right]\left(\frac{A_0}{6}\right)$
	7	$2\nu_{52}-\nu_L$ $=-1243.2-\nu_L$	$\left(\frac{\lambda_0^2}{8\pi}\right)\left(\frac{N_2}{N}\right)\left(\frac{3}{5}\right)\left[15.68g_{52}\left(\nu_L-\frac{V}{\lambda_0}-\nu_{52}\right)\right]\left(\frac{A_0}{6}\right)$
	8	$\nu_{42}+\nu_{41}-\nu_L$ $=341.6-\nu_L$	$\left(\frac{\lambda_0^2}{8\pi}\right)\frac{N_2}{N}\left(\frac{3}{5}\right)\left[5g_{42}\left(\nu_L-\frac{V}{\lambda_0}-\nu_{42}\right)\right]\left(\frac{A_0}{6}\right)$
	9	$\nu_{52}+\nu_{51}-\nu_L$ $=410.5-\nu_L$	$\left(\frac{\lambda_0^2}{8\pi}\right)\frac{N_2}{N}\left(\frac{3}{5}\right)\left[15.68g_{52}\left(\nu_L-\frac{V}{\lambda_0}-\nu_{52}\right)\right]\left(\frac{A_0}{6}\right)$

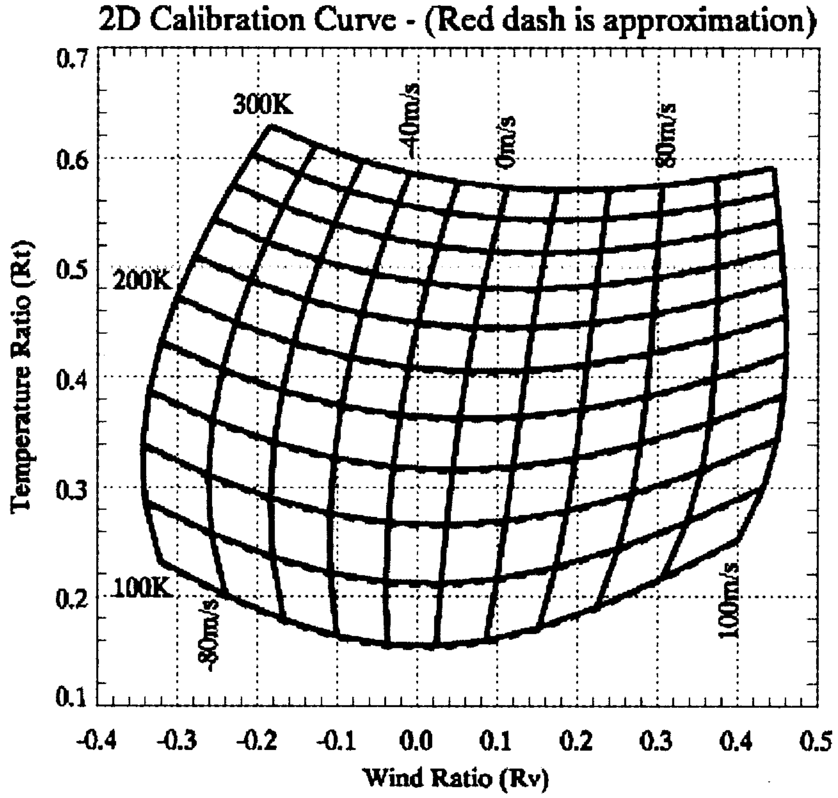

Figure 3.4 2D calibration curves constructed from numerical calculations. The temperature and wind ratios are both theoretical computed from spectrum of laser induced sodium fluorescence. Solid lines are calculated from exact spectrum of Voigt function, whereas the dash lines are calculated from approximate spectrum of Gaussian function. Calibration curves may be used to retrieve temperature and radial wind velocity by using the experimental temperature and wind ratios.

In data analysis, we use much finer grids. With higher resolution grids, each pair of temperature ratio R_T and wind ratio R_V will fall into a particular box, and the corresponding temperature and wind velocity pair can be determined by using a bilinear expansion in temperature and velocity differences within this box.

3.3.3 Sodium density calculation

Before the upward transmission and downward transmission, which depend on Na density, for an altitude bin are calculated, the sodium density for this altitude bin must be determined from the equation below once we already have the temperature and radial wind velocity of this altitude bin.

$$
\begin{aligned}
N(z,\nu_L,T,V)-N_B &= \frac{\left(N_R(z_{\mathrm{Re}},\upsilon_L,T,V)-N_B\right)}{\rho_R(z_{\mathrm{Re}})\sigma_R\left(z_{\mathrm{Re}},\nu_L,T,V\right)}\frac{z_{\mathrm{Re}}^2}{z^2}T_{\uparrow}\rho_{Na}(z)\sigma_{SB}^{total}(z,\nu_L,T,V)T_{\downarrow Eff} \\
\Rightarrow \rho_{Na}(z) &= \frac{\left(N(z,\nu_L,T,V)-N_B\right)}{\left(N_R(z_{\mathrm{Re}},\upsilon_L,T,V)-N_B\right)}\bullet\frac{\sigma_R\left(z_{\mathrm{Re}},\nu_L,T,V\right)}{\sigma_{SB}^{total}(z,\nu_L,T,V)}\bullet\frac{z^2}{z_{\mathrm{Re}}^2}\bullet\frac{\rho_{\mathrm{Re}}(z_R)}{T_{\uparrow}T_{\downarrow Eff}}
\end{aligned}
\tag{3.17}
$$

Usually we set reference altitude $z_{\mathrm{Re}} = 30km$, and the Rayleigh backscattering photon counts at the altitude range 25km-35km received by telescope are fit to the formula $f(z)=\left(B_j/z^2\right)\exp\left(-A_j z\right)$. Then the Rayleigh signal at the reference altitude may be accurately evaluated from the two coefficients A_j and B_j. The air density at reference altitude is determined by MSIS-E-90 atmospheric model and given by $\rho_R = 3.249 \times 10^{23}$ m^{-3}. Notice that we only need one frequency to derive the sodium density.

3.4 Data analysis for temperature, wind, and sodium density

The photon counter board in our lidar system sums the electrical pulses generated by returning photons in the PMT based on tabulated altitude bins according to the time of flight of laser beam. Integration of 2000 shots for each of 3 laser frequencies (a total of 6000 shots and a total time of 2 minutes for 50Hz pulse Nd:YAG) generates a 2-minute raw data file. There are 4 columns in each of these 2-minute raw data files with first column representing altitudes in kilometers and following columns representing photon counts at three laser frequencies ordered by D_{2a} peak, +630MHz, and -630MHz. An example of the vertical profiles of raw photons at three frequencies from typical nighttime and daytime 2-minute raw data files is shown in figure 3.5.

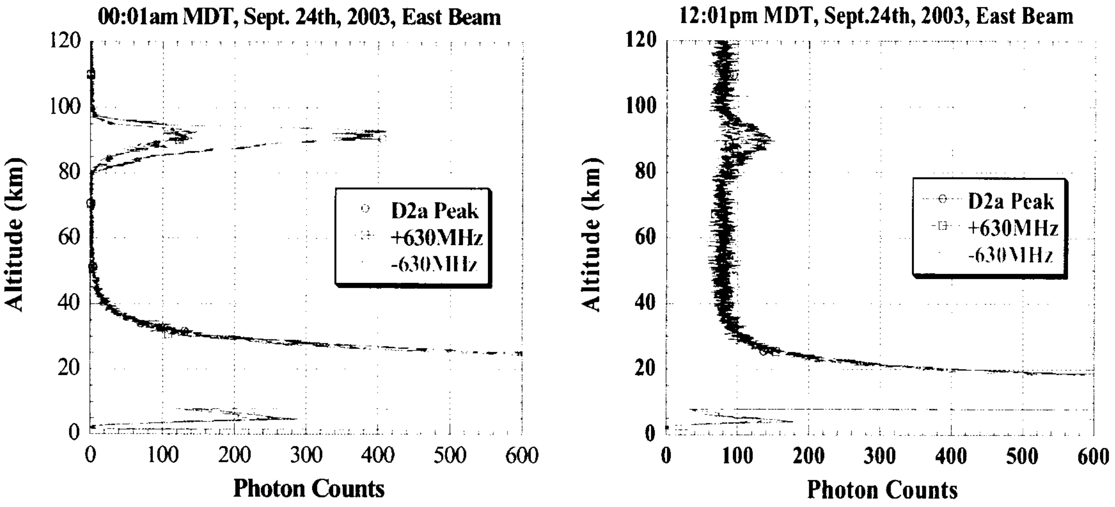

Figure 3.5 Vertical profiles of raw photons with 2-minute integration (a) at nighttime and (b) at daytime. Three colors represent three frequencies with green for D2a peak, blue for +630MHz, and red for -630MHz. Daytime profiles are much noisier than nighttime profiles due to higher background in the daytime even using Faraday filter to dramatically reduce the skylight background. At the same time, the Faraday filter decreases the return signal by a factor of 4.

In addition, some other experimental information, such as lidar site location, laser beam direction number, lidar site altitude, arrangement of size and binning, acquisition starting time, and acquisition duration, can also be found inside the raw data file. All this information is required as inputs by IDL analysis programs of nearly 10,000 lines developed by Prof. David A. Krueger for over a decade with various improvements added at different times. The analysis programs will first eliminate the bad files, based on certain criteria for nighttime data and manual selection for daytime data, which are noisier as can be seen in Fig. 3.5. The good files are summed by corresponding bins and frequencies according to preferred integration time interval of usually 15 minutes for nighttime data and 30 minutes for daytime data. This section will just summarize the procedure for the raw data files step-by-step.

3.4.1 Bad file selection

Since our sodium lidar system is intended to run multiple 24-hour continuous campaign, 720 files could be generated in one day. In these files, there are some bad files due to loss of locking (rarely occur), clouds which block the laser beam, or other system problems. To avoid contamination of the temperature, wind, and sodium density results, all the bad files should be removed prior to any analysis. As for raw data files in the nighttime, a criteria file is read by analysis program and used for automatic diagnostic tests. These tests mainly include trend tests, which make sure that the total sodium counts from 83km to 105km as well as the total Rayleigh counts from 25km to 35km do not vary from current file to the three files before and after by more than some reasonable value (around 20%), ratio tests, which calculate the approximate layer-averaged temperature and wind ratio to make sure that the ratios are within the range of physically realistic values, and minimum count tests, which insure that the signals meet a minimum acceptable level. All the files which do not satisfy these tests are treated as bad files and removed. However, due to high background in the daytime data, it is difficult to set up a criteria file to automatically remove bad files. We manually remove the bad files by visually inspecting photon profiles based on personal judgment.

3.4.2 Time integration and background subtraction

All the good files, either passing the criteria in the nighttime or visual inspection in the daytime, are summed over corresponding bins and frequencies according to preset integration time intervals to form a composite vertical profile of photon counts at each of three frequencies. For dynamics studies, usually in the nighttime the integration time interval is 15 minutes and in the daytime is 30 minutes. Then the analysis program will subtract the background taken as the signal averaged over 125km-155km, where no counts are believed to arise from Rayleigh and sodium backscattering, from each altitude bin in the composite vertical profile. Our regular analysis uses hourly averages, and the retrieved hourly mean Na desity, zonal and meridional wind profiles are deposited in the CEDAR data base for community uses.

3.4.3 Power normalization and vertical smoothing

Since, due to the AO modulator optics our sodium lidar system transmits somewhat different laser powers at each of three operating frequencies, and due to varied lower atmospheric absorption, power normalization must be used. The background subtracted photon counts at sodium layer are normalized to the corresponding lower atmosphere Rayleigh backscattering photon counts summed from 20km-40km, which statistically establish the best estimate for relative laser power of each frequency. After the normalized photon counts are generated at each altitude bin (each bin at sodium layer from 70km to 120km is 150m), they are vertically smoothed by using a Hanning window with FWHM of 31 bins for 2 km resolution.

3.4.4 Determination of temperature, wind, and sodium density

At the lowest altitude bin of the sodium layer, the upward and downward transmissions are assumed to be unity. The experimental temperature and wind ratios are calculated for the first bin, and then the temperature and LOS wind velocity may be determined by using a 2D calibration curve, such as shown in figure 3.4. Total absorption cross section and total backscattering cross section for a given laser frequency in this altitude bin are calculated according to equation 3.16 and table 3.2. After that, the sodium density is determined from equation 3.17 by involving only one frequency; we use the un-shifted frequency, which has more photons. Once temperature, wind, and sodium density are obtained in the lowest altitude bin, the upward and downward transmissions through that layer are evaluated and used in the calculation of the temperature, wind, and sodium density in next highest layer. This is the iterative procedure for determination of altitude-resolved temperature, radial wind velocity, and sodium density altitude by altitude.

3.4.5 Chirp velocity correction for radial wind velocity

Each chirp velocity due to frequency shift of output laser beam from the desired frequency as determined by c.w. Doppler-free spectroscopy is computed in the analysis program for every two-minute profile. All the chirp files corresponding to good photon profile files will be summed and averaged over integration time interval, i.e., 2 min, to form an averaged chirp velocity, and then this averaged chirp velocity will be subtracted from radial wind velocity at each altitude bin. Usually the chirp velocity correction varies from 1m/s to 4m/s.

3.4.6 Some examples of vertical profiles of temperature, wind, and sodium density

To illustrate the results of sodium density, temperature, zonal wind, and meridional wind observed by our lidar system, we choose two profiles (both nighttime at 07:30 UT and daytime at 19:30 UT) in a particular one day (Sept. 24th, 2003) obtained in a record breaking 9-day continuous campaign to plot in figure 3.6. The detailed discussions on dynamics and waves in the temperature, zonal wind, and meridional wind components will be presented in chapter 5.

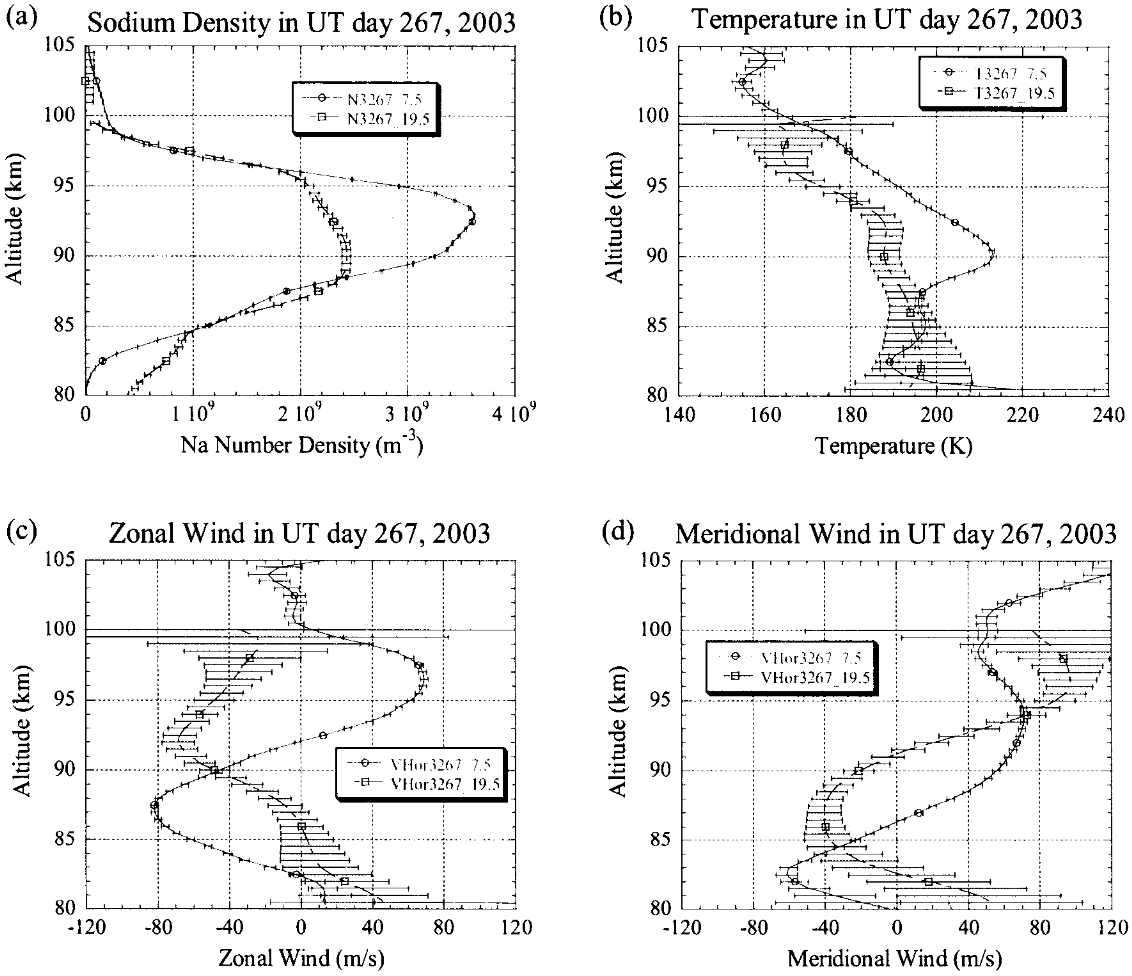

Figure 3.6 Hourly mean vertical profiles of (a) sodium density, (b) temperature, (c) zonal wind, and (d) meridional wind observed by CSU sodium lidar at midnight 07:30UT and noon 19:30UT (worst case scenario) in UT day 267, 2003.

Reference:

Chen, H., M. A. White, D. A. Krueger, and C. Y. She, Daytime Mesopause Temperature Measurements using a Sodium-Vapor Dispersive Faraday Filter in a Lidar Receiver, *Opt. Lett.*, 21, 1093-1095, 1996.

Chen, H., A Sodium Fluorescence Lidar for Daytime Operation Using a Dispersive Faraday Filter, *PhD Dissertation*, Colorado State University, 1997.

Chen, S., 24 Hour Lidar Campaigns and Tidal Analysis, *PhD Dissertation*, Colorado State university, 1999.

Corney, A., *Atomic and Laser Spectroscopy*, Oxford, 39, 1977.

Hartig, W., H. Walther, High-resolution spectroscopy and frequency stabilization of a cw laser, *App. Phys.*, 1, 171-174, 1973.

She, C. Y., J. R. Yu, H. Latifi, and R. E. Bills, High-Spectral-Resolution Fluorescence Lidar for Mesospheric Sodium Temperature Measurements, *Appl. Opt.*, 31, 2095-2106, 1992.

She, C.Y., J. R. Yu, Simultaneous Three-Frequency Na Lidar Measurements of Radial Wind and Temperature in the Mesopause Region, *Geophys. Res. Lett.*, 21, 1771-1774, 1994.

She, C. Y., and J. R. Yu, Doppler-free saturation fluorescence spectroscopy of Na atoms for atmospheric application, *Appl. Opt.*, 34(6), 1063-1075, 1995.

Theon, J. S., The Mean Observed Structure and Circulation of the Stratosphere and Mesosphere, *NASA Tech. Rep.*, TR-375, 1972.

White, M. A., A Frequency-agile Na Lidar for the Measurement of Temperature and Velocity in Mesopause Region, *PhD Dissertation*, Colorado State University, 1999.

Wiese, W. L., W. M. Smith, B. M. Miles, *Atomic Transition Probabilities*, Vol.II-Sodium, NSRDS-NBS 22, 2, 1969.

Yu, J. R., A Sodium Wind/Temperature Lidar and Observed Mesopause Thermal Structure over Fort Collins, CO, *PhD Dissertation*, Colorado State University, 1994.

Yu, J. R., C. Y. She, Climatology of a midlatitude mesopause region observed by a lidar at Fort Collins, Colorado (40.6N, 105W), *J. Geophys. Res.*, 100, 7441-7452, 1995.

Chapter 4: Atmospheric solar tides, planetary waves, and gravity waves

Scientists interested in the physics and chemistry of the Mesosphere and Lower Thermosphere region (MLT) have increasingly come to recognize the importance of atmospheric waves of all types. Gravity/buoyancy waves, planetary waves, and tidal waves pervade the upper atmosphere and are, in fact, ubiquitous features of all planetary atmospheres. These waves generated by dynamical processes propagate vertically and horizontally, dissipate, interact non-linearly, and profoundly influence the flows of momentum, energy, and constituents on a global basis [Killeen, et al., 1995]. This chapter provides a brief review on the atmospheric solar tides in section 4.1, planetary waves in section 4.2, gravity waves in section 4.3, and nonlinear interactions among these waves in section 4.4.

4.1 Atmospheric solar tides

Atmospheric solar tides are global-scale oscillations in temperature, wind, density, and pressure at periods that are subharmonics of a solar day. They include migrating components and non-migrating components. Migrating tidal components propagate westward with the apparent motion of the sun, so their zonal wave numbers are identical to their frequency (in units of "tide maxima per day"). These components are thermally driven by the local periodic absorption of solar radiation throughout the atmosphere, primarily the absorption of UV radiation by stratospheric ozone and of IR radiation by water and water vapor in the troposphere. Since the migrating tides do not move relative to the sun, they act as a steady influence on the atmosphere. Their variation in time to an observer on Earth results from the Earth's rotation through this fixed excitation pattern. These tides have been studied extensively with mechanistic models for more than 30 years [Chapman and Lindzen, 1970; Forbes et al., 1997; Hagan et al., 1998]. Ground-based and satellite-borne wind and temperature measurements reveal that the tides often govern the dynamics of Mesosphere and Lower Thermosphere (MLT) region. However, there are features in the measurements that remain unresolved by current numerical models based on either mechanistic approaches or first principles. Part of the discrepancy may be due to the contribution to the total tide of the non-migrating component. Non-migrating tidal components are also harmonics of a solar day, but unlike migrating tides, their zonal wavenumber do not have to be equal to their frequency. This means that they may be stationary, or propagate either eastward or westward. Their driving sources appear to be dominated by the latent heat [Hagan and Forbes, 2002 and 2003] which is stored in water vapor and transported by complex meteorological activity, to be released again in other regions of the globe when the vapor precipitates.

According to the conservation of energy and the decrease in air density, the upward propagating tidal waves increase in amplitude with altitude. However, wave dissipation or damping effects become important in the middle and upper atmosphere. Between 80-100km in the mesopause region, gravity waves become large enough to interfere with diurnal tides via the deposition of momentum and energy through wave breaking. Depending on the tidal phase, the net effect is to either decrease or increase the wind amplitude at these altitudes. Above 90-100km in the lower thermosphere, the decreasing density of the air reduces the efficiency of mixing, and the tides are damped by molecular diffusion. Above the thermosphere, tides are dissipated by the radiation of energy into space (Newtonian cooling) and drag caused by the tidal acceleration of charged particles in the ionosphere (ion drag) [Hagan et. al., 1997].

4.1.1 Brief history of atmospheric solar tides

Atmospheric tides were not observed until the barometer was invented by Torricelli in 1643. At that time, Newton [1687] explained the dominance of the lunar semidiurnal component in the sea tides, and realized that tidal forces must also affect the atmosphere, but thought the effect too small to be observed. However, later observations showed that atmospheric surface pressure tides are primarily dominated by solar semidiurnal variations. Therefore Laplace concluded that the solar dominance implied a thermal origin. In 1882 Lord Kelvin raised an old puzzle: Since thermal forcing indicates the predominance of the diurnal variation in surface pressure oscillation, then why is the semidiurnal surface pressure oscillation larger and more regular than the diurnal? Kelvin hypothesized that the atmosphere had a free resonant oscillation with zonal wavenumber = 2 and a period = 12 hours. This hypothesis dominated the thinking on atmospheric tides inconclusively for 70 years due to uncertainties in atmospheric structure. After World War II, the real atmospheric temperature structure was observed directly. Jacchia and Kopal [1951] concluded that semidiurnal modes did not coincide with any free oscillation mode of the atmosphere. After the resonance theory, scientists were searching for additional sources of thermal forcing. Siebert [1961] pointed out that the absorption by water vapor in the troposphere could account for 1/3 of the observed semidiurnal surface pressure oscillation (which is right). But he also concluded that ozone heating was relatively small (which is wrong). Butler and Small [1963] found out that ozone absorption in fact accounted for the remaining 2/3 of the semidiurnal surface oscillation. Finally, Lindzen [1967] carried out the theoretical calculations for the diurnal tide with satisfactory answers for the observed features. Since that time a basic understanding of the solar tides and their driven forces was developed, as well as an answer to Lord Kelvin's puzzle. In brief, semidiurnal tides with large vertical wavelengths could be excited rather efficiently by the deep ozone heating and thus can easily propagate to the ground. Uniform distribution of ozone heating determines semidiurnal tide; it is more regular than diurnal tide. In contrast, the diurnal tide near equator between ±30° forced by deep ozone heating tends to interfere destructively, and consequently have a small amplitude at the ground. Poleward of 30°, the diurnal tide is vertically trapped and confined to the source region and hard to reach the ground. Water vapor heating (intermittent in space and time) in the troposphere can excite diurnal tide quite efficiently. The resulting surface pressure diurnal oscillation is also intermittent. This is the basic reason why the semidiurnal surface pressure oscillation is larger and more regular than the diurnal. Recently, the Global Scale Wave Model (GSWM) was developed by scientists at the National Center for Atmospheric Research (NCAR) [Hagan et al., 1999]. In the GSWM, the linearized Navier-Stokes equations on a rotating sphere for steady-state global temperature and wind perturbations are integrated numerically in order to obtain the thermally-driven response for either a diurnal or semidiurnal atmospheric tide, or an "unforced" planetary wave response for a specified period and zonal wavenumber.

The tidal comparisons between the GSWM and ground-based instruments (such as radar and lidar) show excellent agreement on the diurnal component; there is less agreement, however, on the semidiurnal component [She et al., 2004; Pancheva et al., 2002].

4.1.2 Mathematical approach to atmospheric solar tides

The linearized dynamical equations governing atmosphere motions are usually the coupled equations describing the mean states and the perturbations. To simplify these equations, we assume that the background state is a resting hydrostatic isothermal atmosphere. The linearized equations will be decoupled under these assumptions. Then the resulting linearized equations for the perturbations on a spherical isothermal atmosphere are given by [Holton, 1975; Forbes, 1995]:

Zonal momentum:
$$\frac{\partial u'}{\partial t} - 2\Omega v'\sin\theta + \frac{1}{a\cos\theta}\frac{\partial \Phi'}{\partial \lambda} = 0 \tag{4.1}$$

Meridional momentum:
$$\frac{\partial v'}{\partial t} + 2\Omega u'\sin\theta + \frac{1}{a}\frac{\partial \Phi'}{\partial \theta} = 0 \tag{4.2}$$

Energy:
$$\frac{\partial}{\partial t}\left(\frac{\partial \Phi'}{\partial z}\right) + N^2 w' = \frac{\kappa J}{H} \tag{4.3}$$

Continuity:
$$\frac{1}{a\cos\theta}\left[\frac{\partial u'}{\partial \lambda} + \frac{\partial}{\partial \theta}\left(v'\cos\theta\right)\right] + \frac{1}{\rho_0}\frac{\partial}{\partial z}\left(\rho_0 w'\right) = 0 \tag{4.4}$$

Where

u′: zonal wind perturbation

v′: meridional wind perturbation

w′: vertical wind perturbation

Φ': geopotential perturbation ($d\Phi = gdz$)

N^2: square of the Brunt-Vasialla (buoyancy) frequency

Ω: angular velocity of Earth's rotation

ρ_0: basic state density $\propto e^{-z/H}$

z: altitude

λ: longitude (radians)

θ: latitude (radians)

κ: $R/C_p \approx 2/7$

J: heating rate per unit mass (Joules/kg s)

a: radius of Earth (~6400 km)

g: gravity acceleration (~9.5 m/s^2 for middle and upper atmosphere region)

H: constant scale height ($k_B T/mg$)

t: time

Since tidal waves are large-scale waves and we have assumed that they are hydrostatically balanced, we hereafter assume the perturbations have the following longitudinally propagating wave form [Holton, 1975; Forbes, 1995]:

$$\{u, v, w, \Phi\} = \{\hat{u}, \hat{v}, \hat{w}, \hat{\Phi}\}\exp[i(s\lambda - \sigma t)] \tag{4.5}$$

where

s: zonal wavenumber (s = 0, 1, 2 ....)

σ: Frequency ($\sigma > 0$ eastward propagating waves)

($\sigma < 0$ westward propagating waves)

The zonal wave number, which gives the number of maxima of sinusoidal oscillation in longitude, is a positive integer (s = 0 corresponds to the zonally averaged flow). The sign of frequency σ in equation (4.5) is chosen such that waves with σ > 0 propagate to the east and waves with σ < 0 propagate to the west. By substituting the perturbation wave forms given by (4.5) into the linearized equations (4.1) – (4.4), we may eliminate the derivatives with respect to t and λ and obtain a single second-order partial differential equation for $\hat{\Phi}$ in z and θ. We further assume that the solution of this equation is saparable in the altitude and latitude with the form given by:

$$\hat{\Phi} = \sum_n \Theta_n(\theta) G_n(z) \tag{4.6}$$

where

$\{\Theta_n\}$ is a complete orthogonal set dependent on θ

$\{G_n(z)\}$ is a function dependent on z

The thermal excitation can also be expanded in the similar form to equation (4.6). By separating variables in this way, one obtains two equations, one is a D. E. (differential equation) in the horizontal variable θ, i.e., Laplace's tidal equation dependent on latitude; and the second is a D. E. in the vertical variable, altitude, z. The Laplace tidal equation is given by equation (4.7). It is usually written as the symbolic form in equation (4.8) to emphasize the explicit dependencies on s, σ, and ε_n.

$$\left\{\frac{d}{d\mu}\left[\frac{(1-\mu^2)}{(f^2-\mu^2)}\frac{d}{d\mu}\right]-\frac{1}{f^2-\mu^2}\left[-\frac{s}{f}\frac{(f^2+\mu^2)}{(f^2-\mu^2)}+\frac{s^2}{1-\mu^2}\right]\right\}\Theta_n = -\varepsilon_n\Theta_n \tag{4.7}$$

$$F_{s,\sigma}\left(\Theta_n^{s,\sigma}\right) = \varepsilon_n^{s,\sigma}\Theta_n^{s,\sigma} \tag{4.8}$$

where

$\mu = \sin\theta$

$\varepsilon_n = (2\Omega a)^2 / gh_n$ (h_n is the equivalent depth) (Eigenvalue)

Θ_n: Hough function (Eigenfunction)

$f = 2\Omega \sin\theta$ (Coriolis parameter)

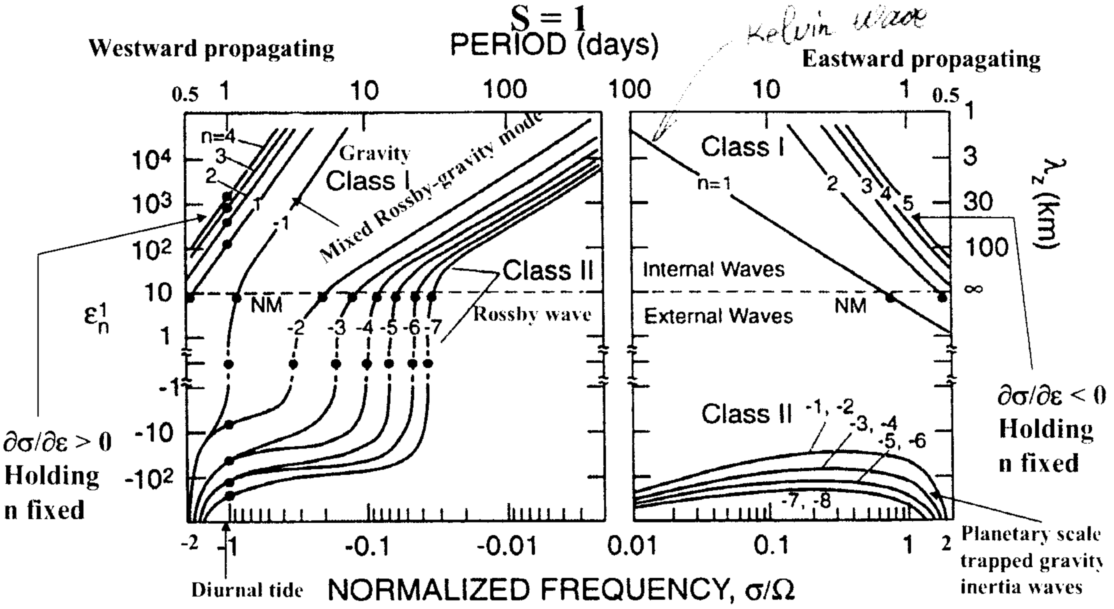

Figure 4.1 the plot of eigenvalue ε_n of wave modes of zonal wave number s = 1 vs. normalized frequency σ/Ω. Waves with positive (negative) frequencies propagate eastward (westward). Figure adapted from Volland [1988].

For each choice of s and σ, in fact there exist many sets of ε_n and Θ_n satisfying Laplace's equation. Since each eigenvalue/eigenfunction (ε_n and Θ_n) pair constitutes an eigenmode, we usually express a mode as Θ_n^s mode or just (s, n) mode (n is the meridional index). Shown in figure 4.1 is the diagram of eigenvalues ε_n of wave modes s = 1 vs. normalized frequency σ/Ω. We see the general features and properties from this figure. Class I refers to "gravity modes" with $\varepsilon_n > 0$, Class II refers to "Rossby" ("rotational"), or "planetary wave" modes with $\varepsilon_n > 0$ for westward propagating waves and $\varepsilon_n < 0$ for eastward propagating. At free (unforced) modes, $\varepsilon_n = 8.4$ (h_n = 10.5km) for an 256 K isothermal atmosphere. When s=1, these free modes have periods of 28 hours (1, -1), 5 days (1, -2), 8 days (1, -3), and 12 days (1, -4), and so on. Diurnal tides ($\sigma/\Omega = -1$, westward propagating wave) consist of a mixture of vertically trapped ((1, -1), (1, -2), ...) modes with negative n values and $\varepsilon_n < 0$, and vertically propagating ((1, 1), (1, 2), ...) modes. All class II waves disappear at frequency $|\sigma| > 2\Omega$, or for periods smaller than 12 hours.

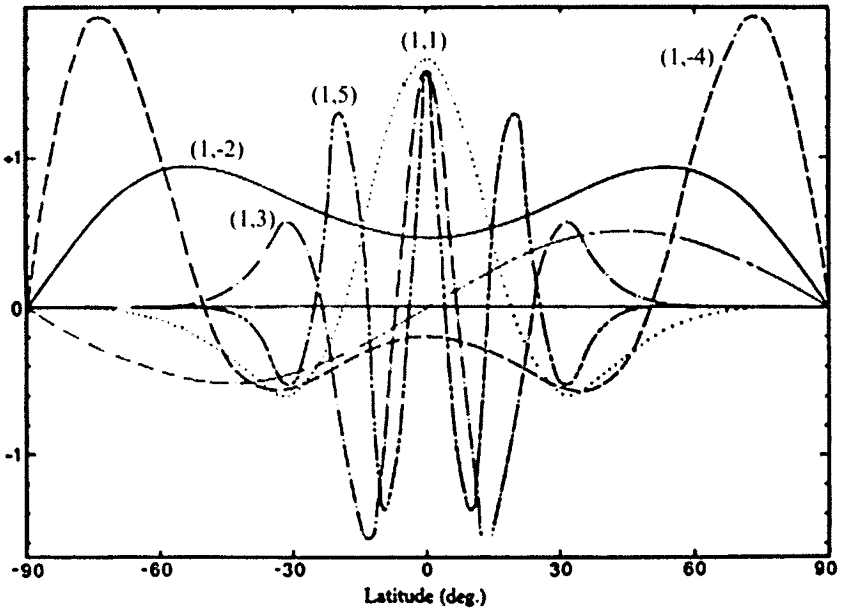

Figure 4.2 Symmetric Hough functions for migrating solar diurnal tides. (Adapted from Lindzen [1967])

Figure 4.2 illustrates the Hough functions for migrating solar diurnal tide. We can see that the vertically propagating modes (For example (1,3) mode only exists between 60N and 60S) disappear at the higher latitudes. Table 4.1 lists some of the more common westward propagating modes with approximate values of h_n and vertical wavelength λ_z in an isothermal atmosphere. In this nomenclature a mode is symmetric about the equator if n+s is even (odd) and antisymmetric if n+s is odd (even) for gravity (Rossby) solutions.

Table 4.1 Common westward propagating modes with approximate value of h_n and vertical wavelength λ_z in the isothermal atmosphere. [Forbes, 1995]

Wave	(s, n)	$(s, \lvert n\rvert - s)$	h_n (km)	λ_z (km)	Additional Descriptors
Diurnal tide	(1,1)		0.6909	27.9	Gravity; first symmetric propagating
Diurnal tide	(1,2)		0.2384	15.9	Gravity; first asymmetric propagating
Diurnal tide	(1,3)		0.1203	11.2	Gravity; second symmetric propagating
Diurnal tide	(1,-1)		803.356		Rotational; first asymmetric trapped
Diurnal tide	(1,-2)		-12.2703		Rotational; first symmetric trapped
Diurnal tide	(1,-4)		-1.7581		Rotational; second symmetric trapped
Semidiurnal tide	(2,2)		7.8519	311.	Gravity; first symmetric (propagating)
Semidiurnal tide	(2,3)		3.6665	81.4	Gravity; first asymmetric (propagating)
Semidiurnal tide	(2,4)		2.1098	53.8	Gravity; second symmetric (propagating)
Semidiurnal tide	(2,5)		1.3671	41.0	Gravity; second asymmetric (propagating)
Semidiurnal tide	(2,6)		0.9565	33.4	Gravity; third symmetric (propagating)
5-day wave	(1,-2)	(1,1)	10.5		Rotational; Rossby; first symmetric
10-day wave	(1,-3)	(1,2)	10.5	free	Rotational; Rossby; first asymmetric
16-day wave	(1,-4)	(1,3)	10.5	mode	Rotational; Rossby; second symmetric
4-day wave	(2,-3)	(2,1)	10.5		Rotational; Rossby; first symmetric
2-day wave	(3,-3)	(3,0)	10.5		Mixed Rossby-Gravity; asymmetric

The group velocity for atmospheric solar tides can be derived from the vertical structure equation. For vertical propagation ($0 < h_n < 4\kappa H$ and $\alpha^2 > 0$), the vertical group velocity should be positive and expressed as:

$$C_{gz*} \equiv \frac{\partial\sigma}{\partial\alpha} = 2\alpha\frac{\partial\sigma}{\partial\alpha}/\frac{\partial\alpha^2}{\partial\varepsilon} = \alpha\frac{8\Omega^2 a^2}{\kappa g H^2}\frac{\partial\sigma}{\partial\varepsilon} > 0 \qquad (4.9)$$

where

$$\alpha_n^2 = \frac{\kappa H}{h_n} - \frac{1}{4} = \frac{\kappa H g \varepsilon_n}{(2\Omega a)^2} - \frac{1}{4}$$

From figure 4.1, we can see that $\partial\sigma/\partial\varepsilon > 0$ for westward propagating waves and $\partial\sigma/\partial\varepsilon < 0$ for eastward propagating waves. Therefore, to maintain the "radiation condition" ($C_{gz*} > 0$), we must choose that $\alpha > 0$ for westward propagating waves and $\alpha < 0$ for eastward propagating waves. Now, let us assume the propagating modes have the form given by $e^{i(s\lambda + \alpha z^* - t\sigma)}$. The phase function $K = s\lambda + z^*\alpha - t\sigma$ defines the surfaces of constant phase. If λ (longitude) is fixed, then $z^* = t\sigma / \alpha + K$. For both westward ($\sigma < 0$, $\alpha > 0$) and eastward ($\sigma > 0$, $\alpha < 0$) propagating waves, phase propagates downward ($C_{pz^*} = \sigma/\alpha < 0$). If t (time) is fixed, then $z^* = -s\lambda / \alpha + K$, which implies that westward phase tilt ($-s/\alpha < 0$) for westward propagating waves ($\alpha > 0$) and eastward phase tilt ($-s/\alpha > 0$) for eastward propagating waves($\alpha < 0$).

For clarity in distinguishing migrating tides from non-migrating tides, we summarize:

Migrating tides: (subharmonics of a solar day)

- Zonal wavenumber s = 1, 2, 3,... and frequency $\sigma = -s\Omega$
    - migrating diurnal tide: $s = 1$, $\sigma = -\Omega$, $T = 24$hr
    - migrating semidiurnal tide: $s = 2$, $\sigma = -2\Omega$, $T = 12$hr
- Phase velocity for migrating tides: $C_p = -\Omega$
- (Westward propagating waves, do not move relative to the sun)
- Dominating driving sources: (periodic absorption of solar radiation throughout the atmosphere)
    - UV energy absorbed and re-radiated as heat by stratospheric ozone
    - IR energy absorbed by tropospheric water and water vapor

Non-migrating tides: (also subharmonics of a solar day)

- Zonal wavenumber ≠ their normalized frequency ($s \neq |\sigma/\Omega|$)
- (Can be stationary, or propagate either eastward or westward)
- Dominating driving sources for non-migrating tides:
    - The latent heat released by meteorological events in the troposphere

Our lidar has the capability to observe temperature, zonal wind, and meridional wind in the mesopause region simultaneously and continuously on a 24hr basis at one location. The dataset can be decomposed to diurnal mean and tidal components. All the tidal components obtained in this way include both migrating and non-migrating tides. Therefore, we can't separate migrating tides from non-migrating without additional information from a global dataset, e. g. satellite data or data from global chains of ground-base instruments.

4.2 Atmospheric planetary waves (Rossby waves)

The planetary or Rossby wave is one of the important large-scale meteorological flows in the middle atmosphere [Holton, 2000]. Relative vorticity of the flow is defined as the curl of the flow velocity, V, $\zeta = \nabla x V$. When air flows over topography/orography, the depth of the layer bounded within the two isentropic levels, D, changes, and the potential vorticity, defined as the absolute vorticity (defined below) divided by D, or $(f+\zeta)/D$, is conserved, when a parcel is moved adiabatically to a standard (reference) latitude in a frictionless flow. That the potential vorticity is conserved in adiabatic frictionless flow is analogous to conservation of angular momentum in solid mechanics.

Planetary waves conserve potential vorticity and owe their existence to meridional gradient of Coriolis parameter. The mechanism for generating planetary wave can be illustrated by considering the simple case of a homogeneous, incompressible fluid of uniform depth (referred to a barotropic non-divergent fluid), D. For such a fluid, the conservation of potential vorticity reduces to conservation of absolute vorticity, which is sum of the relative vorticity owing to the rotation of the fluid and the planetary vorticity owing to the rotation of the earth [Holton, 1992]. Suppose a closed chain of fluid parcels initially at rest in such a fluid and align along a circle of constant latitude θ. The absolute vorticity $\eta = f + \zeta$, where ζ is relative vorticity and $f = 2\Omega \sin\theta$ is planetary vorticity (local vertical component of planetary vorticity). Suppose at t_0, $\zeta = 0$, and at t_1, a fluid parcel is displaced slightly in the meridional direction from the original latitude by δy. Then the equation of the conservation of absolute vorticity is given by:

$$\zeta(t_1) + f(t_1) = f(t_0) \Rightarrow \zeta(t_1) = f(t_0) - f(t_1) = -\beta\delta y \tag{4.10}$$

where $f_{t_1} = f_{t_0} + \beta\delta y$ ($\beta \equiv df/dy$, and since f is independent of longitude, we term this as β plane approximation). If the chain of parcels is subject to a sinusoidal meridional displacement under absolute vorticity conservation, the resulting perturbation vorticity will be positive (negative) for southward (northward) displacement. Shown in figure 4.3 is the perturbation vorticity field and induced velocity field for a sinusoidal displacement of a chain of fluid parcels from its mean latitude. The pattern of the vorticity maxima and minima propagates to west. This westward propagating vorticity field constitutes a planetary wave. The meridional gradient of absolute vorticity resists the meridional displacement, and provides the restoring mechanism for planetary waves. The dispersion relation of free barotropic planetary waves on a β plane is easily derived by finding wave-type solutions of the linearized barotropic vorticity equation [Holton, 1992]. This dispersion relation is given by:

$$\omega = k\bar{u} - \frac{\beta k}{k^2 + l^2} \tag{4.11}$$

Where k = 2π/λ_x is zonal wavenumber, ℓ = 2π/λ_y is meridional wavenumber, and $\bar{u}$ is zonal mean wind. The intrinsic zonal phase speed is given by

$$C_{px} = \frac{\omega}{k} = \bar{u} - \frac{\beta}{k^2 + l^2} \Rightarrow \hat{C}_{px} \equiv C_{px} - \bar{u} = \frac{\beta}{k^2 + l^2} \tag{4.12}$$

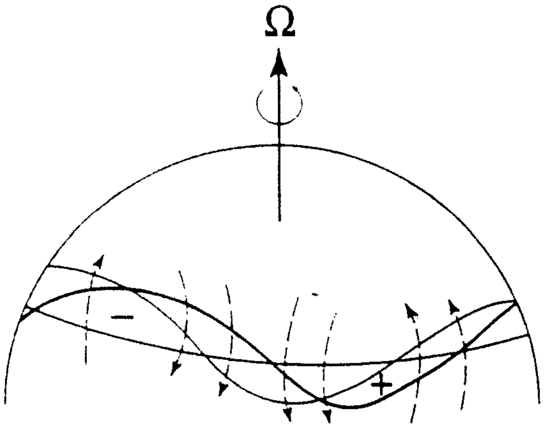

Figure 4.3 Perturbation vorticity field and induced velocity field (dashed arrows) for a sinusoidal displacement of a chain of fluid parcels from its mean latitude. Heavy wavy line denotes original perturbed position; light line denotes the westward displacement caused by advection of the pattern by the induced meridional velocity field. Positive sign means the induced vorticity points out of paper, visa versa. (Taken from Holton and Alexander [2000])

Planetary waves differ from other wave types, such as gravity waves, because the zonal phase propagation of gravity waves can be either eastward or westward, while the phase propagation of planetary waves is only westward relative to the mean wind. Furthermore, the zonal phase speed of the planetary waves increase rapidly with increasing wavelength (planetary waves are dispersive waves, so are gravity waves), Eq. 4.12. The free planetary waves are the normal modes of oscillations of the atmosphere, which generally have rather weak amplitudes [Holton, 1992]. However, another type of planetary wave which is also interesting for the MLT region study is the vertically propagating planetary waves, which are forced modes generated in the troposphere by flow over continental scale topography, by continent-ocean heating contrasts, and by nonlinear interactions among transient tropospheric wave disturbances [Holton, 2000]. These forced planetary waves are significantly different from that of the free planetary waves and are also important for understanding the planetary-scale circulation pattern. Linear wave theory shows that for a stationary planetary wave (stationary relative to the ground), the vertical wavenumber m ($m=2\pi/\lambda_z$, where λ_z is vertical wavelength) is given by the relation [Andrews et al., 1987]:

$$m^2 = \frac{N^2}{f^2}\left[\frac{\beta}{\bar{u}} - \left(k^2 + l^2\right)\right] - \frac{1}{4H^2} \qquad (4.13)$$

For topographically generated planetary waves, $m^2 > 0$ only if

$$0 < \bar{u} < u_c \qquad where \quad u_c = \beta\left(k^2 + l^2 + \frac{f^2}{4N^2H^2}\right) \qquad (4.14)$$

where u_c is the zonal wind value for which $m = 0$. Planetary waves can propagate upward for $m^2 > 0$, while the waves are trapped for $m^2 < 0$. Therefore, for a stationary planetary wave, vertical propagation can only exist in the presence of mean westerly winds that are less than u_c. When the phase speed of planetary wave becomes comparable to background mean wind, the effects of mean wind assume much greater importance. For example for a 2-day wave at 40N latitude, the horizontal phase speed is ~30m/s. In this case, and for other planetary waves as well, the summer easterlies (westward) of order -20 to -60m/s could obviously have dramatic effects on the propagation of planetary waves [Forbes, 1995]. The critical level is the altitude where the horizontal phase speed of a planetary wave is equal to the horizontal background mean wind. The planetary wave is more sensitive to dissipative processes when it approaches the critical level than gravity wave.

4.3 Atmospheric gravity waves

Atmospheric gravity waves are propagating waves associated with excess gravity (over buoyancy) as restoring force in stably stratified fluids [Holton, 2000]. The dominant sources of gravity waves include topography, convection, and wind shear, although other sources may also be significant, such as wave-wave interactions and body force accompanying localized wave dissipation [Fritts and Alexander, 2003]. Because of their major roles in transporting energy and momentum, in contributing turbulence and mixing, and in influencing the mean circulation and thermal structure of the middle atmosphere, gravity waves have been a subject of continued research activity for more than four decades since the pioneering study by Hines [1960]. In this section, following the review paper "Gravity wave dynamics and effects in the middle atmosphere" by Fritts and Alexander [2003] we will briefly review the linear theory of gravity waves, and discuss some simple forms of the dispersion relations. The method of the hodograph analysis of inertia-gravity waves will also be discussed.

4.3.1 Linear theory of gravity waves

Atmospheric gravity waves are usually described by a simple linear theory that treats them as small perturbation on a stably stratified background state varying only in the vertical [Fritts and Alexander, 2003]. The conservation of momentum, mass, and energy [Holton, 1992], give the equations of fundamental fluid motion in Cartesian coordinates (x, y, z) with velocity components (u,v,w) which is different from the coordinates we used in tidal equations. The pressure is p and the mass density is ρ.

(1) Momentum Equation

Zonal: $$\frac{Du}{Dt} - fv + \frac{1}{\rho}\frac{\partial p}{\partial x} = F_x \tag{4.20}$$

Meridional: $$\frac{Dv}{Dt} + fu + \frac{1}{\rho}\frac{\partial p}{\partial y} = F_y \tag{4.21}$$

Vertical: $$\frac{Dw}{Dt} + \frac{1}{\rho}\frac{\partial p}{\partial z} + g = 0 \tag{4.22}$$

(2) Continuity equation

$$\frac{1}{\rho}\frac{\partial \rho}{\partial t} + \frac{\partial u}{\partial x} + \frac{\partial v}{\partial y} + \frac{\partial w}{\partial z} = 0 \tag{4.23}$$

(3) Energy Equation

$$\frac{D\theta}{Dt} = Q \tag{4.24}$$

where θ is the potential temperature

$$\theta = T\left(\frac{p}{p_0}\right)^{-R/C_p} = \frac{p}{\rho R}\left(\frac{p_0}{p}\right)^{R/C_p} = \frac{p}{\rho R}\left(\frac{p_0}{p}\right)^{\kappa}$$

$$\kappa = R/C_p \approx 2/7$$

D/Dt is the total or material derivative (time derivative of the fluid following the motion)

$$\frac{D}{Dt} = \frac{\partial}{\partial t} + u\frac{\partial}{\partial x} + v\frac{\partial}{\partial y} + w\frac{\partial}{\partial z}$$

Suppose all the linearized equations are unforced in the horizontally uniform hydrostatic basic state with background wind ($\bar{u}(z), \bar{v}(z)$, 0), potential temperature $\bar{\theta}(z)$, pressure $\bar{p}(z)$, and density $\bar{\rho}(z)$. Any variable will then be the sum of the perturbation (prime term) and background (bar term). According to the WKB approximation [Gill, 1982], we neglect the background shears in the above equations and assume that $(\bar{u}(z), \bar{v}(z))$ and buoyancy frequency vary very slowly over a wave cycle in the vertical direction. To describe a monochromatic wave perturbation with wave number (k, l, m) and ground observed frequency ω, we also assume that the gravity wave solutions have the wave form given by:

$$\left(u', v', w', \frac{\theta'}{\bar{\theta}}, \frac{p'}{\bar{p}}, \frac{\rho'}{\bar{\rho}}\right) = \left(\hat{u}, \hat{v}, \hat{w}, \hat{\theta}, \hat{p}, \hat{\rho}\right)\exp\{i(kx + ly + mz - \omega t) + z/(2H)\} \qquad (4.25)$$

By substituting the equation above into the general equations (4.20) – (4.24), we obtain a set of another six equations for wave amplitudes of winds, potential temperature, pressure, and density. We are not going to present detailed derivations for all these equations which could be found in the review paper by Fritts and Alexander [2003]. Combining all the equations above, we can derive the gravity wave dispersion relation expressed by:

$$\hat{\omega}^2 = \frac{N^2(k^2 + l^2) + f^2(m^2 + 1/4H^2)}{k^2 + l^2 + m^2 + 1/4H^2} \Rightarrow m^2 = \frac{(k^2 + l^2)(N^2 - \hat{\omega}^2)}{(\hat{\omega}^2 - f^2)} - \frac{1}{4H^2} \qquad (4.26)$$

where $\hat{\omega} = \omega - k\bar{u} - l\bar{v}$ is the intrinsic frequency which is the frequency observed in a frame of reference moving with the background wind ($\bar{u}(z), \bar{v}(z)$, 0). The wave frequency, the wave numbers, and the properties of the background atmosphere are all related through this dispersion relation.

The group velocity of the gravity wave describing energy transportation and wave packet propagation can also be obtained from the dispersion relation and written as:

$$\left(c_{gx}, c_{gy}, c_{gz}\right) = \left(\frac{\partial \omega}{\partial k}, \frac{\partial \omega}{\partial l}, \frac{\partial \omega}{\partial m}\right) = \left(\overline{u}, \overline{v}, 0\right) + \frac{\left\{k\left(N^2 - \hat{\omega}^2\right), l\left(N^2 - \hat{\omega}^2\right), -m\left(\hat{\omega}^2 - f^2\right)\right\}}{\hat{\omega}\left(k^2 + l^2 + m^2 + 1/4H^2\right)} \quad (4.27)$$

where N^2 is square of the buoyancy frequency. The sign convention assumes that $\hat{\omega}$ is always positive. The (k, l) vector defines the direction of horizontal propagation (k > 0 for eastward and l > 0 for northward). From the equation above we can clearly see that the horizontal intrinsic group velocity has the same direction as the horizontal intrinsic phase speed ($\hat{c}_x = \hat{\omega}/k, \hat{c}_y = \hat{\omega}/l$). However, the direction of the vertical phase speed ($\hat{c}_z = \hat{\omega}/m$) is opposite to that of vertical group velocity. Therefore, although the direction of wave propagation is given by vector (k, l, m), the speeds of line of constant phase along coordinate directions are not equal to the components of wave's phase velocity, which is parallel to the wave vector. However the group velocity is a (real) vector [Cushman-Roisin, 1994].

In addition, the polarization relations are obtained relating the perturbation amplitudes of the different variables associated with the same wave from a set of equations. Some of them are listed below, and others could be found in the review paper by Fritts and Alexander [2003].

$$\hat{u} = \left(\frac{ik\hat{\omega} - lf}{il\hat{\omega} + kf}\right)\hat{v} \tag{4.28}$$

$$\hat{T} = \frac{H(im + 1/2H)(\hat{\omega}^2 - f^2)}{\hat{\omega} kR\hat{u}} \tag{4.29}$$

Since the frequency of gravity wave must be higher than the inertial frequency f (T_{inertial} = 18.4 hr in Fort Collins, CO), we distinguish three different wave groups, sorted by frequency: high frequency waves ($\hat{\omega} >> f$), medium-frequency waves ($N >> \hat{\omega} >> f$), and low-frequency waves ($\hat{\omega} \sim f$).

For high frequency gravity waves (internal gravity waves, $\hat{\omega} >> f$), we neglect the Coriolis force and assume that $m^2 >> 1/4H^2$. The gravity wave dispersion relation of gravity wave simplifies to:

$$\hat{\omega}^2 = \frac{N^2(k^2 + l^2)}{k^2 + l^2 + m^2} = N^2 \cos^2 \alpha \tag{4.30}$$

where, assuming plane waves, α is the angle between phase fronts and vertical axis. At the same time, the group velocity is also simplified to:

$$(c_{gh}, c_{gz}) = (\bar{u}_h, 0) + \frac{Nm}{k_h^2 + m^2} \frac{(m, -k_h)}{(k_h^2 + m^2)^{1/2}} \tag{4.31}$$

where c_{gh} is the horizontal group velocity, $\bar{u}_h$ is the horizontal wind velocity in the direction of gravity wave propagation, and $k_h = \sqrt{k^2 + l^2}$ is the horizontal wave number. We see from this equation not only that for upward group velocity, the phase propagates downward, but also that the group velocity is parallel to the lines of constant phase and perpendicular to direction of phase propagation.

For medium-frequency waves ($N >> \hat{\omega} >> f$), the dispersion relation has very simple format given by equation (4.32). By slightly changing the format of the equation, we can simply relate the vertical wave number to the background wind and buoyancy frequency N.

$$\hat{\omega} = N\left|\frac{k_h}{m}\right| \Rightarrow |m| = \frac{N}{|\hat{c}_h|} \tag{4.32}$$

where $\hat{c}_h = (c_h - \overline{u}_h)$ is the intrinsic horizontal phase speed, and $k_h > 0$ for $\hat{c}_h > 0$ and $k_h < 0$ for $\hat{c}_h < 0$. This equation shows that both the vertical wave length and intrinsic frequency are proportional to the intrinsic horizontal phase speed. If there is a critical level where $c_h = \overline{u}_h \Rightarrow \hat{c}_h = 0$, the vertical wavelength of the wave shrinks to zero at that level. The instability and dissipation mechanisms become more likely as a wave approaches a critical level because its vertical wavelength decreases to zero, and temperature gradient and wind shear become very large. As the critical level is approached, the vertical group velocity of a wavepacket slows down, thus the packet will never reach the critical level in the real atmosphere. The group velocity for medium frequency waves will be given by:

$$(c_{gh}, c_{gz}) = (\overline{u}_h, 0) + \left(\frac{\hat{\omega}}{k_h}, -\frac{\hat{\omega}}{m}\right) \tag{4.33}$$

We can see that the vertical group velocity has the same magnitude as the vertical phase speed but opposite sign. The equation also shows that to reach a critical level (m→∞), a wave packet requires an infinite time, implying that time-dependent and nonlinear effects become important when the wave approaches a critical level.

For low-frequency waves (inertia-gravity waves, $\hat{\omega} \sim f$), the effect of the earth rotation (Coriolis parameter f) becomes important. For a propagating wave in the zonal direction, the meridional velocity amplitude $\hat{v}$ is simply expressed as:

$$\hat{v} = -i\frac{f}{\hat{\omega}}\hat{u} \tag{4.34}$$

Later, we will use this equation and polarization relation of temperature amplitude and zonal wind amplitude to do hodograph analysis.

The dispersion relation for the low-frequency waves is given by:

$$\hat{\omega}^2 = N^2\frac{k_h{}^2}{m^2} + f^2 \tag{4.35}$$

When any wave approaches a critical level where the background wind speed is close to horizontal phase speed ($c_h = \bar{u}_h$ and m→∞), the wave frequency will move toward lower intrinsic frequency, then the rotation effects become more important. The vertical and horizontal group velocities could be both derived from dispersion relation, and the ratio of them is:

$$\left|\frac{c_{gz}}{c_{gh}}\right| = \left|\frac{k_h}{m}\right| = \frac{\left(\hat{\omega}^2 - f^2\right)^{1/2}}{N} \tag{4.36}$$

This ratio becomes very small for inertia-gravity waves relative to their high-frequency counterparts. And they also could be found at large horizontal distance from their sources [Dunkerton, 1984; Eckermann, 1992]

4.3.2 Hodograph Analysis of inertia-gravity waves

For a single, steady, non-dissipating, propagating inertia-gravity wave, Eq. (4.34) suggests that the polarization ellipses of horizontal velocity of the intertia-gravity wave can be used to determine the intrinsic frequency of the wave [Eckermann, 1996]. The horizontal propagation direction of the wave is oriented parallel to the ellipse's major axis [Vincent et al., 1987], while the sense of ellipse rotation with height provides the direction of the wave's vertical group velocity [Andrews et al., 1987; Hirota et al., 1985]. The most widely used method is to form hodographs from the velocity profiles, which is a straightforward technique, very accurate when a large-amplitude monochromatic inertia-gravity wave is present [Cot et al., 1986]. According to the polarization relation in equation (4.28), the amplitude of quadrature-phase wind $\hat{v}$ (v' is perpendicular to the horizontal wave propagation direction) is 90° out of phase with the amplitude of in-phase wind $\hat{u}$ (u' is along the horizontal wave propagation direction). In northern hemisphere where $f > 0$ (f is the Coriolis parameter, or inertial frequency), $\hat{v}$ will lead $\hat{u}$ for upward propagating waves. In the other word, the (u', v') vector will rotate clockwise with the increasing altitudes for upward propagating waves. At the same time, from equation (4.29), for upward propagating waves ($m < 0$), $\hat{T}$ will lead $\hat{u}$ for waves propagating in positive in-phase direction ($0° \leq$ azimuth angle $< 180°$) and the (u', T') vector will rotate clockwise with increasing altitude. These rotations are reversed for waves propagating in the opposite direction [Hu et al., 2002]. Therefore, by using the hodograph method, we can determine both the horizontal and vertical propagation directions of both group and phase velocities, as well as the intrinsic frequency of the inertia-gravity wave. Hodograph analysis of inertial gravity wave will be discussed in section 5.2 and 5.4.

4.4 Gravity wave–Tidal–planetary wave interactions

As discussed in section 4.3, gravity waves play a central role in controlling the mean circulation and thermal structure through wave momentum transport, wave filtering, and the body forces arising from wave dissipation and momentum flux divergence. Such filtering and effects are mostly due to mean wind shears as well as larger-scale tides and planetary waves. Walterscheid [1981] addressed the feedbacks on tidal structure through selective gravity wave filtering near critical levels. Holton [1984] pointed out that the planetary waves could be excited at the altitudes where gravity wave body forcing is asymmetric. Recent model studies [Forbes, 1991; Lu and Fritts, 1993; Mayr et al., 1998; Meyer, 1999b; McLandress and Ward, 1994; Norton and Thuburn, 1997] shows that the interaction could potentially influence the tidal and planetary wave structures and their variability. The coupling between gravity waves and the larger-scale motions accounting for wave filtering is very complicated. If gravity waves are dissipated near or below a large-scale wave maximum in the direction of gravity wave propagation, then the result is that wave maximum is accelerated and induces a downward phase motion. If gravity waves are dissipated by breaking where the large-scale wave moves in the opposite direction, then gravity forcing will reduce the amplitude of the large-scale wave.

Recent observations by our sodium lidar system and other ground-base instruments (e.g. radars) show that the atmospheric tides manifest a significant day-to-day variability. It has been suggested that this short-term variability may be the result of several mechanisms [Vial, 1992], primarily the interactions between tides and planetary waves, and/or tides and gravity waves [Fritts et al., 1987]. Manson [1982] first noted that the regular variation in tidal amplitude has periods similar to those of planetary waves, and that secondary waves which are generated with frequencies that are the sum or difference of primary tides and planetary waves were also observed. Teitelbaum and Vial [1991] and Ruster [1994] suggested that the nonlinear interactions between tides and planetary waves are an important cause for the short-term tidal variability. Fritts and Vincent [1987] found a high correlation of large tidal amplitude and shears with gravity wave momentum flux, suggesting that the tidal/gravity wave interactions accounts for their observations of varied momentum flux. Modeling studies also reveal the important role of tidal/gravity wave interactions in affecting the short-term tidal variability [Liu et al., 1998; Liu 2000]. Therefore, the observed short-term tidal variability could have contributions from both tidal/planetary interactions and tidal/gravity wave interactions. In chapter 5, we will show the tidal day-to-day variability observed by our lidar system near equinox, summer season, and winter season, revealing varied form of tide-gravity wave interactions and planetary wave modulation of tides.

Reference:

Andrews, D. G., J. R. Holton, and C. B. Leovy, *Middle Atmosphere Dynamics*, Academic Press, 489pp, 1987.

Cot, C. E., and J. Barat, Wave-turbulence interaction in the stratosphere: A case study, *J. Geophys. Res.*, 91, 2749–2756, 1986.

Chapman, S. and R. S. Lindzen, Atmospheric Tides, Reidel, Norwell, Mass., 1970.

Dunkerton, T. J., Inertia-gravity waves in the stratosphere, *J. Atmos. Sci.*, 41, 3396–3404, 1984.

Eckermann, S. D., Ray-tracing simulation of the global propagation of inertia gravity waves through the zonally averaged middle atmosphere, *J. Geophys. Res.*, 97, 15,849–15,866, 1992.

Eckermann, S. D., Hodographic analysis of gravity waves: Relationships among Stokes parameters, rotary spectra and cross-spectral methods, *J. Geophys. Res.*, 101, 19,169-19,174, 1996.

Killeen, T.L. and R.M. Johnson, Upper atmospheric waves, turbulence, and winds: Importance for mesospheric and thermospheric studies, *Rev. Geophys.*, 33: 737-743 Part 1 Suppl. S, 1995.

Fobers, J. M., Tidal and Planetary Waves. The Upper Mesosphere and Lower Thermosphere: A Review of Experiment and Theory, *Geophy. Monog. Ser.*, vol. 87, p67-87, 1995.

Forbes, J. M., M. E. Hagan, X. Zhang, and K. Hamilton, Upper atmospheric tidal oscillations due to latent heat release in the tropical troposphere, *Ann. Geophys., 15*, 1165-1175, 1997.

Fritts, D. C., and T. E. VanZandt, Effects of Doppler shifting on the frequency spectra of atmospheric gravity waves, *J. Geophys. Res.*, 92, 9723–9732, 1987.

Fritts, D. C., and R. A. Vincent, Mesospheric momentum flux studies at Adelaide, Australia: Observations and a gravity wave/tidal interaction model, *J. Atmos. Sci.*, 44, 605–619, 1987.

Fritts, D. C., and M. J. Alexander, Gravity wave dynamics and effects in the middle atmosphere, *Rev. Geophys.*, 41(1), 1003,doi:10.1029/2001RG000106, 2003.

Gill, A. E., *Atmosphere-Ocean Dynamics*, 662 pp., Academic, San Diego, Calif., 1982.

Hagan, M. E., J. L. Chang, and S. K. Avery, GSWM estimates of non-migrating tidal effects, *J. Geophys. Res., 102,*, 16,439-16,452, 1997.

Hagan, M. E., M. D. Burrage, J. M. Forbes, J. Hackney, W. J. Randel, and X. Zhang, GSWM-98: Results for migrating solar tides, *J. Geophys. Res. ,104*, 6813-6828, 1999.

Hagan, M. E. and J. M. Forbes, Migrating and nonmigrating diurnal tides in the middle and upper atmosphere excited by tropospheric latent heat release, *J. Geophys. Res., 107*(D24), 4754, doi: 10.1029/2001JD001236, 2002.

Hagan, M. E. and J. M. Forbes, Migrating and nonmigrating semidiurnal tides in the upper atmosphere excited by tropospheric latent heat release, *J. Geophys. Res., 108*(A2), 1062, doi:10.1029/2002JA009466, 2003.

Hines, C. O., Internal atmospheric gravity waves at ionospheric heights, *Can. J. Phys.*, 38, 1441–1481, 1960.

Hirota, I., and T. Niki, A statistical study of inertia-gravity waves in the middle atmosphere, *J. Meteorol. Soc. Jpn.*, 63, 1055–1066, 1985.

Holton, J. R., The Dynamic Meteorology of the Stratosphere and Mesosphere, *Meteor. Monog. Ser.*, 15(37), Amer. Met. Soc., MA, 1975.

Holton, J. R., The generation of mesospheric planetary waves by zonally asymmetric gravity wave breaking, *J. Atmos. Sci.*, 41, 3427–3430, 1984.

Holton, J. R., *An Introduction to Dynamic Meteorology*, Academic Press, Orlando, 511pp., 1992.

Holton, J. R., and M. J. Alexander, The role of waves in the transport circulation of the middle atmosphere, in *Atmospheric Science Across the Stratopause, Geophys. Monogr. Ser.*, vol. 123, edited by D. E. Siskind, S. D. Eckermann, and M. E. Summers, pp. 21–35, AGU, Washington, D. C., 2000.

Hu, X., A. Z. Liu, C. S. Gardner, and G. R. Swenson, Characteristics of quasi-monochromatic gravity waves observed with Na lidar in the mesopause region at Starfire Optical Range, NM, *Geophys. Res. Lett.*, *29*(24), 2169, doi:10.1029/2002GL014975, 2002.

Lindzen, R. S., Thermally driven diurnal tide in atmospherie, *Quart. J. Roy. Meteoro. Soc.*, 93 (395), 18, 1967.

Liu, H., and M. E. Hagan, Local heating/cooling of the mesosphere due to gravity wave and tidal coupling, *Geophys. Res. Lett.*, 25(15), 2941–2944, 1998.

Liu, H., Temperature changes due to gravity wave saturation, *J. Geophys. Res.*, 105(D10), 12,329-12,336, 2000.

Manson, A. H., Meek, C. E., Gregory, J. B., and Chacrabarty, D. K., Fluctuation in tidal (24- and 12-h) characteristics and oscillations (8-h and 5-h) in the mesosphere and lower thermosphere (70-110km): Saskatoon (52N, 107W), 1979-1981, *Planet. Spac. Sci.*, 30, 1283-1294, 1982.

Pancheva, D. et al., Global-scale tidal structure in the mesosphere and lower thermosphere during PSMOS campaign of June-August 1999 and comparison with the global-scale wave model, J. Atmo. Solar-Terr. Phys. 64, 1011-1035, 2002.

Cushman-Roisin, Benoit, *Introduction to Geophysical Fluid Dynamics*, Prentice-Hall, 1994

Ruster, R., VHF radar observations of nonlinear interactions in the summer polar mesosphere, *J. Atmos. Terr. Phys.*, 56, 1289-1299, 1994.

She, C. Y., T. Li, B. P. Williams, T. Yuan, and R. H. Picard, Concurrent OH imager and sodium temperature/wind lidar observation of a mesopause region undular bore event over Fort Collins/Platteville, Colorado, *J. Geophys. Res.*, 109, D22107, doi:10.1029/2004JD004742, 2004.

Teitelbaum, H., and Vial, F., On tidal variability induced by nonlinear interaction with planetary waves, *J. Geophys. Res.*, 96, 14,179-14,182, 1991.

Vial, F., Causes of tidal variability, *Coupling processes in the lower and middle atmosphere*, edited by Thrane, E. V., Blix, T. A., Fritts, D. C., Kluwer Academic, 1992.

Vincent, R. A., and D. C. Fritts, A climatology of gravity waves in the mesosphere and lower thermosphere over Adelaide, Australia, *J. Atmos. Sci.*, 44, 748–760, 1987.

Volland, H., *Atmospheric Tidal and Planetary Waves*, Kluwer Academic Publ., Boston, MA, 1988

Walterscheid, R. L., Inertio-gravity wave induced accelerations of mean flow having an imposed periodic component: Implications for tidal observations in the meteor region, *J. Geophys. Res.*, 86, 9698–9706, 1981.

Chapter 5: Variability in mesopause region temperature and horizontal wind

In the MLT region (Mesosphere and Lower Thermosphere), the dynamic variability dominates the atmospheric observations, mainly due to the presence of ubiquitous and varied gravity waves and planetary waves, as well as their interactions with mean wind and tides. Currently, these topics are still under intense modeling studies with observations with sufficient resolution providing reality check lagging behind. With the newly achieved robustness in lidar simultaneous observations of mesopause region temperature and horizontal wind over a period of several days, data acquired indeed contain interesting and unexpected examples of tidal variability.

To demonstrate the power of multiple-day continuous and simultaneous observations of temperature, zonal and meridional winds by CSU sodium lidar system, we will present three different events covering three different seasons (summer, fall, and winter) in this chapter. We will first discuss the data analysis method for temperature and wind tides in section 5.1, and then present the tidal day-to-day variability in our longest dataset in Sep. 2003 as well as the possible tidal/planetary wave and/or tidal/gravity wave interactions in section 5.2. Section 5.3 discusses quasi-two-day waves observed by lidar in August 2002, 2003, 2004 as well as tidal day-to-day variability in these datasets, and compares the quasi-two-day waves observed by lidar and TIMED/SABER satellite. Finally, the winter temperature inversion layer and its relation with tidal variability will be discussed in section 5.4.

5.1 Data Analysis for the temperature and wind tides

As discussed in section 3.4, the temperature, radial winds, and sodium density are calculated separately for daytime and nighttime. For a multiple-day campaign, many files will be produced with different filenames depending on UT day number, beam number, daytime or nighttime, temporal and spatial resolution and data types. In order to do tidal fitting, we collect the same types of files, such as temperature files for specified resolution together according to their time sequences into a text file format, called "masstd" file, for historical reason. Then the masstd file is read by tidal analysis programs in order to do tidal fitting altitude by altitude.

5.1.1 Generation of masstd files

Since we are doing two-beam measurements with one east beam and one north beam, both pointing 30° from zenith, the initial analysis will only give the temperature and line-of-sight (LOS) wind for each beam. In order to derive the values of zonal wind and meridional wind, we assume that for a time interval in question, the vertical wind velocity is averaged to zero. We then obtain zonal wind and meridional wind from LOS winds using a simple equation, $V_{Zon,Mer} = V_{LOS}/\sin 30° = 2V_{LOS}$. This step is done when we generate the zonal wind masstd file and meridional wind masstd file from the initial LOS wind files. Strictly speaking, the assumption of zero vertical wind is valid only when gravity wave perturbations are averaged to zero. Since the wind bias due to short period vertical wind perturbations in the temporal resolution in question is much smaller than the horizontal wind speed, this working hypothesis is considered to be valid.

Like raw photon files, the vertical separation is usually about 130 m in the analyzed temperature and LOS wind files, with 150 m range bin (distance) separation for the beams tilted 30° from zenith. Since vertical smoothing is done for the raw photon profile in the initial analysis, the typical vertical resolution is taken to be 2-km for 31-point smoothing (nighttime) and 4-km for 61-point smoothing (daytime). In the masstd file, we over-sample and read the values at altitudes with separation of 0.5 km, such as 90.0 km, 90.5 km,…., and leave other points out.

Masstd files of temperature and sodium density are generated from each of two beams. Therefore we have two temperature masstd files and two sodium density masstd files. Since the separation distance of two beams in the mesopause region is ~70km, unless otherwise specified, we report temperatures by averaging over the two observed temperatures weighted by their error bars due to photon noise.

5.1.2 Tidal fitting

In order to extract the tidal information from our 24hr continuous dataset over a single lidar station, we can decompose the field variables, such as temperature T, zonal wind U, and meridional wind V as a function of altitude and time, to a diurnal mean, a sum of four leading tidal components or tidal-period oscillations (amplitudes and phases for 24hr, 12hr, 8hr, and 6hr periods), and a residual term. It can be expressed as [She, 2004]:

$$\Phi^{T,U,V}(z,t)=\overline{\Phi^{T,U,V}}(z)+\sum_{j=1,\dots 4}A_j^{T,U,V}(z)\cos\left\{\frac{2\pi j}{24}\left[t-\tau_j(z)\right]\right\}+R^{T,U,V}(z,t) \qquad (5.1)$$

Where

$\overline{\Phi^{T,U,V}}$: Diurnal mean

$A_j^{T,U,V}$:Amplitude

$\tau_j(z)$: Phase (crest in local hours)

$R^{T,U,V}(z,t)$: Residual

If there is a lidar dataset covering over a full diurnal cycle (24hr) without data gap and each dynamic field (T, U, V) is expressed as a sum of quadrature terms, the diurnal mean, tidal amplitudes, and phases could be determined un-ambiguously by using linear least-square fit. The difference between the raw data and their least-square fitted function will give the residual term, $R^{T,U,V}(z,t)$, which includes the information of all other perturbations, such as gravity waves. Since the expansion of the field variables into equation 5.1 is unique within the uncertainty limit of the observation, the diurnal mean, tidal amplitudes, and phases can be determined solely from observational data. It should be noted, however, that for fits to data sets that are not multiples of 24 hours and/or that have missing hours the amplitudes and phases are not independent.

For a multiple-day continuous campaign, we can do linear least-square fits of the whole dataset, yielding the best-fit vertical profiles of amplitudes and phases of tidal components (diurnal, semidiurnal, terdiurnal, and quaddiurnal). Tidal amplitudes and phases obtained in this way will be referred hereafter as mean tidal values. On the other hand, if this continuous campaign is long enough for the study of day-to-day variability of tidal perturbations (usually more than 3 days), we can also perform tidal best fits within a running 24hr window centered at every hour on the dataset to obtain the time series of vertical profiles of diurnal-means, tidal amplitudes and phases. In this manner, we can investigate the day-to-day variability of tides and mean fields. In this thesis, we concentrate on the diurnal-mean, diurnal and semidiurnal tidal components.

5.2 Tidal day-to-day variability near Fall equinox

During the second half of Sep 2003, fair weather prevailed in northern Colorado, and an unusually long data set of 14-day duration was acquired between Sep 18 and Oct 01 including a 9-day observation which was continuous except for a 4 hour gap at the end of day 269. The length of this lidar observation exceeds that of other middle atmosphere lidar observations to-date, and is similar to that of radar campaigns [Thayaparan et al., 1995]. Multi-day observations of this type allow studies where the shorter-period planetary waves (PW) and gravity waves (GW) can be averaged out and the analysis can focus on the recurrent tidal wind and temperature perturbations. Since the data set is long enough, we could conduct a tidal day-to-day variability study, and examine planetary wave and gravity wave perturbations as well as their nonlinear interactions with tidal waves. Shown in upper, middle, lower panels of figure 5.1 are the contour plots of temperature, zonal wind, and meridional wind with the vertical resolution of 2 km and the

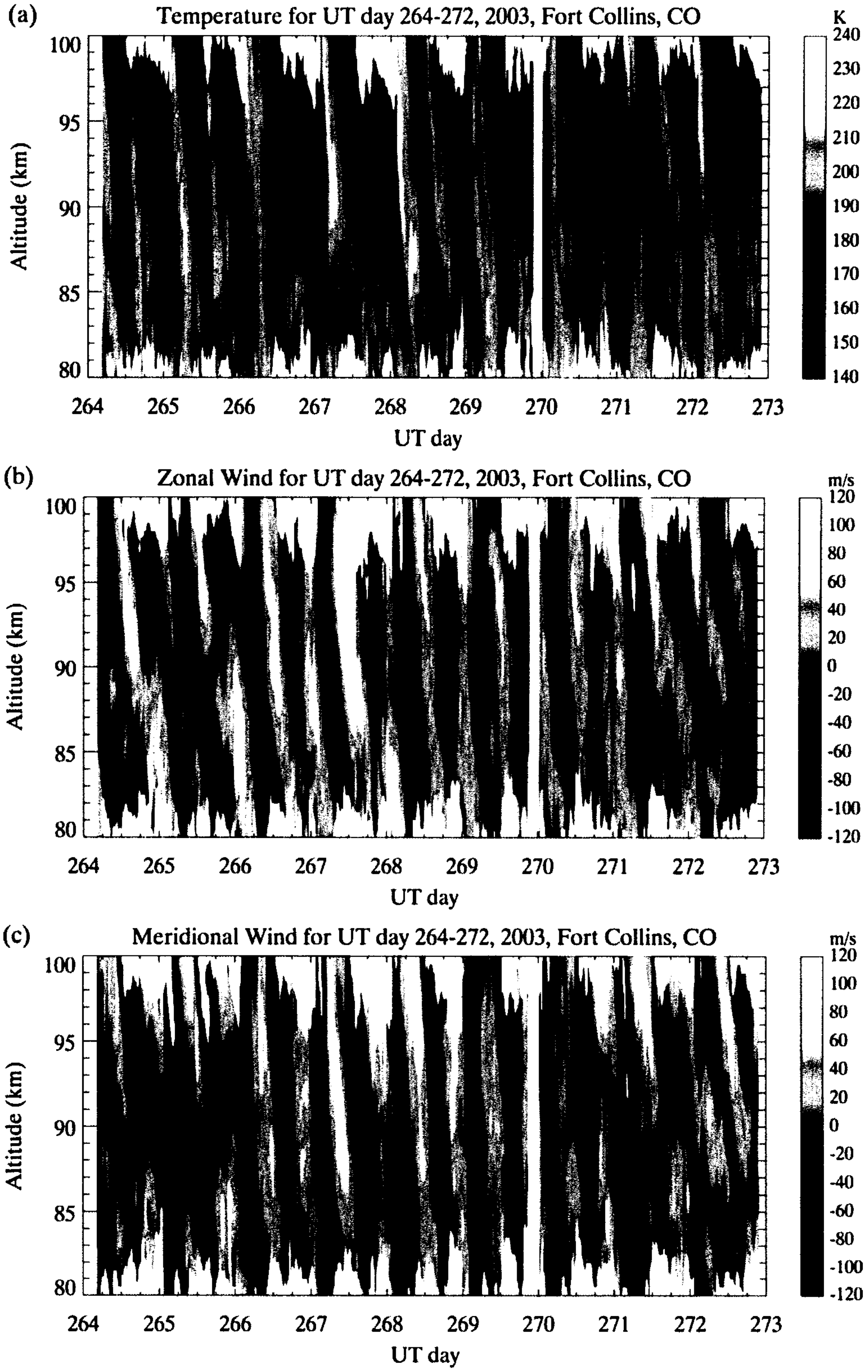

Figure 5.1 Contour plots of temperature (a), zonal wind (b), and meridional wind (c) observed by CSU sodium lidar between UT day 264 and UT day 272 of 2003. Diurnal and semidiurnal oscillations are clearly shown in all three fields with downward phase progression. Day-to-day variability of tides can also be clearly seen with tidal enhancement on UT day 267 and 268.

temporal resolutions of 15 minutes for nighttime and 30 minutes for daytime. The ranges of temperature, zonal wind, and meridional wind are seen to be approximately between (150K, 220K), (-120m/s, 120m/s), and (-120m/s, 120m/s), respectively. With a quick inspection, these contours clearly show diurnal and semidiurnal oscillations with downward phase progression. We could also see the dramatic day-to-day variation, especially on UT day 267 and 268 with large enhancement in temperatures and winds. In addition to tidal period perturbations, short period perturbations, presumably due to gravity waves are also suggested in all three contours.

5.2.1 Mean tidal field

According to equation 5.1, a harmonic analysis of the continuous 9-day dataset (9-day-C) and 14-day duration dataset (14-day-D) with the vertical resolution of 2 km for nighttime and 4 km for daytime and the temporal resolution of 1 hour would yield the best-fit vertical profiles of diurnal and semidiurnal tidal amplitudes and phases for all three fields. These profiles with error bars are plotted in figure 5.2a for the diurnal component and figure 5.2b for the semidiurnal, along with the predictions of both GSWM00 (Global Scale Wave Model, version 2001) and GSWM02 (version 2002) for comparison. The difference between two model versions lies in the fact that GSWM02 includes both non-migrating and migrating effects while GSWM00 includes migrating tides only. In figure 5.2a, we can see that the two data sets, 9-day-C and 14-day-D, yield the same tidal amplitudes and phases. Data over a total of 14 days should be able to estimate tidal characteristics of the month, leading to a meaningful comparison with the model tides.

The diurnal amplitudes of temperature, zonal wind, and meridional wind observed by lidar are within 10 K, 20 m/s, and 15 m/s respectively for most altitudes between 80 km and 100 km. The phase plots clearly show the downward phase progression of diurnal tide with vertical wavelength of about 50 km in the temperature field and about 25 km in zonal wind and meridional wind. Different vertical wavelengths in temperature field and wind fields seen in most of our datasets could suggest different dominant diurnal tidal modes for temperature and winds. While there is negligible difference between the two GSWM predictions in diurnal phases, the GSWM02 diurnal amplitude typically is a factor of two larger. When observation and model predictions are compared, the agreement in diurnal phase is excellent for all three fields. The GSWM02 overestimates the diurnal amplitude, while the GSWM00 fares much better.

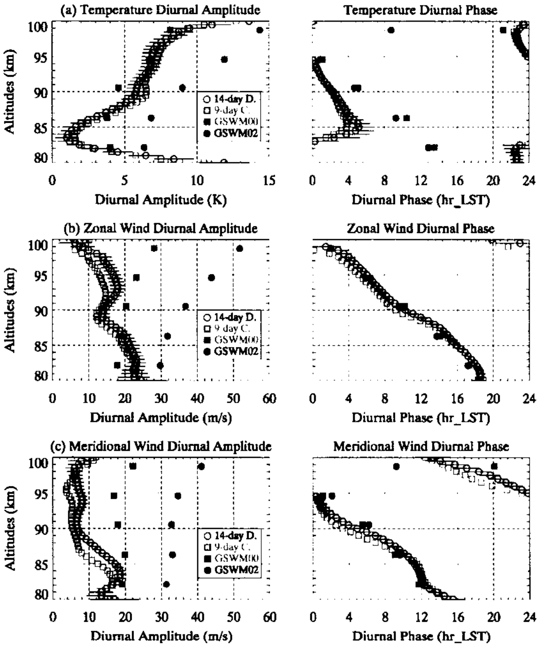

Figure 5.2a Vertical profiles of diurnal tidal amplitudes and phases of temperature, zonal wind, and meridional wind in the mesopause region for both 9-day continuous dataset and 14-day duration datasets. The predictions of both GSWM00 and GSWM02 are also plotted for comparison.

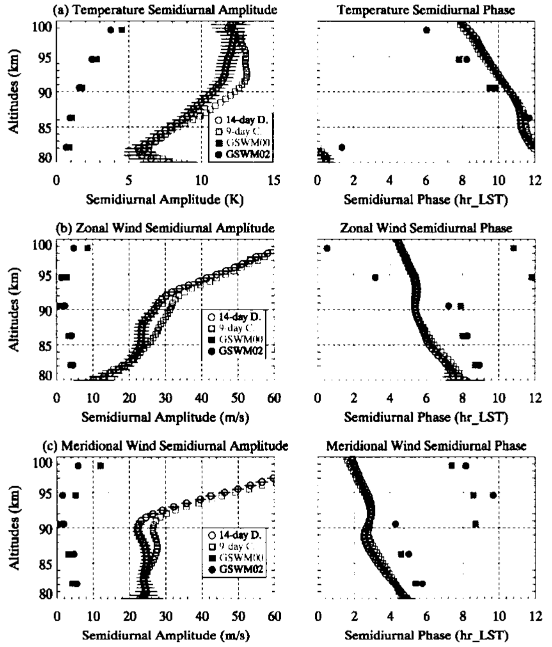

Figure 5.2b Vertical profiles of semidiurnal tidal amplitudes and phases of temperature, zonal wind, and meridional wind in the mesopause region for both 9-day continuous dataset and 14-day duration datasets. The predictions of both GSWM00 and GSWM02 are also plotted for comparison.

The semidiurnal tidal amplitudes of temperature, zonal wind, and meridional wind observed by lidar shown in the left column of figure 5.2b are much larger than the diurnal tidal amplitudes, especially above 90km. The semidiurnal amplitudes of temperature, zonal wind, and meridional wind reach maxima of 14K at 93km, 70m/s at 98km, and 80m/s at 98km respectively. Similar to diurnal phase plots, the downward phase progression of the semidiurnal phase shown in the phase plots of right column of figure 5.2b suggests that the dominant tidal sources are located in the lower atmosphere. However, the vertical wavelengths of semidiurnal tides in three fields are comparable and about 60km; this is a wavelength longer than those of diurnal tides shown in figure 5.2a, as expected [GSWM website]. Almost the same vertical wavelengths in temperature and wind semidiurnal tides are observed, suggesting that there are similar dominant modes appearing in all three components. The relation of three vertical phase profiles with the phase of meridional wind leading that of zonal wind, which in turn leads that of temperature, each by ~90°, is consistent with the polarization relations of upward and westward propagating gravity waves [Fritts and Alexander, 2003]. Meanwhile we see reasonable agreement in phases, with GSWM predictions underestimating the observed amplitude by an order of magnitude. The agreement between observation and the GSWM00 predictions suggest that the migrating tide dominates observed diurnal-period perturbations. The marginal agreement in semidiurnal phase along with much larger observed amplitudes suggests that either strong local sources exist or the model missed significant global sources with semidiurnal periods in September. Radar wind measurements from globally distributed stations for a summer campaign in 1999 [Pancheva et al., 2002] and from nearby Platteville, CO with two years of observation

[Manson et al., 2003] also found agreement with GSWM00 prediction in diurnal tides and discrepancy in semidiurnal tides.

5.2.2 Spectrum Analysis

For evenly sampled data [$h_n = h(n\Delta)$, where Δ is sampling interval and $n = -N,\ldots,-2,-1,0,1,2,\ldots,+N$], we could use fast Fourier transform methods to extract the frequency information. The Nyquist frequency (the highest frequency that can be coded at a given sampling rate in order to be able to fully reconstruct the signal) is $f_c = 1/(2\Delta)$ [Press et. al., 1997] for the evenly sampled data. This kind of the sampled data set contains complete information about all spectral components (i.e. at discrete frequencies 0,2,4,6….) in a signal h(t) up to the Nyquist frequency. There are situations, however, where evenly spaced data cannot be obtained. These situations, typical in our lidar observations, arise because the lidar beams are blocked by clouds leading to data gap, and/or because we are using different resolutions for daytime and nighttime data. There are some obvious ways to get from unevenly spaced t_i's to evenly spaced ones. Interpolation and zero-padding are common practice. However, such techniques lead to aliasing with un-realistic frequencies introduced. Fortunately, there is a completely different method of spectrum analysis for unevenly sampled data developed by Lomb [1976]. The Lomb method of spectrum analysis only evaluates the sines and cosines at the times that are actually measured.

For the N data points, $h_i = h(t_i)$; $i = 1, \dots, N$, the Lomb normalized periodogram (spectral power as a function of any angular frequency $\omega = 2\pi f > 0$) is expressed by:

$$P_N(\omega) \equiv \frac{1}{2\sigma^2}\left\{\frac{\left[\sum_j (h_j - \bar{h})\cos\omega(t_j - \tau)\right]^2}{\sum_j \cos^2\omega(t_j - \tau)} + \frac{\left[\sum_j (h_j - \bar{h})\sin\omega(t_j - \tau)\right]^2}{\sum_j \sin^2\omega(t_j - \tau)}\right\} \tag{5.1}$$

where

$$\bar{h} = \frac{1}{N}\sum_{1}^{N} h_i$$

$$\sigma^2 = \frac{1}{N-1}\sum_{1}^{N}(h_i - \bar{h})^2$$

Here τ is defined by relation [Press et al., 1997]

$$\tan(2\omega\tau) = \frac{\sum_j \sin 2\omega t_j}{\sum_j \cos 2\omega t_j}$$

In order to determine whether the measured points could be due to just (white) Gaussian noise, we need to find out the significance of a peak in the spectrum $P_N(\omega)$. The null hypothesis (the data values are independent Gaussian random values), a very nice property of the Lomb normalized periodogram, can be used to find out the significance level of any peak in $P_N(\omega)$ by evaluating the false-alarm probability of the null hypothesis. In the other word, the probability that $P_N(\omega)$ will be between some positive z and z + dz is exp(-z)dz. It readily follows that, if we scan some M independent frequencies, the probability that none give values larger than z is $(1 - e^{-z})^M$. So the false-alarm probability is given by [Press et. al., 1997]:

$$P(> z) \equiv 1 - (1 - e^{-z})^M \tag{5.2}$$

A small value for the false-alarm probability for a experimental signal indicates a highly significant periodic signal. Lomb Periodograms are an effective way to reveal the frequency contents in a data set including tidal periods. A Monte Carlo simulation with the same temporal structure is used to calculate the effective value of M and thus assign a percent probability that a given Lomb power would be present in random noise.

Using the 9-day continuous dataset with vertical resolution of 2 km (both day and night) and temporal resolution of 15 min (30 min) resolution for nighttime (daytime) observation, the normalized Lomb periodograms for temperature, zonal wind, and meridional wind are shown in figure 5.3 when calculated for periods of 1, 2, 3,...150hr. As expected, the diurnal and semidiurnal components in all three fields are very strong at all altitudes between 80 and 100 km, along with a noticeable terdiurnal component. In addition, we see in the temperature, a quasi 4-day period between 84km and 87km, a quasi 1.5-day period between 84km and 86km, in zonal wind component, a 1.5-day period between 84km and 88km, between 93km and 99km. In the meridional wind component we see a prominent quasi 5-day period between 89 and 95 km, a quasi 3-day period between 87 and 94 km, and a 1.5-day period between 85 and 88 km along with a weak but discernable 2-day feature near 86 km. These all likely represent planetary waves. The 1.5-day wave in temperature is not as significant as that in zonal wind and meridional wind. While they appear to be overpowered by the semidiurnal tide, there exists power at 20 hr, 14 hr and 10 hr periods in meridional wind, respectively, between 85 and 89, 90 and 100 km and 87 and 90 km. there also exsts power at 20 hr, 17 hr, 14 hr periods in zonal wind, respectively, between 85 km and 89 km, 85 km and 89 km, and 87 km and 100 km. These secondary/subsidiary peaks are likely the result of nonlinear interactions, similar to those identified in our April 2002 data [She et al., 2003].

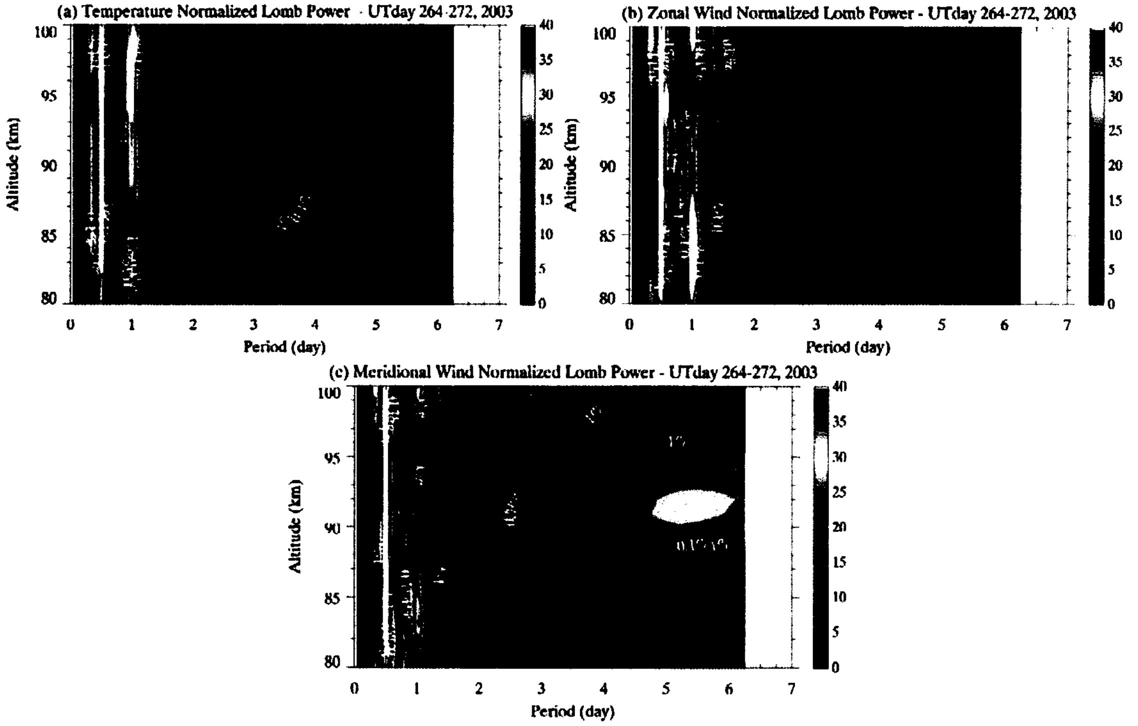

Figure 5.3 Normalized Lomb power contours of temperature, zonal wind, meridional wind based on the 9-day continuous dataset are shown with the contour lines corresponding to 0.1% (solid line) and 1% (dot line) probability resulting from random noise marked..There is only a 1×10^{-5}% probability that a Lomb power of 20 would be generated by Gaussian noise for our observation times and the frequencies investigated.

Table 5.1 Significant non-tidal-period oscillations

Dynamic field	Period	Range (km)	Sources (primary periods)
Temperature (T)	102hr	85-88	Quasi 4-day
Zonal Wind (U)	14hr	87-100	Nonlinear (12h, 3d)
	17hr	89-93	Nonlinear (12h,1.5d)
	20hr	85-89	Nonlinear (1d, 5d)
	36hr	84-88, 93-99	Quasi 1.5-day
Meridional wind (V)	10hr	87-90	Nonlinear (12h, 3d)
	14hr	90-100	Nonlinear (12h, 3d)
	20hr	85-89	Nonlinear (1d, 5d)
	36hr	85-88	Quasi 1.5-day
	70hr	87-94	Quasi 3-day
	130hr	89-95	Quasi 5-day

We tabulate the observed periods with significant Lomb power (having less than 0.1% probability of being due to random noise) for temperature, zonal and meridional winds in Table 5.1, along with a preliminary indication of their possible sources. However, the frequency relationship between the primary and secondary waves alone is not enough to unequivocally ascribe the nonlinear interaction, because the vertical wavenumber of the secondary wave needs to be determined. Since this will depend not only on the primary wavenumbers but also on the depth of the interaction region as well as the specific mode of the secondary wave, a more detailed study is obviously necessary for their full understanding. Thus, while Table 5.1 suggests the richness of this data set, the explanation put forth is merely plausible and not definitive.

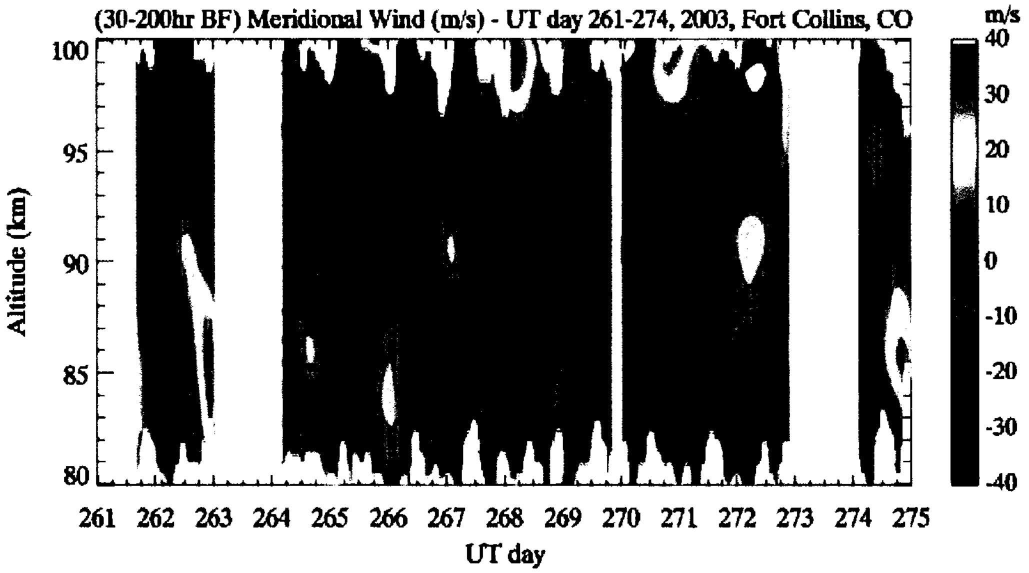

Figure 5.4 Filtered meridional wind contours by a band-pass filter with sharp cutoffs at 30 and 200 hours.

To reveal the coherence of the observed planetary waves, contours of the meridional wind in 1hr intervals of the 14-day duration data set, filtered by a band-pass filter with sharp cutoffs at 30 and 200 hours, are shown in figure 5.4. A wind minimum with a period of ~3 days is clearly seen to progress downward at ~1.3km/day. Phase progression with ~1.5-day period (yellow maxima) can also be seen below 90 km. In addition, maxima near days 262, 267 and 272 at 90 km suggests the presence of a quasi 5-day perturbation.

5.2.3 Tidal day-to-day variability

Using the 9-day continuous data set with 2 km and 15-30 min resolution, we have performed a running tidal analysis using individual 24-hour continuous data sets, centered at each hour. The method of analysis for tidal variability was discussed in detail in section 5.1.2. The variability (in absolute values) is smallest in diurnal-means and largest in semidiurnal amplitudes, consistent with considerable nonlinear interactions associated with 12hr period, see Table 5.1. Diurnal and semidiurnal amplitudes and phases of temperature, zonal wind, and meridional wind are shown in figure 5.5. This shows not only day-to-day variability but also a large increase in amplitudes between noon, day 266 (Sep 23) and noon, day 268, with the maximum increase in diurnal amplitude which leads that in semidiurnal amplitude by about half a day. We note that though the variability in diurnal phases is larger in comparison, the altitude-dependent semidiurnal phases remain constant within two hours at each altitude in these 9 days.

The variability of the apparent tidal amplitudes and phases could be caused by interactions with planetary waves on global scales [Hagan and Roble, 2001] or interactions with gravity waves, or a combination of both. As shown in figure 5.3 and 5.4,

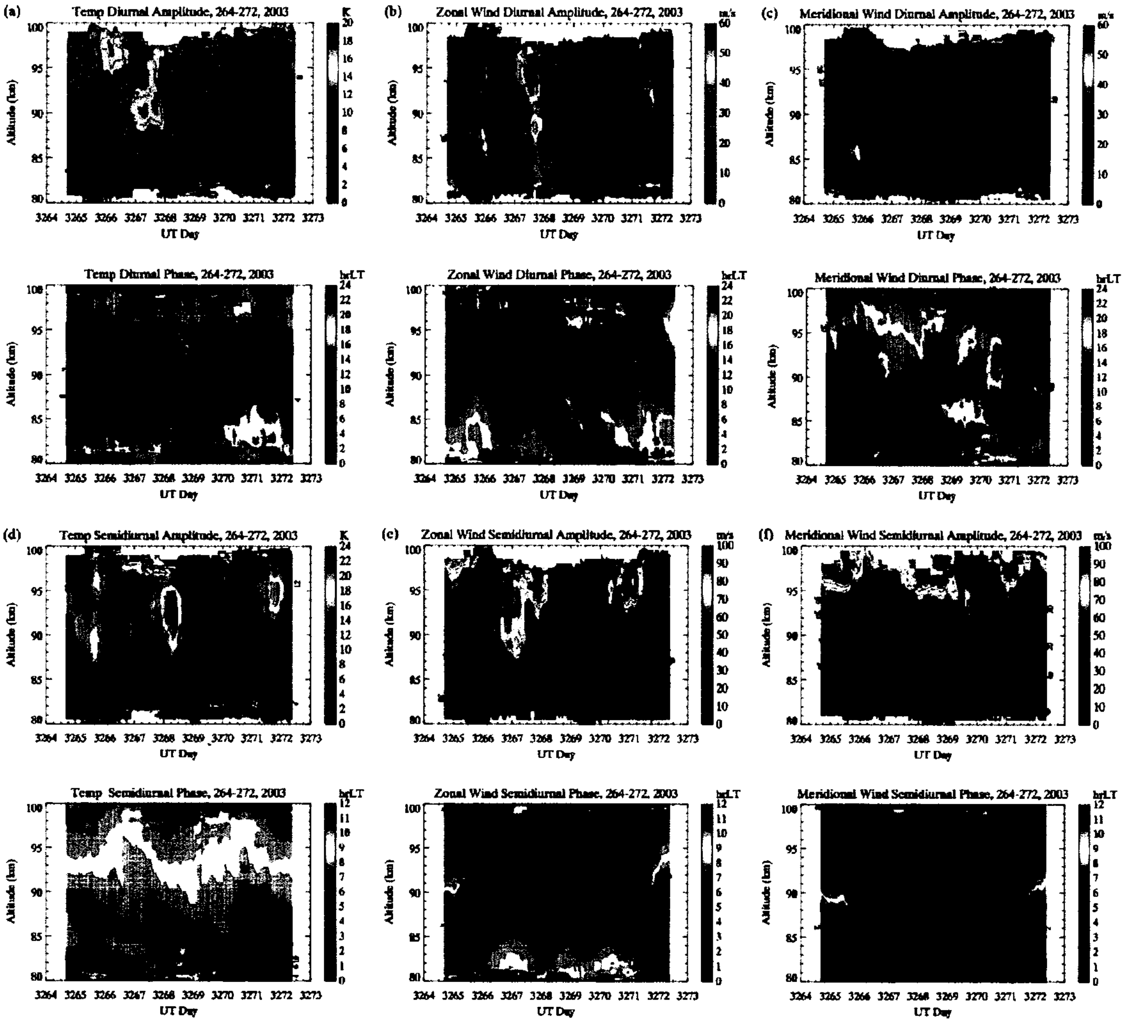

Figure 5.5 Variability in diurnal (a, b, c) and semidiurnal (d, e, f) amplitudes (top) and phases (bottom) of temperature (a, d), zonal wind (b, e), and meridional wind (c, f) during 9-day observation. Notice scale differences.

perturbations with periods of 1.5-day, 3-day, and quasi 5-day are present during these 9 days, which may be associated with planetary waves. Previous studies [Meyer and Forbes, 1997] demonstrated that planetary waves with a period near 6.5-days may indeed peak around equinox. The local apparent tidal amplitudes and phases may also change due to interactions with gravity waves [Waterscheid, 1981; Fritts and Vincent, 1987]. The tides modulate the atmospheric stability and thus GW breaking, and the wave breaking leads to changes of local mean wind and temperature. The temperature inversions thus formed can be strong and are characterized by near adiabatic lapse rates at the top side due to turbulent mixing in the wave breaking region. At the same time, momentum deposition due to wave breaking changes the zonal wind. Temperature inversions with overlying adiabatic or near adiabatic lapse rates were indeed observed on days 267 and 268, which we will discuss in detail below.

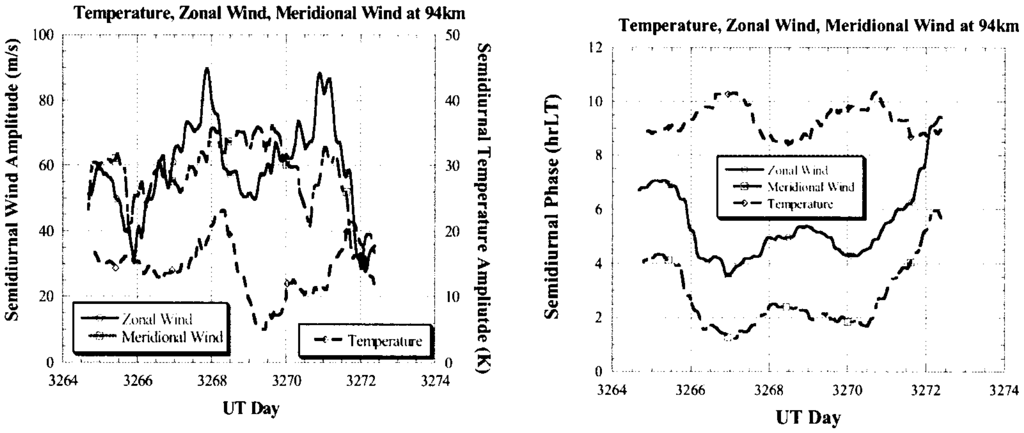

Figure 5.6 Semidiurnal tidal amplitude and phase variability of the temperature, zonal wind, and meridional wind at 94km during 9-day continuous observation.

Shown in figure 5.6 are the time series of the semidiurnal amplitude and phase of temperature, zonal wind, and meridional wind at 94 km. The plots clearly show the quasi 3-day wave oscillations, especially in the phase plots. The time series of zonal wind phase showed the similar wavelike pattern as that of meridional wind phase, but with 2-3 hours delay expected from the polarization relation. However, the temperature phase evolved 180° out of phase from those of winds'. According to polarization relation of gravity waves, we expect the phases of all three components to follow each other within about a 3-hour (90°) difference. The reason for the anomalous behavior in temperature phase change is not yet clear and is still under investigation.

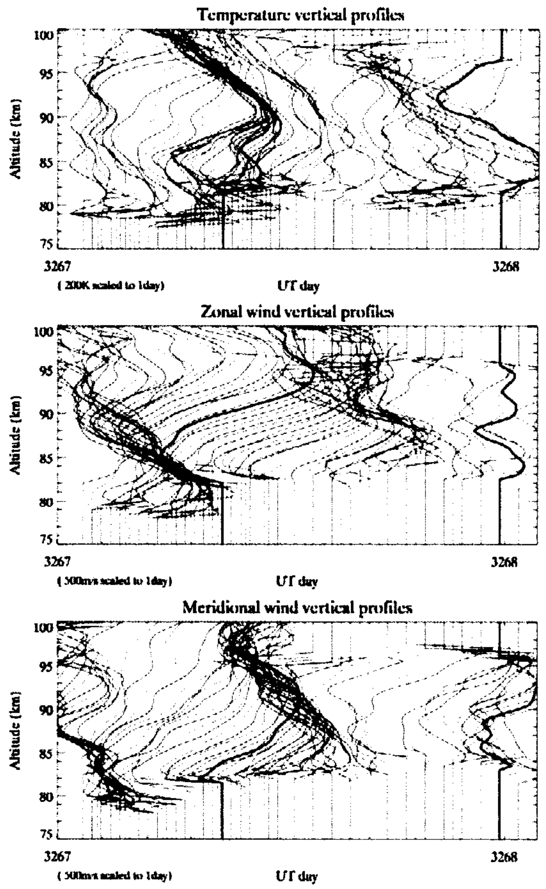

Figure 5.7 the time series change of vertical profiles of temperature (upper panel), zonal wind (middle panel), and meridional wind (bottom panel) with vertical resolution of 2km and temporal resolution of 15min for nighttime and 30min for daytime in UT day 267. Red and blue lines alternate in time. Note that 1 day is scaled to 200K for temperature and 500m/s for wind.

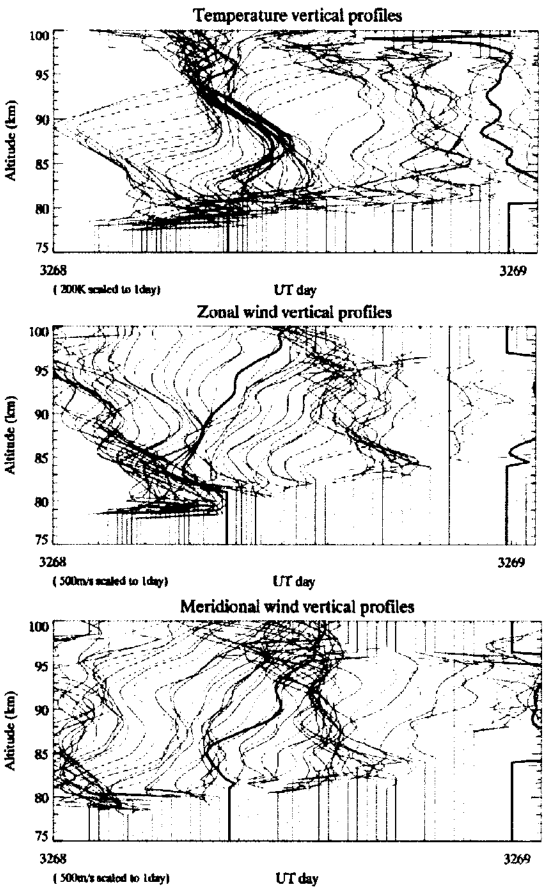

Figure 5.8 the time series change of vertical profiles of temperature (upper panel), zonal wind (middle panel), and meridional wind (bottom panel) with vertical resolution of 2km and temporal resolution of 15min for nighttime and 30min for daytime in UT day 268. Note that 1 day is scaled to 200K for temperature and 500m/s for wind.

In order to look further at detailed profiles for UT days 267-268 when a 2-fold increase of diurnal and semidiurnal tidal amplitudes was observed by lidar, we plot in figure 5.7 the time series of vertical profiles in temperature, zonal wind, and meridional wind with the vertical resolution of 2 km and temporal resolution of 15 min for nighttime and 30 min for daytime in UT day 267-268. Temperature profile is shifted ~2 K for every 15-min profile and ~4 K for every 30-min profile, centered at 180 K. Correspondingly, the origins of the profiles for both zonal and meridional winds are shifted 20 m/s and 40 m/s, respectively. In temperature profiles, we can see two strong inversion layers, one is ~25 K at ~07:30 UT near 90 km with the vertical temperature gradient of ~-8.5 K/km above, and another is ~30 K inversion at ~23:00 UT near 85 km. The height and the time of the nighttime inversion layer correspond to those of the big tidal increase shown in diurnal tidal amplitude contour of figure 5.5. The corresponding zonal wind changes from -90 m/s at 86 km to 90 m/s at 96 km with maxima wind shear of ~25 m/s/km near 90 km, and meridional wind changes from -60 m/s at 83 km to 60 m/s at 95 km with maxima wind shear of ~18 m/s/km near 86 km. The nighttime temperature inversions around 90 km are seen between 04:00 and 11:00 UT, while zonal wind and meridional wind profiles were observed with downward phase progression. The zonal and meridional wind shears corresponding to the daytime inversion layer are not as strong as those observed in the nighttime. As shown in figure 5.8, the strong temperature inversion near 87 km with ~25 K amplitude was also observed at ~08:30 UT. Above the inversion layer, the temperature gradient is ~ -7 K/km which is not as steep as that observed in nighttime of day 267. The corresponding zonal wind changes from -50 m/s at 83 km to 70 m/s at 96 km with maxima wind shear of ~15 m/s/km near 90 km, and meridional wind changes from -30 m/s at 85 km to 90 m/s at 95 km with maxima wind shear of ~20 m/s/km near 88 km. The horizontal wind shear in the nighttime of day 268 is weaker than that observed in the nighttime of day 267. The nighttime inversion layer near 87 km is persistent for ~4 hours between 06:00 and 10:00 UT. The downward phase progression could also be seen in the zonal wind and meridional wind plots. The strong temperature inversion with big wind shears indicates the possible dynamic or convective (static) atmospheric instability in the mesopause region. Furthermore, it could also suggest possible tidal/gravity wave interactions

5.2.4 Temperature Comparisons between Lidar and TIMED/SABER

The TIMED (Thermosphere, Ionosphere, Mesosphere, Energetics and Dynamics) satellite was launched on December 7, 2001 and carries 4 instruments to study the atmosphere with 60-180km as core altitudes. One of the instruments is SABER (Sounding of the Atmosphere using Broadband Emission Radiometry), which is a multi-channel infrared radiometer that measures atmospheric temperature and a variety of chemical species [Saber Website, http://saber.larc.nasa.gov/]. The kinetic temperature profiles are retrieved from the measurements of CO_2 emission centered in the 15μm band Earth limb emission under conditions that are not in local thermal equilibrium (LTE) [Mertens et al., 2001]. In the MLT region, both LTE and non-LTE analysis are essential.

During our 14-day campaign in September 2003, fortunately the SABER also continuously operated over the globe. Therefore, the SABER global temperature structures provide some global tidal structure information and can be used to compare with our locally lidar observed tidal-period perturbations. Here we will limit our comparison between lidar temperature and SABER temperature on only two UT days, 267 and 268 when the 2-fold increase of tidal amplitudes was observed by lidar. Shown in figure 5.9 is the SABER latitude versus longitude footprint for UT day 267 (Sept. 24, 2003). Since satellite follows yaws orbits, the measured SABER temperature will include descending temperature, which is nighttime temperature, and ascending temperature, which is daytime temperature, both with almost fixed local times (for descending orbit the local time is ~01:00am, for ascending orbits is ~10:00am). Figure 5.10 shows the vertical temperature profile comparison between lidar and SABER at UT time around 8:00am (LT 1:00am) when SABER almost passed over our lidar station at Fort Collins, CO in UT day 267. The excellent agreement between two temperature profiles below 95km can be clearly seen. Above 95km, lidar observed temperature is a little warmer than SABER observed temperature. The difference could be attributed to the retrieval method for SABER nighttime temperature. Meanwhile, both profiles show the strong temperature inversion (temperature warming above a positive lapse rate in the bottom portion of the temperature profiles) with nearly adiabatic lapse rate above 90 km, which indicates the possible tidal/gravity wave interactions.

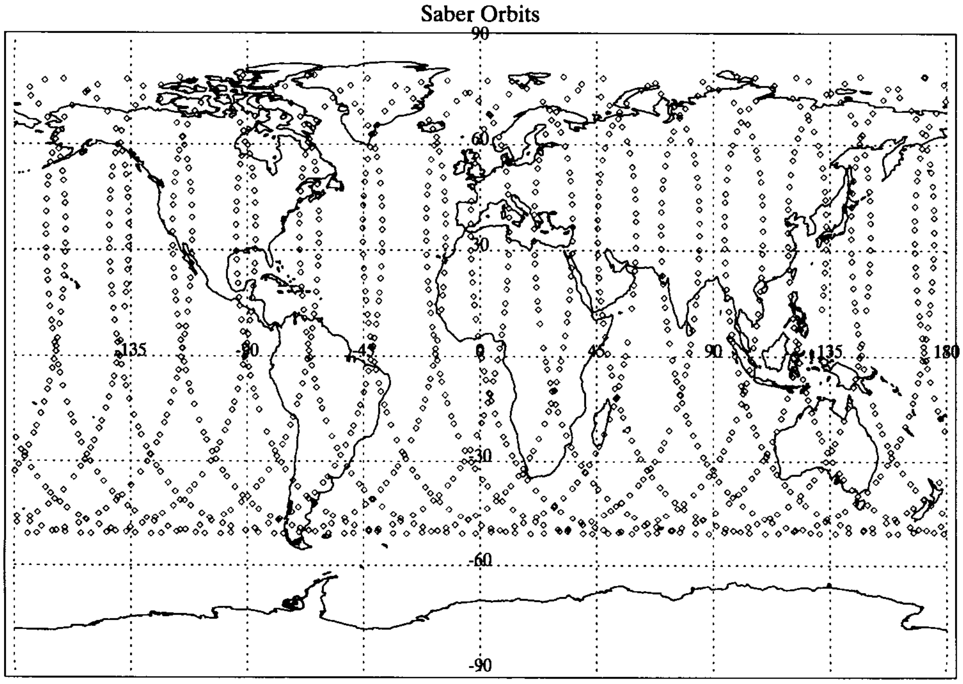

Figure 5.9 the SABER latitude versus longitude orbit for UT day 267

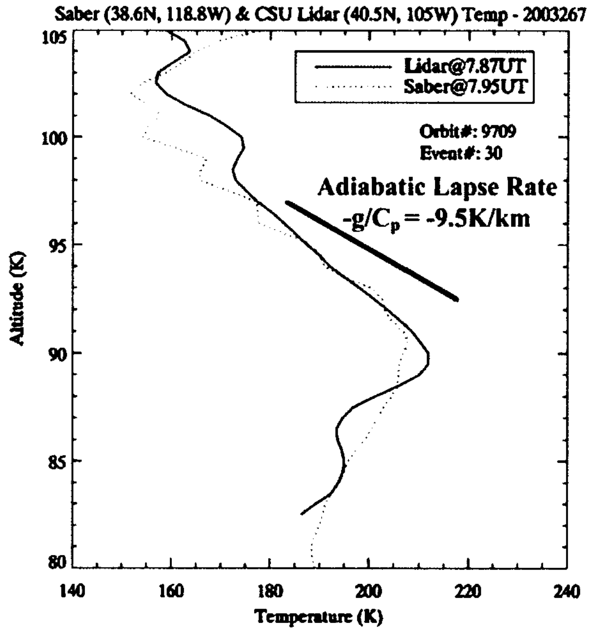

Figure 5.10 the vertical temperature profiles of lidar (blue solid line) and SABER (red dot line) at UT time around UT 8:00am (LT 1:00am)

Since SABER measures global temperature at the same local time, we could plot the longitudinal distribution of temperature by only looking at the middle latitude. Shown in figure 5.11 are the contour plots of the longitudinal distribution of SABER ascending (upper panel) and descending (bottom panel) temperature averaged over 10° of latitude from 35°N to 45°N. In the contour plot of descending temperature, a strong inversion is observed at ~250°E (our lidar station is at 255°E with a vertical temperature gradient of ~-8 K/km, which is close to the adiabatic lapse rate of -9.5K/km. Although high temperature (~230°C) at 80°E and 85 km is observed, the temperature gradient for that longitude is only ~5 K/km. Whereas in the ascending temperature plot, the weak inversion could be seen at 120°E with temperature gradient ~-4 K/km. Shown in figure 5.12 are SABER footprints over US and contour plots of latitudinal distribution of SABER temperatures for one ascending orbit and one descending orbit which are the closest orbits that passed over our lidar station on UT day 267. It can be seen in the descending temperature plot that with the exception of high temperatures in the equatorial region which are most likely due to strong diurnal tidal oscillation, a strong temperature inversion layer above 90 km at 35°N is observed, which is consistent with our lidar observation. For the ascending temperature, SABER also observed a weak inversion layer above 85 km near 30°N, whereas our lidar observed an inversion layer much late at LT 5:00 pm, but nearly at the same altitude range (see figure 5.7 in section 5.2.3).

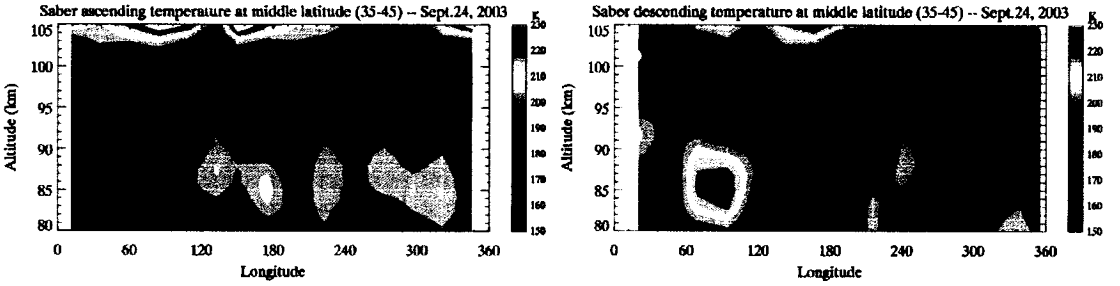
Saber ascending temperature at middle latitude (35-45) -- Sept.24, 2003

Saber descending temperature at middle latitude (35-45) -- Sept.24, 2003

Figure 5.11 Contour plots of longitudinal distribution of SABER ascending and descending temperature by averaging over 10° of latitude from 35°N to 45°N in UT day 267.

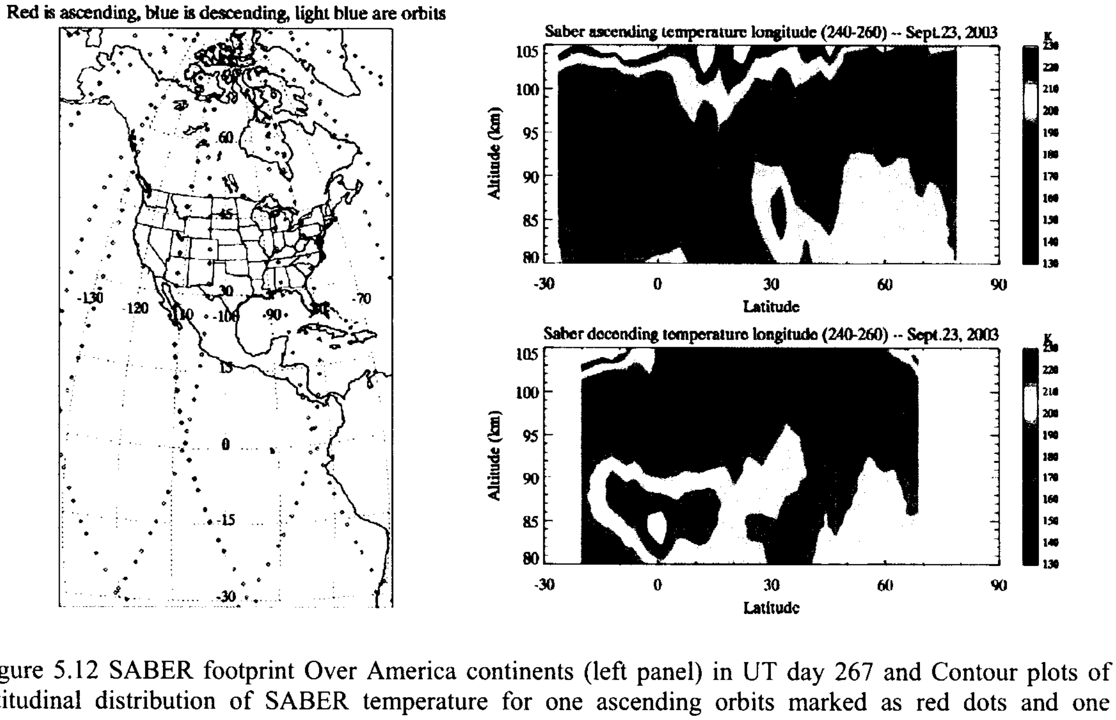
Red is ascending, blue is descending, light blue are orbits

Saber ascending temperature longitude (240-260) -- Sept.23, 2003

Saber decending temperature longitude (240-260) -- Sept.23, 2003

Figure 5.12 SABER footprint Over America continents (left panel) in UT day 267 and Contour plots of latitudinal distribution of SABER temperature for one ascending orbits marked as red dots and one descending orbits marked as blue dots.

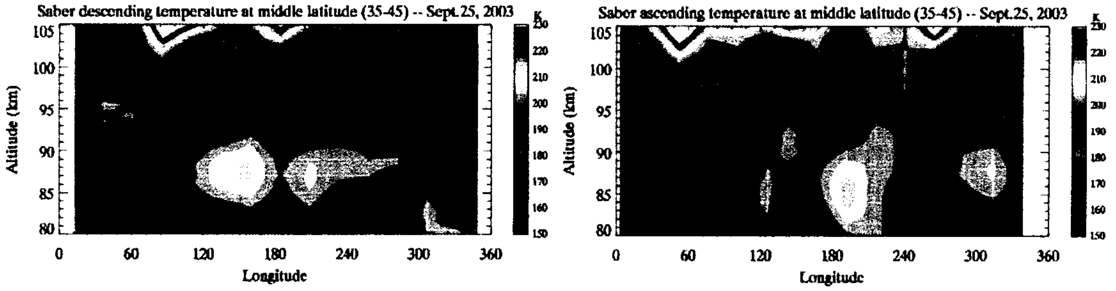

Figure 5.13 Contour plots of longitudinal distribution of SABER ascending and descending temperature by averaging over 10° of latitude from 35°N to 45°N in UT day 268.

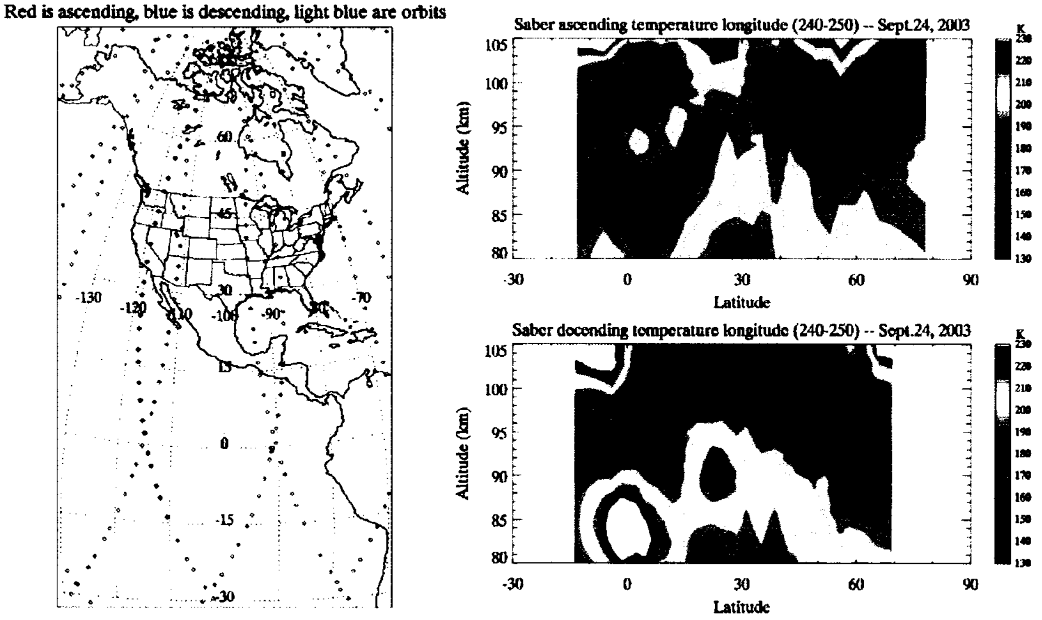

Figure 5.14 SABER footprint Over America continents (left panel) in UT day 268 and Contour plots of latitudinal distribution of SABER temperature for one ascending orbits marked as red dots and one descending orbits marked as blue dots.

The longitudinal and latitudinal distribution of SABER temperature for UT day 268, are shown in figures 5.13 and 5.14. Strong temperature inversions between 20°N and 40°N in the nighttime were also observed. After looking at the global SABER temperature structures, we note that the 2-fold increase we observed on the tidal amplitudes in UT day 267 and 268 is large regional phenomena rather than global phenomena. However, it could be still due to both tidal/planetary wave interactions and tidal/gravity wave interactions. In the upcoming sections, we will discuss two related topics that support our hypothesis. They are (1). The TIME-GCM simulations, which demonstrate that the interactions of a transient quasi-stationary planetary wave with tides could introduce strong short-term tidal variability and strong temperature inversions in the mesopause region, and (2). Likely additional tide/gravity wave interaction on these 2 days.

5.2.5 TIME-GCM simulation

The Thermosphere-Ionosphere-Mesosphere-Electrodynamics General Circulation Model (TIME-GCM), an extension and the most elaborate of the upper-atmospheric Thermospheric General Circulation Models (TGCM's) [Dickinson et al., 1981], is being developed by the National Center for Atmospheric Research (NCAR) [Roble et al., 1994]. TIME-GCM solves for global distributions of neutral and plasma temperatures, velocities, and compositions, including all of the species that are photochemically important in the mesosphere, thermosphere, and ionosphere. The TIME-GCM includes all of the processes incorporated into the TIE-GCM. It is unique in its range of altitude coverage (30-500 km), with the critical mesosphere/lower thermosphere region in the center of its numerical grid, allowing dynamical, chemical, radiative, and electrodynamical couplings between the thermosphere and mesosphere to occur without major boundary influences. A TIME-GCM modeling study could be used to interpret tidal day-to-day variability due to the interactions between tides and planetary waves. Since the TIME-GCM solves the spherical primitive equations and has a spatial resolution of 5x5 degrees, it can be used to study the propagation and interaction of planetary scale waves. We can control the forcing of planetary waves at the lower boundary, so that planetary waves with specific wavenumber and period can be represented in the model. By comparing the results from controlled numerical experiments with and without the planetary wave(s), we will be able to study the interactions between tides and planetary waves and their implications for mesospheric variability. On the other hand, mesoscale gravity waves can not be resolved by the TIME-GCM because their scales are smaller than the model grid size.

Coincident with the 2-fold increase of tidal amplitudes in UT day 267 and 268, the strong temperature inversion layers were also observed. Examination of the SABER temperature at the same time not only confirms the existence of the inversion layers but also reveals the superposition of global and local inversions. It thus suggests the presence of a planetary wave in the mesosphere, according to Sassi et al [2002]. Because the strong inversion was only observed for a few days, the planetary wave was probably a transient wave, consistent with previous studies of planetary waves around equinox [Taylor et al., 2001, Liu et al., 2001]. Since the large tidal variability may be a consequence of the interaction between the transient planetary wave and the tides, two TIME-GCM runs were made [Liu, private communication] to study the possible impact of planetary waves on tides: One is the base case, where no planetary wave is added, and the other is a control case where a wavenumber 1 quasi-stationary planetary wave (QSPW) is added. The QSPW is forced between 30 and 90 N with peaks at 60N. In time, the wave amplitude has a Gaussian shape with peak on day 265 and 2 day half width. The maximum amplitude of the geopotential height perturbation at 60N on day 265 is 2000

m. The objective of the experiment is to simulate a transient QSPW and its interaction with the tides. The simulation starts on day 255 and stops on day 280. Note that NCEP (National Centers for Environmental Prediction) forcing is not added to the simulation in order to easily control the simulation.

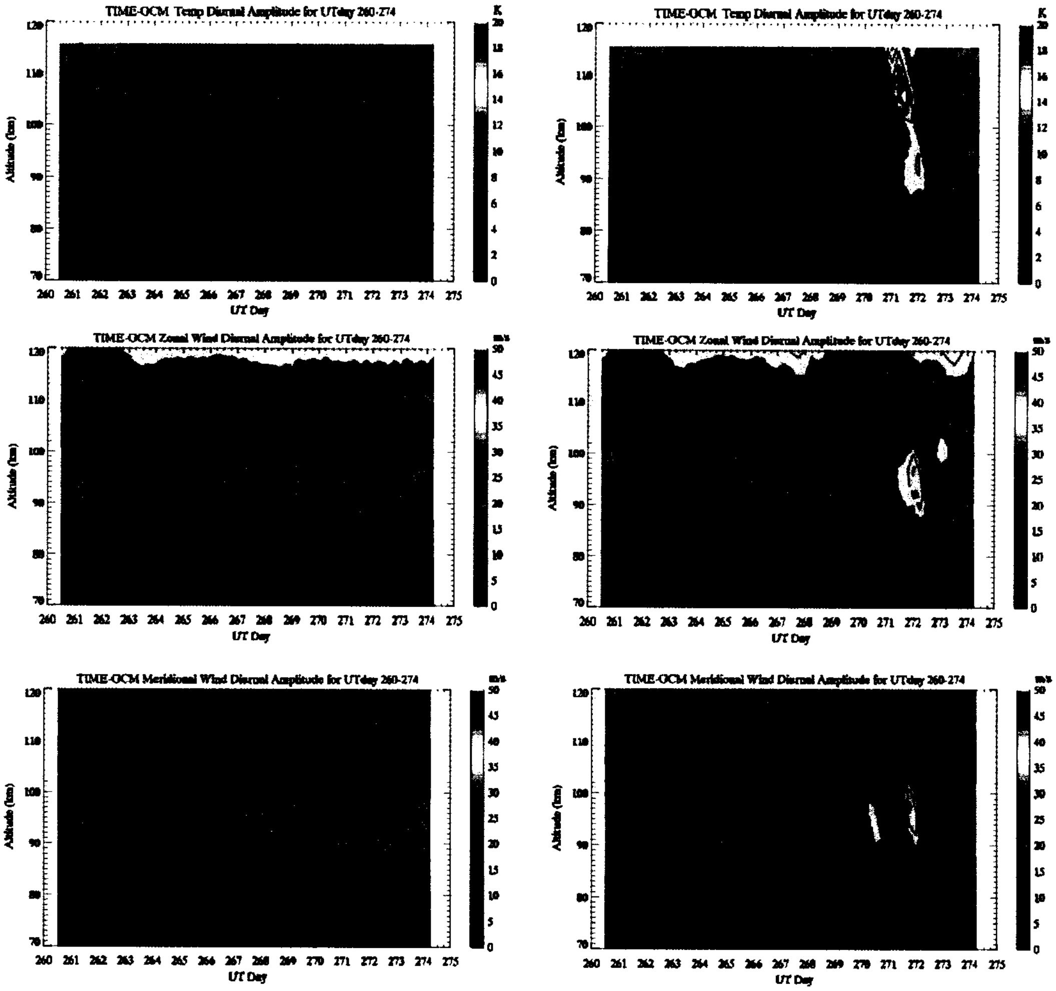

Figure 5.15 Tidal day-to-day variability for the location at 42.5N, 105W (Fort Collins, CO, 40.5N, 105W). Contours on the left column are base cases. Contours on the right column are control cases. Control cases show a strong tidal amplitude increase on UT day 271-272. Vertical profiles of TIME-GCM control case on 272 and lidar on UT 267 show general agreement.

Shown in the figure 5.15 are the contour plots of temperature (top panel), zonal wind (middle panel), and meridional wind (bottom panel) simulated by using TIME-GCM for two cases, base case (left column) and control case (right column). The simulation shows that the zonal wind and temperature tides (diurnal and semi-diurnal) both increase and decrease rapidly as a result of the interaction, peaking on day 270, 271, or 272, depending on the altitude/latitude and which component. The S=1 QSPW does produce an inversion layer between 90 and 100 km at certain longitude, though not as strong as that observed by the lidar, seven days after the QSPW was launched, as shown in figure 5.16. So the numerical experiments demonstrate that planetary wave and tidal interaction can introduce strong short term variability to the tides.

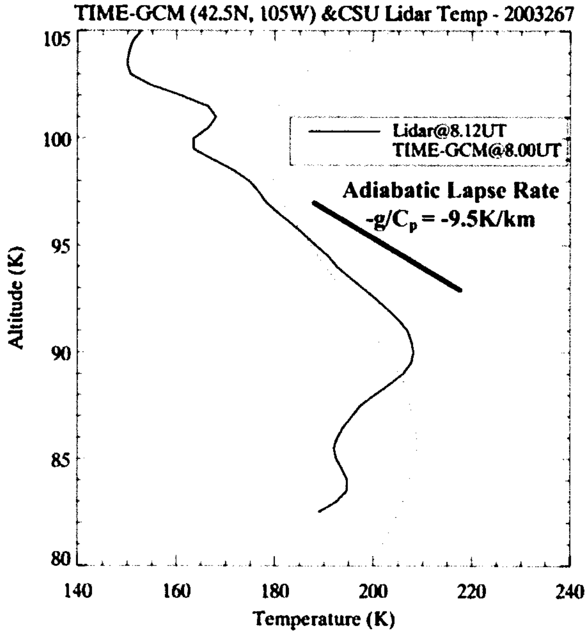

Figure 5.16 Comparison of the vertical profiles between lidar and TIME-GCM simulation at 08:00 UT. Temperature inversions are seen on both profiles. But inversion observed by lidar is stronger than that simulated by TIME-GCM.

5.2.6 Possible tidal/gravity wave interactions

The TIME-GCM simulation demonstrates that planetary wave and tidal interaction can introduce strong short term variability in the tides, such as observed in UT day 267 and

268. As shown in figure 5.16, the temperature inversion observed by lidar is larger than that simulated by TIME-GCM, which suggests that in addition to tidal/planetary wave interactions, tidal/gravity wave interactions could further increase the temperature gradient above the inversion layer. A simulation of gravity wave and tidal coupling was reported by Liu and Hagan [1998]. Wave breaking can induce downward heat flux causing cooling in the breaking region and heating right below it. The maximum heating corresponds closely with a negative or positive wind shear due to gravity wave acceleration. In order to explain the governing mechanism in this process, the paper also presented a simple schematic of the interaction between a tidal wave and a propagating gravity wave, which is shown in figure 5.17.

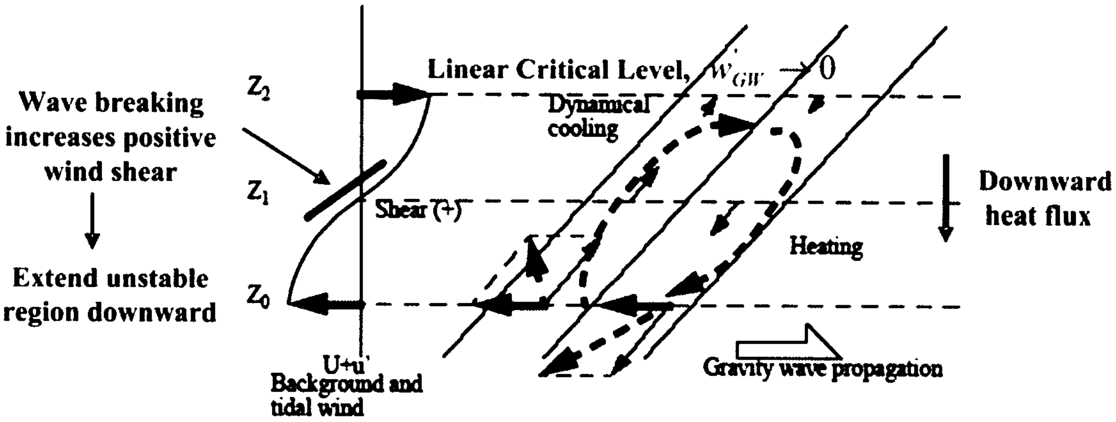

Figure 5.17 Schematic of a propagating gravity wave interaction with background and tidal wind. Thin arrow: gravity wave wind; thick solid arrow: background and tidal wind; thick dash arrow: composite wind. [Courtesy of Liu, GRL, 1998]

When an eastward propagating gravity wave is approaching the linear critical level at altitude Z_2, the vertical velocity perturbation of the gravity wave diminishes in amplitude toward zero asymptotically. The composite wind constructed from the superposition of the gravity wave wind and background and tidal wind appears as a circulation shown in the figure 5.17 with thick dash line. Dynamic cooling due to circular motion will be maxima at altitude Z_2. When approaching linear critical level at Z_2, gravity waves will become unstable (dynamical, $0<Ri<0.25$, or, convective, $N^2 < 0$, $Ri <0$ instability due to increase of the vertical shear of horizontal wind or increase of the negative temperature gradient [Nappo, 2002]) and break (wave field breaks down to turbulence). In real observation, the wave does not collapse. Instead, only the top parts of the wave collapse. This dissipation process is called wave saturation. [Fritts, 1984; Lelong and Dunkerton, 1998]. At this altitude, the breaking wave deposits momentum in the medium and thus accelerates the mean flow. In the unstable region, the downward heat flux is enhanced when eddy diffusion increases due to turbulence mixing, thus heating is caused. Cooling at the top of circulation and heating below it will increase the negative temperature gradient, and thus increase the temperature inversion. Meanwhile, the acceleration of mean flow will increase positive wind shear. As a result, the unstable region is extended downward. The relative location of the heating/cooling region with respect to the tidal temperature perturbation depends on the phase relation of the tidal wind perturbation and tidal temperature perturbation.

In order to show the vertical profiles of background tides in three fields (T, U, V), we reconstruct them from the 9-day mean tidal values which are shown in figures 5.2a and 5.2b. The background profiles did not account for the effect of tidal/planetary wave interactions. At the same time, since we have the tidal values for every hour obtained by tidal fitting within a running 24hr window, we could also reconstruct the vertical profiles for "real-time" observed atmosphere. The reconstruction of the vertical profiles only includes 24hr mean, diurnal, semidiurnal, and terdiurnal tides. Since terdiurnal tide is much smaller than diurnal and semidiurnal tides, there will not be much difference with or without terdiurnal included. The time series of reconstructed vertical profiles of zonal wind, meridional wind, and temperature (with residual term removed) are shown in figure 5.18, 5.19, and 5.20 respectively. The left panel of each figure is constructed from the 9-day mean tidal values, whereas the right panel of each figure is constructed from "real-time" atmospheric tides with running 24-hour tidal fits.

From these figures we can clearly see that the real-time atmospheric zonal wind shear, meridional wind shear, and negative temperature gradient are much larger than those in background atmosphere. We also find that at the altitudes where the lapse rate is nearly adiabatic, the minimum and maximum temperature gradients due to the semidiurnal and

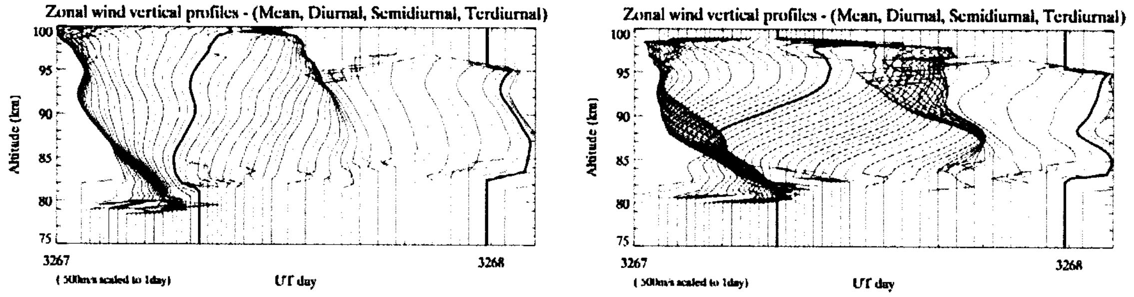

Figure 5.18 Reconstructed vertical profiles of zonal wind from 9-day mean tidal values (left panel) and from tidal values obtained by doing tidal fitting within a running 24-hr window (right panel). Note 1 day is scaled to 500m/s.

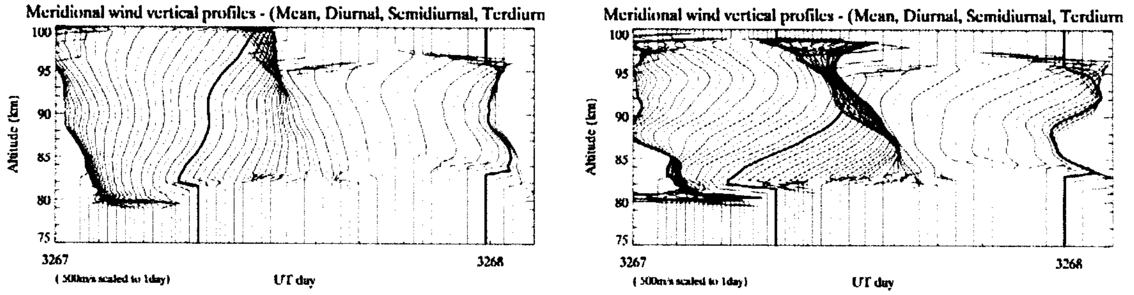

Figure 5.19 Reconstructed vertical profiles of meridional wind from 9-day mean tidal values (left panel) and from tidal values obtained by doing tidal fitting within a running 24-hr window (right panel). Note 1 day is scaled to 500m/s.

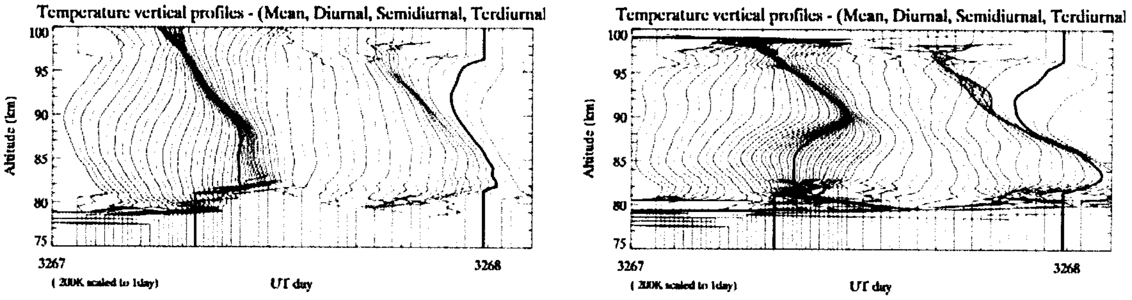

Figure 5.20 Reconstructed vertical profiles of temperature from 9-day mean tidal values (left panel) and from tidal values obtained by doing tidal fitting within a running 24-hr window (right panel). Reconstructed profiles include only diurnal mean, diurnal, semidiurnal, and terdiurnal tides. Note 1 day is scaled to 200K.

diurnal tides are coincident at the same altitudes. As a result, the total negative temperature gradient due to tidal contribution was increased to near adiabatic lapse rate. Similar phenomena are observed in both zonal wind and meridional wind components. The observed strong temperature inversion and accompanying large change of the horizontal wind in the small altitude region are consistent with wave breaking or overturning of isentropic surface. If there is a gravity wave propagating northeastward, the gravity wave will tend to become dynamically or convectively unstable when it approaches the linear critical level above ~90 km. According to the tidal/gravity wave coupling model shown in figure 5.17, the gravity wave will break and then deposit its positive momentum into the background flow. The zonal wind shear will then tend to increase and further extend the unstable region downward. This can be seen in the vertical profiles of real-time atmosphere in the right panel of figure 5.18 and 5.19. Downward heat flux with dynamic cooling near the linear critical level and heating below it will increase the negative gradient of temperature shown in the right panel of figure 5.20. Therefore, the observations in UT day 267 suggest good agreement with idealized modeling study of tidal/gravity wave coupling [Liu and Hagan, 1998]. Similar conclusions are found for UT day 268. The temperature inversion on day 267 is most likely due to diurnal tide, whereas, temperature inversion in day 268 is mainly due to semidiurnal tide.

Fortunately, we did observe the gravity wave activities on both UT day 267 and 268. By subtracting the real-time mean and tidal components from raw data, we obtained residuals, which include a component of the perturbations with periods less than 24 hr. Then using residual data, we plot the hodographs of zonal wind versus meridional wind, and of in-phase horizontal wind (the sum of projections of zonal wind and meridional wind onto the major axis of fitted ellipse in u-v plot) versus temperature, which are shown in figure 5.21a for UT day 267 and figure 5.21b for UT day 268 both at ~3:40 am. According to the hodograph analysis of inertial gravity waves discussed previously in section 4.3, we can identify two gravity waves in UT day 267 from figure 5.21a. One gravity wave propagates at azimuth angle of ~190° (Due north = 0° azimuth angle, clockwise from the north), and another gravity wave propagates at azimuth angle of ~290°. Both gravity waves are upward propagating waves, and last for only 1-2 hours from 3:00am to 4:30am LT. However, for the case of UT day 268, only one upward propagating gravity wave can be identified from figure 5.21b with horizontal propagating azimuth angle of ~240°. This gravity wave lasts about 4 hours from 1:00am to 5:00am. Since zonal wind and meridional wind both change from large negative value at lower altitude z (~83km) to large positive value at higher altitude z (~96 km) with positive wind shears in both days, the linear critical levels are likely to be formed specifically between 85km and 92km for the nighttime of day 267, and below 85 km for the nighttime of day

268 when these gravity waves propagate upward into the mesopause region. When they approach linear critical levels, these waves become unstable and tend to break. It is our hypothesis that tidal/gravity wave interactions occured and further more fed back to modify the tides. The increased tides could be seen in figures 5.18, 5.19, and 5.20.

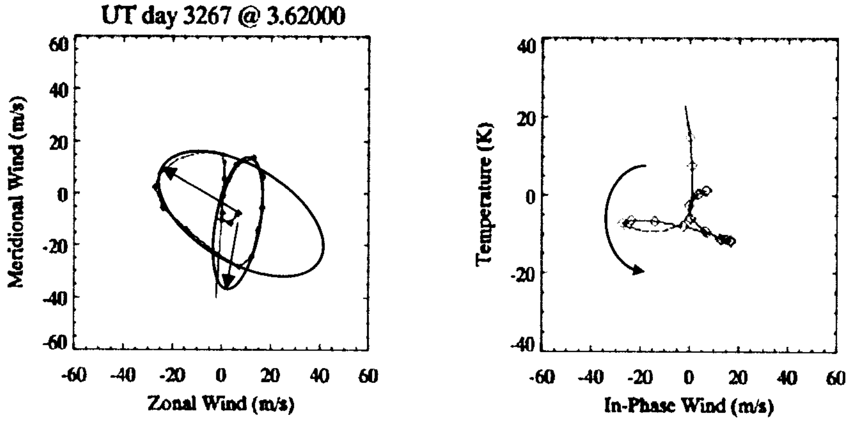

Figure 5.21a Hodographs of zonal wind vs. meridional wind (left panel) and of temperature vs. in-phase wind (right panel) for UT day 267 at 03:37am. The colors from dark to red denote the altitudes from 83 km to 96 km. The ellipses are fitting curves.

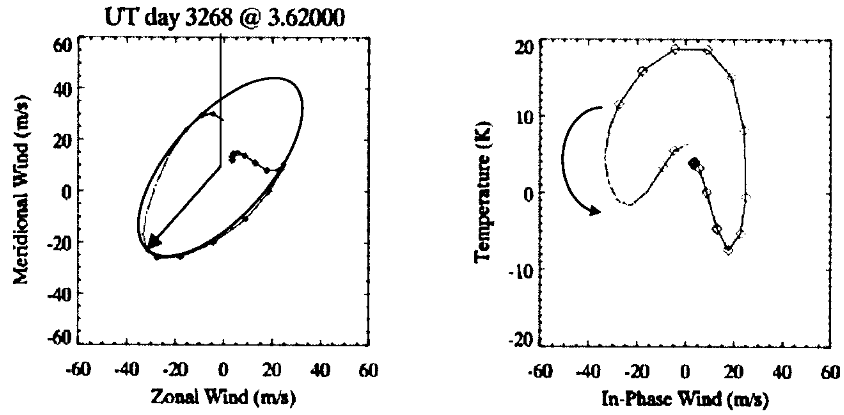

Figure 5.21b Hodographs of zonal wind vs. meridional wind (left panel) and of temperature vs. in-phase wind (right panel) for UT day 268 at 03:37am.

In order to investigate possible atmospheric instability, we need to evaluate the square of Brunt-Vaisala frequency, N^2, and the Richardson number, Ri, for each altitude, defined as:

$$N^2 = \frac{g}{T}\left(\frac{dT}{dz} + \frac{g}{C_p}\right) = \frac{g}{T}\left(\frac{dT}{dz} - \frac{dT_{ada}}{dz}\right) \text{ and } Ri = \frac{N^2}{S^2} \text{ with } S = \sqrt{\left(\frac{du}{dz}\right)^2 + \left(\frac{dv}{dz}\right)^2} \quad (5.3)$$

where - $dT_{ada}/dz = \gamma_d = g/c_p$ is the dry adiabatic lapse rate with g and c_p being, respectively, the gravitational acceleration and per unit mass specific heat at constant pressure. Near 90 km altitude, the adiabatic lapse rate and g are 9.5 K/km and 9.5×10^{-4} kms^{-2}, respectively. The local atmosphere is said to be hydrostatically or convectively unstable if $N^2 < 0$. Simple theory suggests that $Ri > 0.25$ is a necessary condition for dynamic stability [Dutton, 1986].

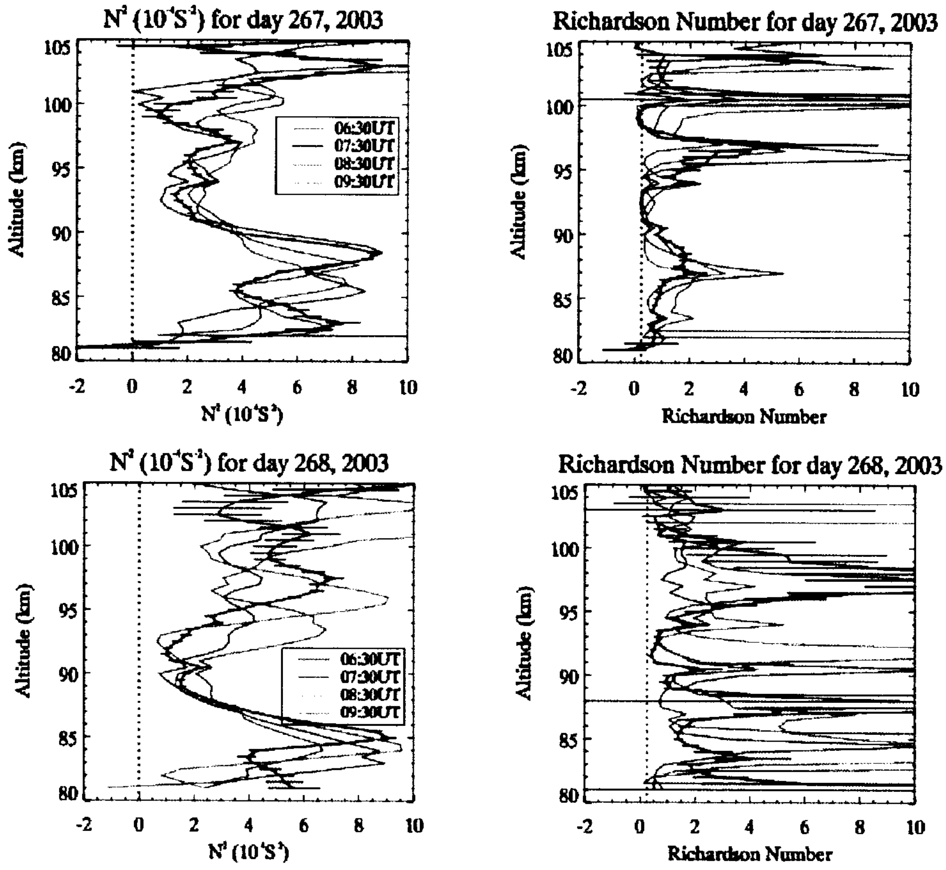

Figure 5.22 Vertical profiles of Brunt-Vasialla frequency square (left panel) and Richardson number (right panel) at UT 06:30, 07:30, 08:30, and 09:30 for both day 267 (top panel) and 268 (bottom panel).

To show that there indeed exists unstable region in both unusual nights of day 267 and 268, we plot the hourly mean vertical profiles of Brunt-Vasialla frequency square and Richardson number at UT 06:30, 07:30, 08:30, and 09:30 in figure 5.22. We clearly see that, in the day 267, the Brunt-Vasialla frequency squares (top left panel) are positive at most altitudes for all four-hour profiles. The Richardson numbers (top right panel) are less than 0.25 at altitude 91-94 km and 98-100 km for both hours 06:30 and 07:30 and at 91-92 km for hour 08:30, and are larger than 0.25 at most of altitudes for hour 09:30. This suggests the atmosphere is convectively stable for most of night, but dynamically unstable in some regions before 09:30UT. The altitude of dynamical instability in 06:30 and 07:30 are corresponding to the altitude we suggested above for the linear critical level between 83 km and 96 km. Similar to day 267, the Brunt-Vasialla frequency squares in day 268 (bottom left panel) are also positive at all the altitudes, suggesting the atmosphere is convectively stable. At the same time, the Richardson numbers are also larger than 0.25 for most altitudes, except near 91.5 km at 07:30UT if taking error bar account, suggesting that the atmosphere is dynamically stable for most of time and altitudes, but dynamically unstable near 91.5 km only at 07:30UT.

5.2.7 Summary

An unprecedented multi-day observation was completed with the upgraded CSU sodium lidar between Sep 18 and October 01, 2003, including a 9-day continuous observation. Spectral analysis of temperature, zonal and meridional winds led to the identification of quasi 1.5-day, 3-day and 5-day waves. These are likely planetary waves, though their origins and characteristics are not presently known. In addition to the tidal periods, the spectral analysis also revealed periods of ~20, ~14 and ~10 hours, which are likely products of nonlinear interactions between tides and planetary wave. Considerable day-to-day variations in diurnal and semidiurnal tidal amplitudes were observed along with a large increase by factors of ~2 in diurnal and semidiurnal amplitudes during days 266-268.

Possible causes for the observed large tidal variability were suggested in relation to planetary wave modulation and gravity wave interactions, revealing the complexity of tidal/planetary wave interaction and tidal/GW interaction. TIME-GCM simulation demonstrated that a Quasi-Stationary Planetary Wave and tidal interactions can introduce strong short term variability to the tides. The temperature, zonal wind, and meridional wind tides (diurnal and semi-diurnal) all increase and decrease rapidly as a result of the interaction. The planetary wave decay also produces an inversion layer between 90 and 100 km at certain longitude, though not as strong as that observed by the lidar. Lidar observed temperature and SABER overpass temperatures over Fort Collins showed very good agreement in both UT day 267 and 268. SABER observation also revealed that the inversion covered over a global region, suggesting the presence of tide/planetary wave interaction. However, we suggested that tide/gravity wave interactions are still needed to account for the more than 2-fold increase in tidal amplitudes.

According to QSPW modeling and gravity wave studies, and local instability (Ri and N^2) analysis for both unusual nights of UTday 267 and 268, both tidal/gravity wave and tidal/planetary wave interactions appear to play a role in the enhancement in tidal amplitudes during both nights. We also found that the heating rate due to breaking of inertial gravity wave is estimated to be less than 2 K/hr [Liu, 2000], which is not enough to account for the dramatic temperature increase in both nights. Unfortunately, the heating rate due to breaking of short period gravity waves (internal gravity waves), which can be much larger locally, can not be observed by sodium lidar at present. Since, as shown in Fig. 5.22, the atmosphere was less stable during the night of 267, it is plausible that the tidal/gravity interactions might possibly make more contribution to tidal amplitude enhancement. Though detailed causes for tidal variability require further study, we have demonstrated that substantial information on MLT dynamics may be obtained from a comprehensive long-period data set.

5.3 Summer quasi-two-day wave activities and tidal day-to-day variability

During August of 2002, 2003, and 2004, three 4-day campaigns of simultaneous observations of temperature, zonal wind, and meridional wind in the mesopause region by our sodium lidar system were completed in UT days 221-224, 2002, days 225-229, 2003, and days 225-229, 2004. In these datasets, we found considerable tidal day-to-day variability along with the significant quasi-two-day wave activities, which can be usually observed in the northern hemisphere with the maximum wave amplitudes near the mesopause in July–August and in the southern hemisphere with corresponding maxima in January–February [Pancheva et al., 2004]. Similar to tidal waves, the quasi-two-day wave is a westward propagating wave with associated zonal wave number three or four. It is believed that the quasi-two day wave is forced by the baroclinic instability of the summer strato-mesospheric jet [Plumb, 1983; Pfister, 1985; Sably, 2001; Sably, 2003]. This instability forces a spectrum of waves with similar phase speeds but differing growth rates that propagate away from the source region. In the Southern Hemisphere, the dominant structure of the wave is a westward propagating pattern of zonal wavenumber 3. However, in the Northern Hemisphere, the zonal wavenumbers observed by longitudinally spaced networks of ground-based radars reported a range between 2 and 5, although the wavenumber 3 structure is still the most significant [Muller and Nelson, 1978; Meek et al., 1996; Thayaparan et al., 1997b]. Satellite analyses have also indicated a westward propagating structure with zonal wavenumbers between 2 and 4 [Lieberman, 1999, 2002]. By combining data from nine meteor and MF (Medium Frequency) radars around the globe, Meek et al. [1996] found a zonal wave number 4 wave in the Northern Hemisphere in 1992. Meanwhile a natural resonance or normal mode of the atmosphere also exists with a wavenumber of 3 and a period near 48 hours, the so called (3, 0) Rossby normal mode. While "true" resonant modes do not exist in the atmosphere due to dissipation, this mode represents a spectral region of enhanced response. The observed quasi-two-day wave period varies between 45 and 55 hours with horizontal winds exceeding 50 m/s in the upper mesosphere (90 km) with the meridional component generally being larger than the zonal component [Meyer, 1998].

The summer quasi-two-day wave is still a very active research topic in recent years. Most investigations thus far employed radar winds and models [Thayaparan et al., 1997; Palo et al., 1999]. Since we fortunately have multiple-day data in August, known to have quasi two-day wave activities, for three consecutive years, 2002, 2003, and 2004, we could compare with satellite data to demonstrate that correlative study between ground-based instrument and space-borne instrument can identify and evaluate the wave features in question. In this section, we will present our lidar observations of quasi-two-day waves, and the comparison with SABER global temperature observations. The tidal day-to-day variability in August for each of the three years, and their possible interaction with quasi-two-day waves will also be discussed. Shown in figure 5.23, 5.24, and 5.25 are the contour plots of temperature (a), zonal wind (b), and meridional wind (c) for August of 2002, August 2003 and August 2004 respectively. A factor of ~5 weaker signal and much higher background around noon, LST, leads to the bare regions above 100 km during these time intervals. Along with the sharper cutoff in Na density near the lower edge of the Na layer, the contours for full diurnal cycle coverage are limited to between 83 and 100 km.

For the August 2002 campaign shown in figure 5.23, the ranges of temperature, zonal wind, and meridional wind are seen to be approximately between (150K, 210K), (−80m/s, 120m/s) and (−90m/s, 90m/s) respectively. While semidiurnal period appears to be stronger in altitudes above ~93 km, oscillations with diurnal period can be seen clearly throughout the region. Both diurnal and semidiurnal oscillations are particularly clear in the meridional wind. Day-to-day variability in the mean-state values, as well as in both diurnal and semidiurnal oscillations clearly exists in all three contours (T, U, V). Downward phase progressions from 100 to 80 km can be seen between day 221 and 222, and again between day 223 and 224 in zonal and meridional wind (less obvious in

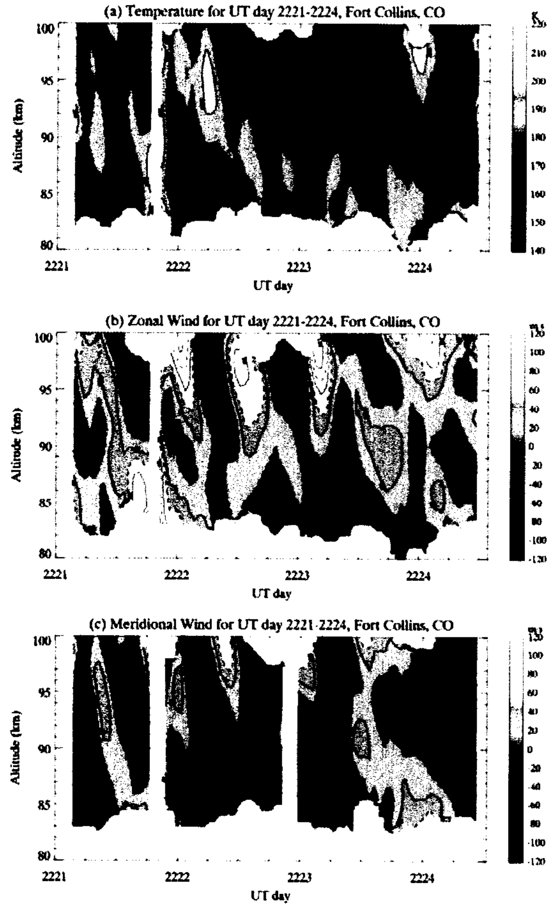

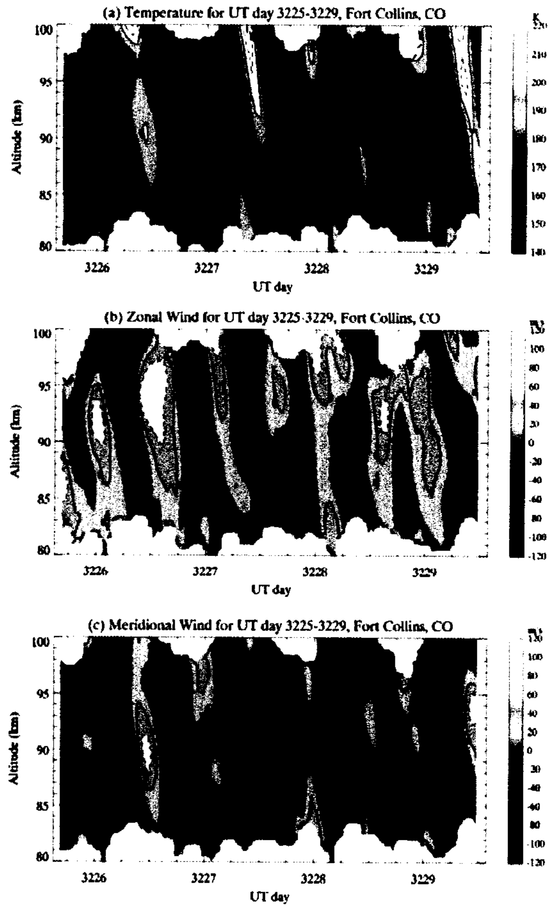

Figure 5.23 Contour plots of temperature (a), zonal wind (b), and meridional wind (c) for August 2002 campaign with resolutions of 2-4km and 1hr.

Figure 5.24 Contour plots of temperature (a), zonal wind (b), and meridional wind (c) for August 2003 with resolutions of 2-4km and 1hr.

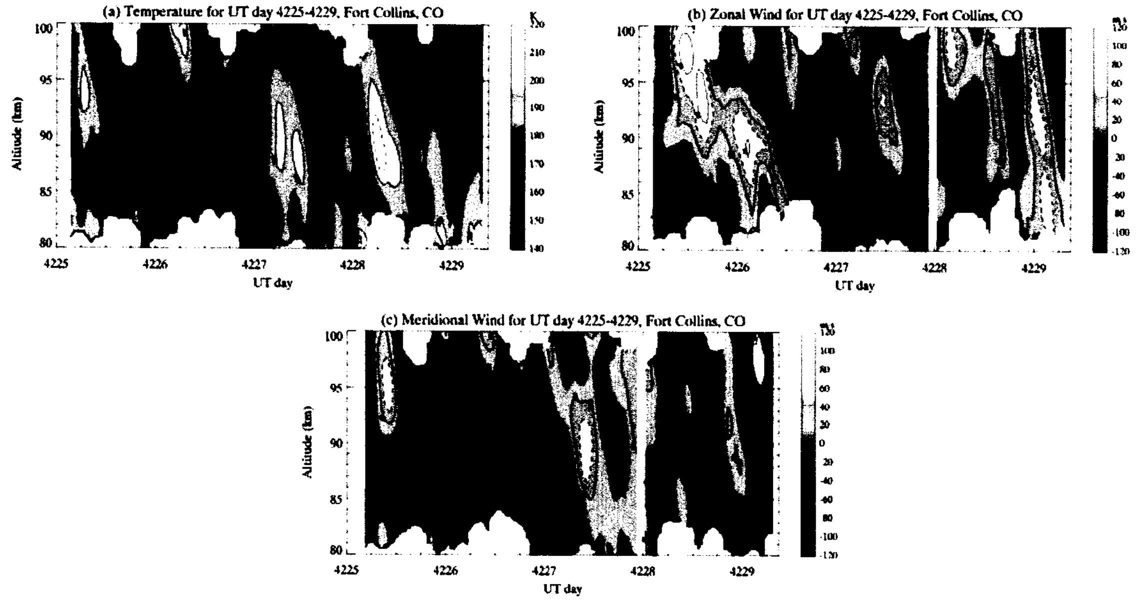

Figure 5.25 Contour plots of temperature (a), zonal wind (b), and meridional wind (c) for August 2004 with resolutions of 2-4km and 1hr.

temperature, but still existent) contours, suggesting the existence of quasi two-day waves. Its relatively smaller phase speed of ~0.8 km/h suggests the presence of interaction between it and atmospheric waves with other periods [She, 2004]. In addition to tidal perturbations, oscillations with other periods shorter than one day also exist. For the August 2003 campaign shown in the figure 5.24, the ranges of temperature, zonal wind, and meridional wind are approximately between (150K, 230K), (-80m/s, 100m/s), and (-100m/s, 80m/s) respectively. Diurnal and semidiurnal oscillations can be seen through the region in all three fields, along with the clear day-to-day variability. Maxima peaks above 90km in temperature contour between day 227 and 228, and again between day 229 and 230, and in zonal wind contour between day 226 and 227, and again between day 228 and 229, clearly indicate the existence of a quasi two-day wave. But it is not very clear in the meridional wind contour. Other periods of perturbations can also be clearly seen in three contours. For the August 2004 campaign shown in figure 5.25, the ranges of temperature, zonal wind, and meridional wind are approximately between (150K, 220K), (-80m/s, 120m/s), and (-120m/s, 100m/s) respectively. Semidiurnal oscillations are stronger throughout the whole region. Maximum winds in the meridional wind contour below 90km suggest the presence of a quasi two-day wave.

5.3.1 Spectrum analysis

By using continuous datasets with vertical resolution of 2-km (4-km) for nighttime (daytime) and temporal resolution of 1hour in UT days 221-224, 2002, UT days 225-229, 2003, and UT days 225-229, 2004, we plot contours of the normalized Lomb periodograms of temperature (top panel), zonal wind (middle panel), and meridional wind (bottom panel) shown in figure 5.26, 5.27, and 5.28 respectively for three campaigns from Lomb powers calculated at periods of 2, 4, 6,...,80 h.

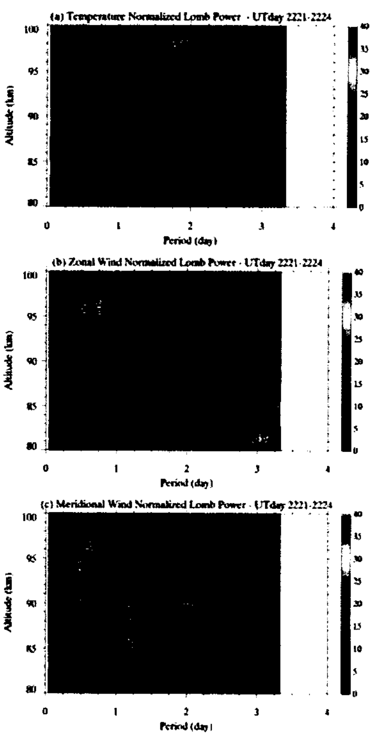

Figure 5.26 Normalized Lomb power contours of temperature (a), zonal wind (b), and meridional wind (c) for UT days 221-224, 2002 are shown with the contour lines corresponding to 1% (white solid line) and 10% (white dot line) probability resulting from random noise.

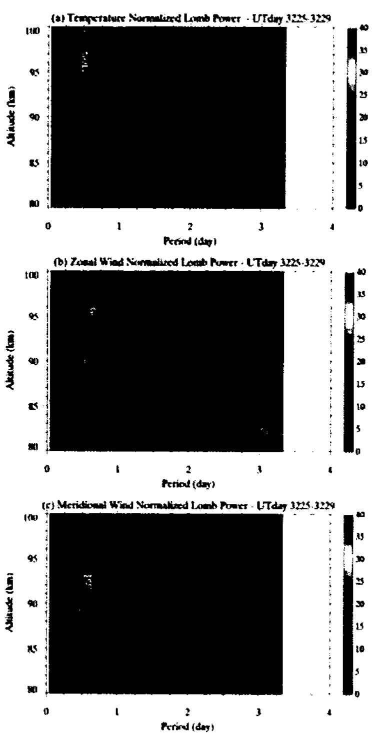

Figure 5.27 Normalized Lomb power contours of temperature (a), zonal wind (b), and meridional wind (c) for UT days 225-229, 2003 are shown with the contour lines corresponding to 1% (white solid line) and 10% (white dot line) probability resulting from random noise.

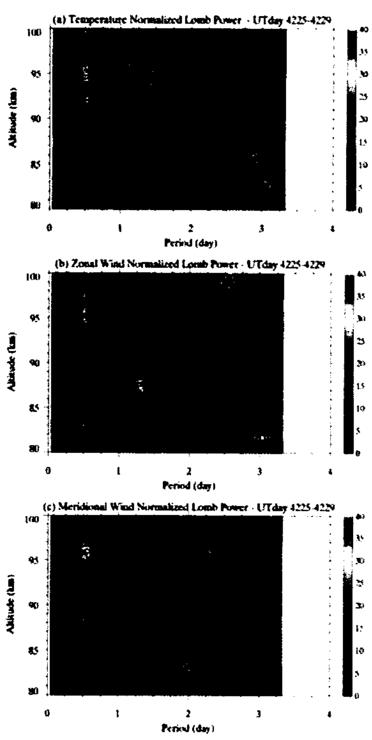

Figure 5.28 Normalized Lomb power contours of temperature (a), zonal wind (b), and meridional wind (c) for UT days 225-229, 2004 are shown with the contour lines corresponding to 1% (white solid line) and 10% (white dot line) probability resulting from random noise.

For UT days 221-224, 2002 shown in figure 5.26, both diurnal and semidiurnal are not seen at all altitudes between 80km and 100km, and also are very weak, especially in the temperature component. The quasi-two-day wave activities are most significant in meridional wind component between 85km and 90km, and less significant in zonal wind component between 86 km and 89 km and in temperature component between 96 km and

98 km. The significant normalized power in zonal component between 82 km and 86 km for 3-day period is possible aliasing due to temporally limited data set. However, for UT days 225-229 in 2003 shown in figure 5.27, both diurnal and semidiurnal are strong above 85 km. In addition, we see a quasi-two-day wave in temperature at 83-85 km, in zonal wind at 87-91 km, and in meridional wind at 85-88 km respectively, and a 1.5-day wave in temperature and zonal wind both at 85-90 km. There also exists power at 9-10 hr period in temperature above 85 km, in zonal wind at 85-95 km, and in meridional wind at 85-92 km respectively, and 14-15 hr period in temperature at 85-95 km, in zonal wind above 83 km, and in meridional wind above 85 km respectively. These are likely the results of nonlinear interactions between tides and planetary waves [She et al., 2004], though the two-day wave activity in 2003 appears to be weaker than those in 2002 and 2004. As shown in figure 5.28 for UT days 225-229, 2004, we saw not only diurnal and semidiurnal oscillations, but also a significant 1.5-day oscillation above 90 km and a quasi two-day wave near 85km in temperature component, a 1.5-day wave between 82 km and 95 km and a quasi-two-day wave near 92 km in zonal wind component, and a quasi-two-day wave below 98 km in meridional wind component.

To reveal the quasi two-day wave activities, the time series of temperature, zonal wind, and meridional wind profiles in 1-hr intervals were filtered by a band-pass filter with sharp cutoffs at 30 and 80 hours. The resulting contours are shown in figures 5.29, 5.30, and 5.31 respectively for UT days 221-224, 2002, UT days 225-229, 2003, and UT days 225-229, 2004.

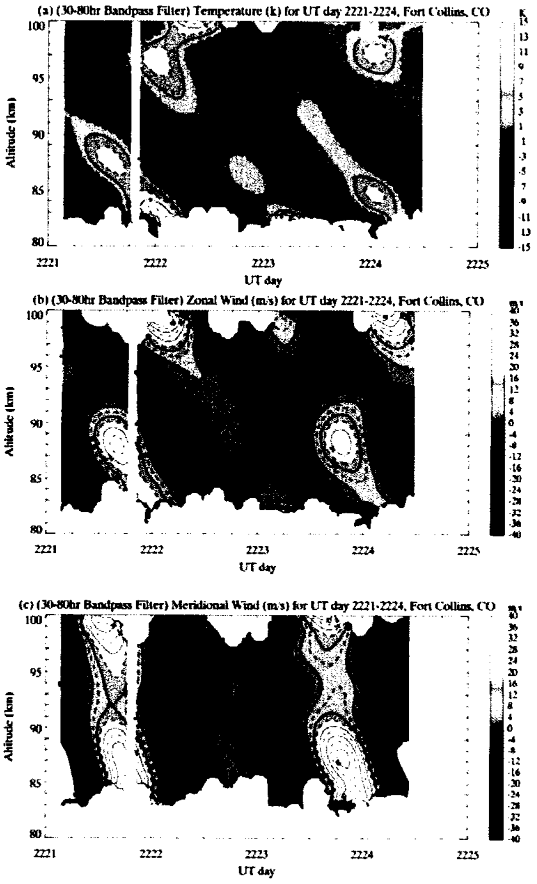

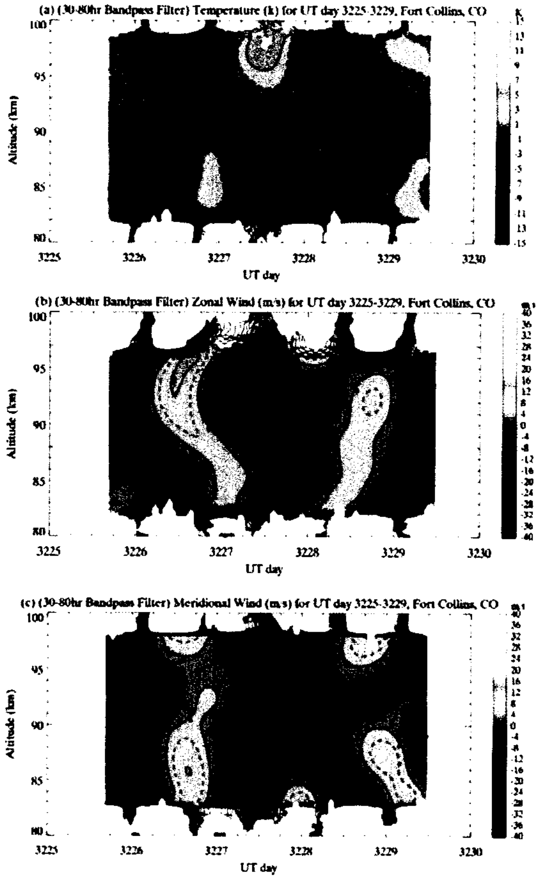

Figure 5.29 Filtered temperature (a), zonal wind (b), and meridional wind (c) contours by a band-pass filter with sharp cutoffs at 30 and 80 hours for UT days 221-224, 2002.

Figure 5.30 Filtered temperature (a), zonal wind (b), and meridional wind (c) contours by a band-pass filter with sharp cutoffs at 30 and 80 hours for UT days 225-229, 2003.

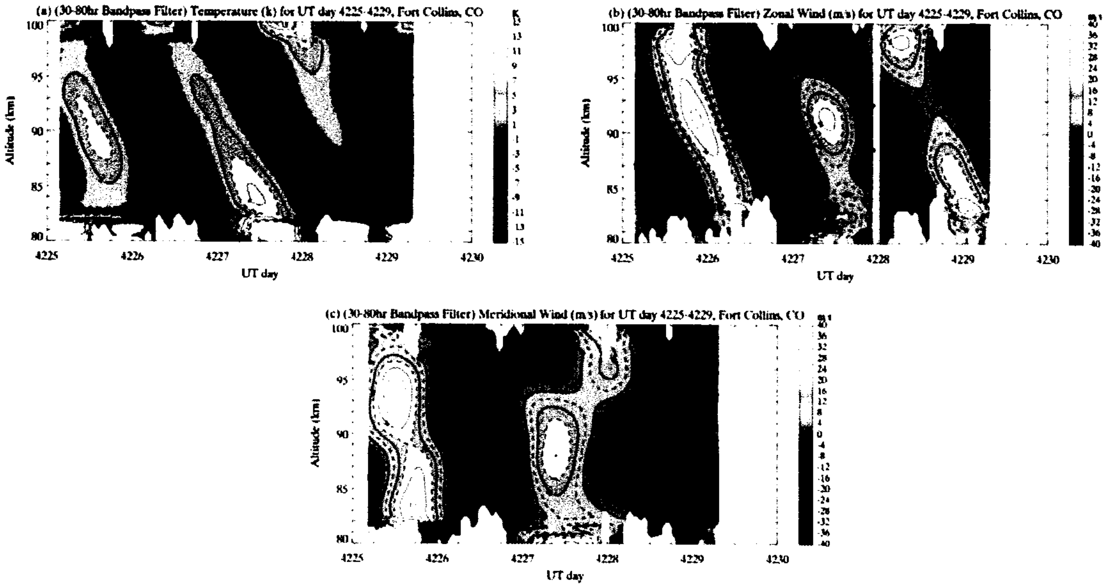

Figure 5.31 Filtered temperature (a), zonal wind (b), and meridional wind (c) contours by a band-pass filter with sharp cutoffs at 30 and 80 hours for UT days 225-229, 2004.

We can clearly see the yellow maxima with two-day separation respectively in temperature below 85 km and above 95 km, in zonal wind below 90 km and above 97 km, and in meridional wind at most altitudes for the dataset in UT day 221-224, 2002 as shown in the figure 5.29. The contour plots for 2003 figure 5.30 look different from both 2002 and 2004, in which no clear downward phase progression was observed. The yellow maxima around 84 km in temperature and around 87 km in meridional wind, as well as both maximum and minimum around 97 km in temperature all appear to be two-day perturbations at a single altitude. The period of zonal wind perturbations were shorter, possibly the result of aliasing from longer-period waves as revealed in the associated Lomb power, shown in figure 5.27(b). Finally, the yellow maxima with two-day separation in meridional wind below 95 km for the dataset in UT day 225-229, 2004 shown in the figure 5.31(c) also suggests the presence of the quasi two-day waves. We note that the downward phase progression in 2003 is not as clear as that in 2002 and 2004, especially among temperature contour plots. In addition, a 1.5 day wave with downward phase progression can also be clearly seen in the temperature and zonal wind components in the figure 5.31(a) and figure 5.31(b). By measuring the vertical phase speed from these two figures, we determine the vertical wavelength of 1.5-day wave to be ~30 km in both temperature and zonal wind components. The 1.5-day wave observed in this campaign behaves differently from that observed in our longest campaign in September 2003, which is discussed in detail in section 5.2. Shown in figure 5.32 is filtered zonal wind contour by a band-pass filter with sharp cutoffs at 30 and 200 hours for September campaign in UT days 261-274, 2003. We clearly see that below 90 km the 1.5-day wave progresses downward with the vertical wavelength of ~25 km which is shorter than that observed in the August 2004 campaign in UT day 225-229. Above 90 km the phase of the wave does not progress downward, and the vertical wavelength of the wave is very large.

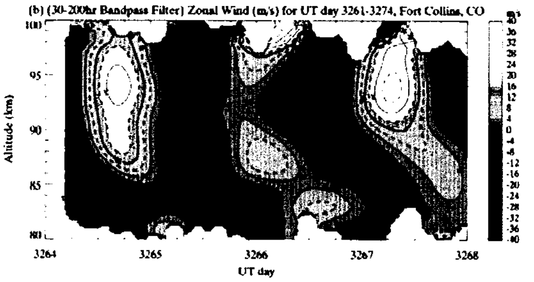

Figure 5.32 Filtered zonal wind contour by a band-pass filter with sharp cutoffs at 30 and 200 hours for September campaign in UT days 261-274, 2003. To clearly show the 1.5-day wave, the contour only presents part of the results between UT days 264 and 268.

5.3.2 Tidal day-to-day variability

The tidal variability in the August 2002 observations was already discussed in detail by She [2004] with the method of day-by-day tidal fitting. Here, we fit the tidal period oscillations with a running 24-hour window. By performing the tidal analyses within the individual 24-hour continuous data sets centered at each hour, we can investigate the variability of diurnal-means, tidal amplitudes and phases much more continuously. Shown in figure 5.33 are the contour plots of the variability in diurnal (a, b, c) and semidiurnal (d, e, f) amplitudes and phases of temperature (a, d), zonal wind (b, e), and meridional wind (c, f) during August 2002 (UT days 221-224) observations. Considerable variability in tidal amplitudes can be clearly seen with magnitudes up to 12 K and 60 m/s for temperature and winds respectively. The semidiurnal amplitudes of both zonal wind and meridional wind are generally small (less than 15 m/s) and less variable between 85 km and 90 km. The diurnal and semidiurnal tidal amplitudes of temperature are both small (less than 8 K) after UT day 2222 with minima which progress downward in the diurnal plot and upward in the semidiurnal plot. This possibly indicates different interaction mechanisms of diurnal and semidiurnal tides with planetary waves. We also note that although the variability in diurnal wind phases is larger in comparison than the corresponding semidiurnal, the altitude-dependent semidiurnal wind phases are robust against interactions.

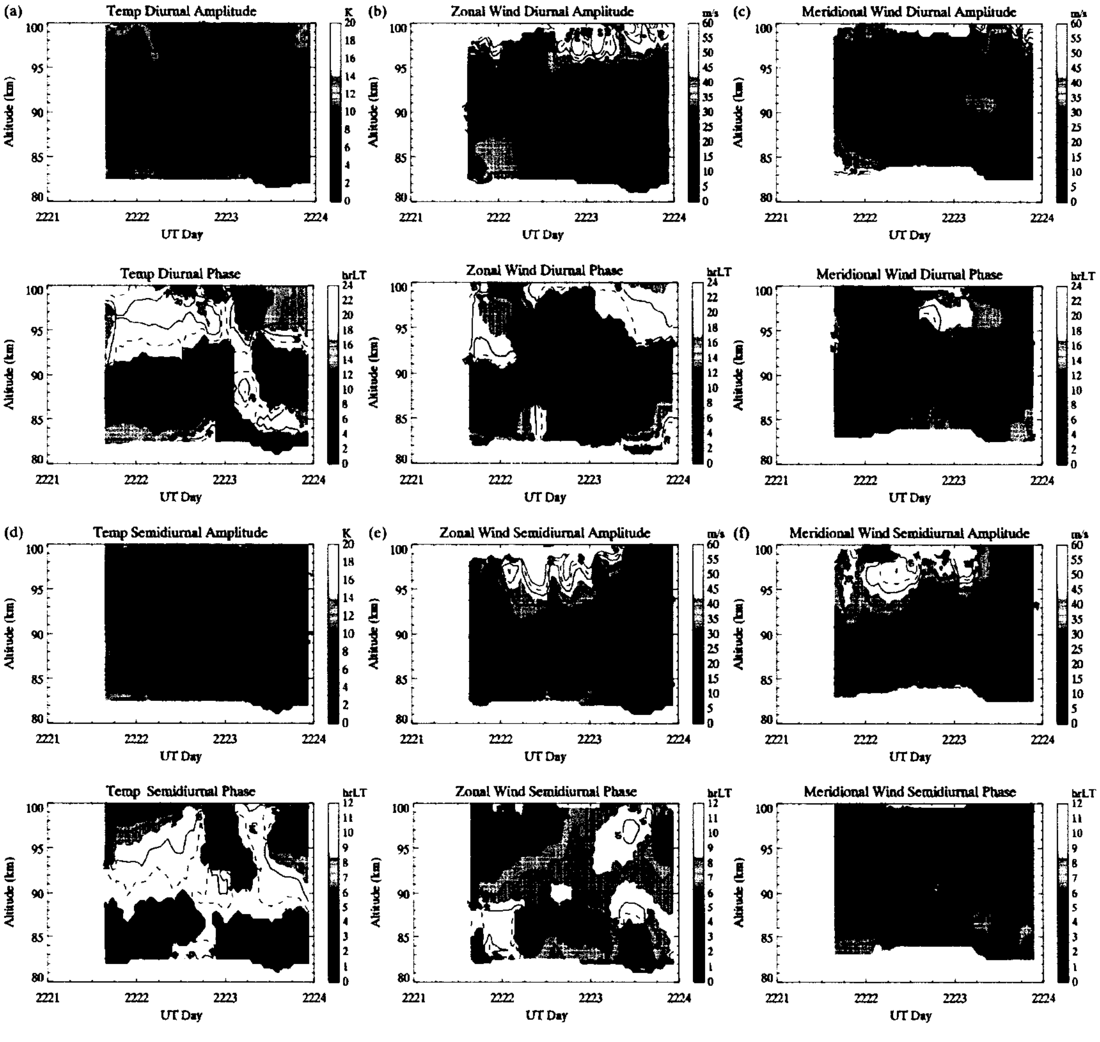

Figure 5.33 Variability in diurnal (a,b,c) and semidiurnal (d,e,f) amplitudes (top) and phases (bottom) of temperature (a,d), zonal wind (b,e), and meridional wind (c,f) during August 2002 (UT days 221-224) observation.

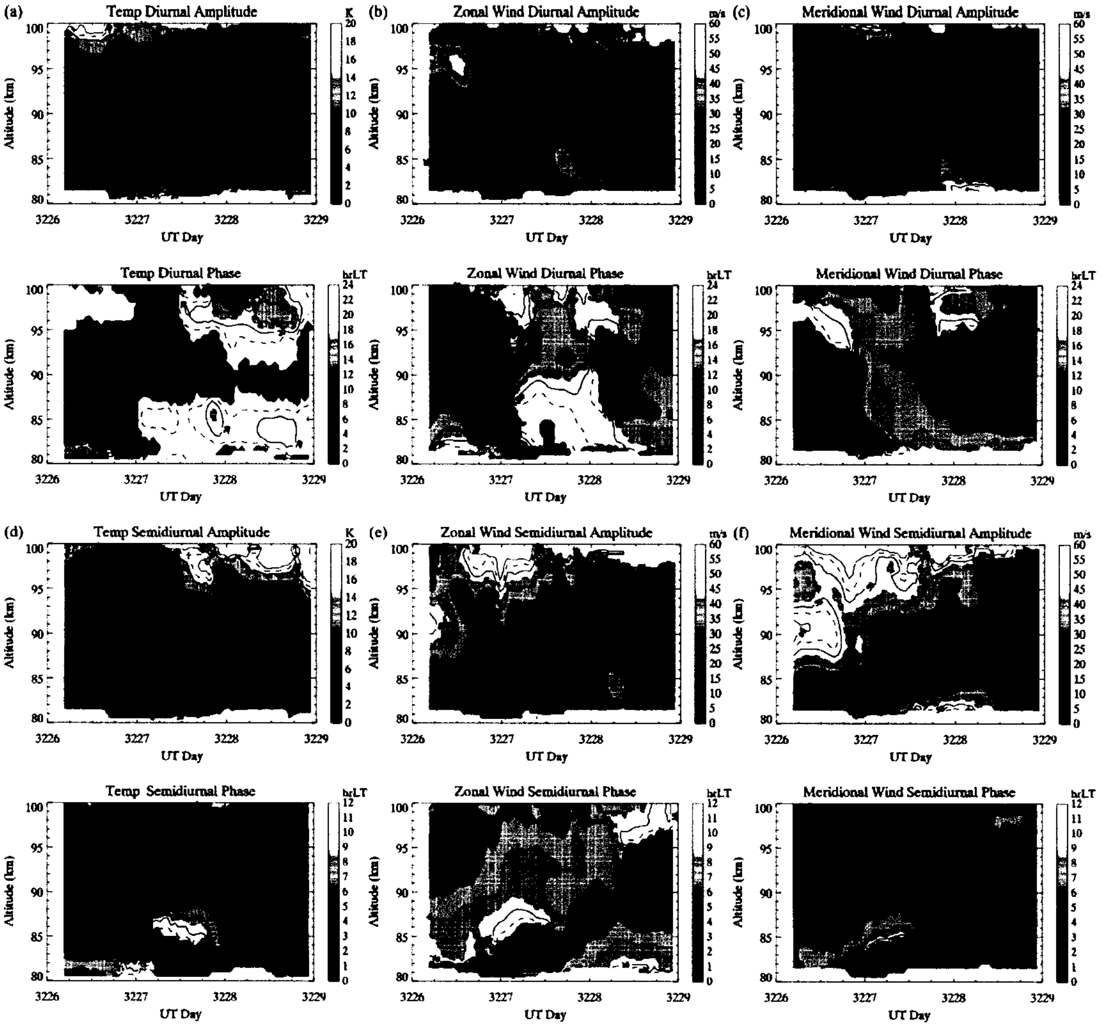

Figure 5.34 Variability in diurnal (a,b,c) and semidiurnal (d,e,f) amplitudes (top) and phases (bottom) of temperature (a,d), zonal wind (b,e), and meridional wind (c,f) during August 2003 (UT days 225-229) observation.

Similar to figure 5.33, we plot the contours of tidal variability during August 2003 observations (UT days 225-229) which are shown in figure 5.34. Again like the August 2002 dataset, we see tidal day-to-day variability in all three fields with amplitudes varying up to 20 K and 60 m/s for temperature and winds respectively. The variability in the zonal wind diurnal and semidiurnal amplitudes, and the meridional wind semidiurnal amplitude can be seen but with unclear signature. In the zonal wind diurnal amplitude plot, one observes a downward progression, while the upward progression is clearly seen in the semidiurnal amplitudes of both zonal and meridional components. The diurnal and semidiurnal phases in temperature, zonal wind, and meridional wind are constant within 2 hours at each altitude for the whole campaign. The semidiurnal phases of zonal and meridional wind components follow each other very well with an approximate ~3 hour difference in accordance with the polarization relation of tides and gravity waves.

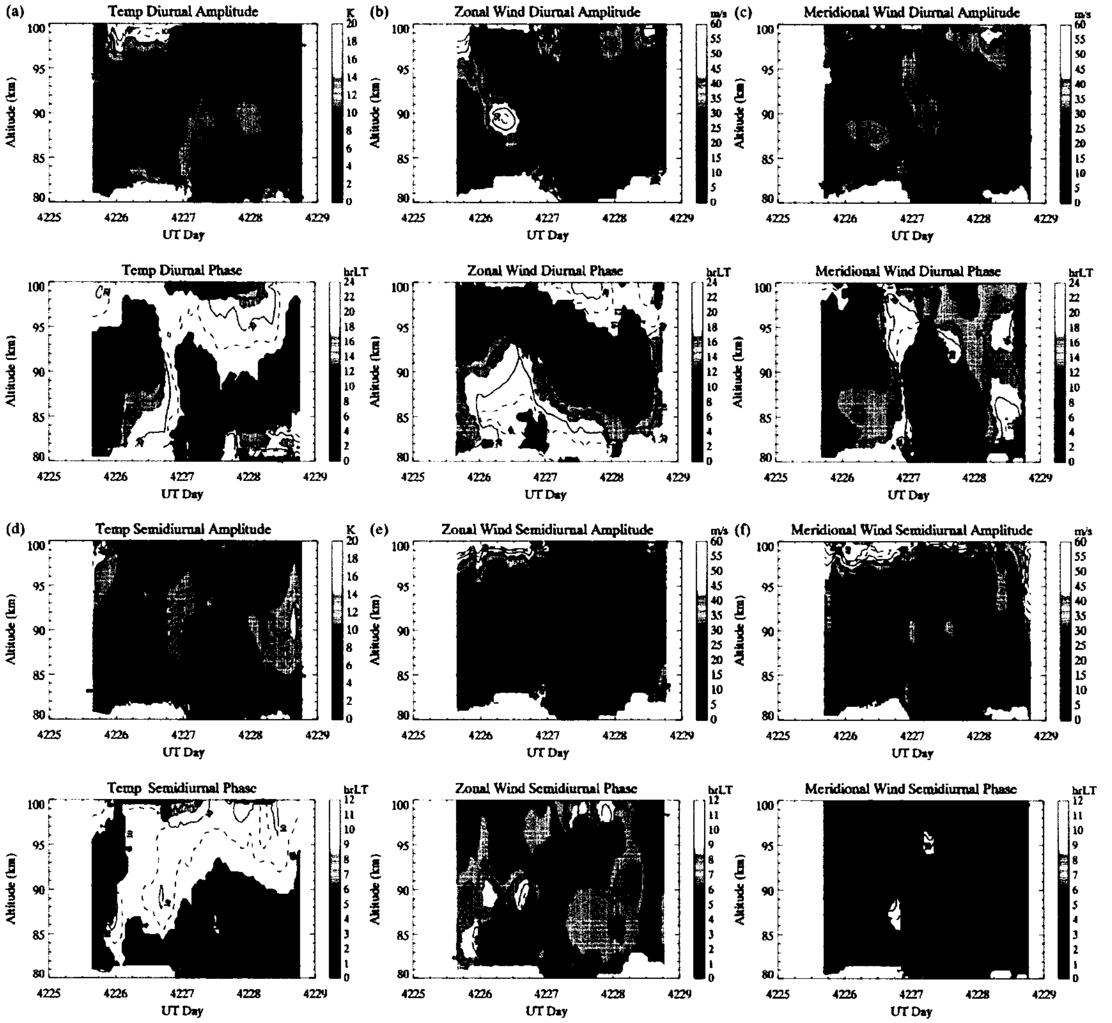

Figure 5.35 Variability in diurnal (a,b,c) and semidiurnal (d,e,f) amplitudes (top) and phases (bottom) of temperature (a,d), zonal wind (b,e), and meridional wind (c,f) during August 2004 (UT days 225-229) observation.

Shown in figure 5.35 are the contours of tidal variability during August 2004 observations (UT days 225-229). We could see considerable day-to-day variability of diurnal and semidiurnal amplitudes. The diurnal amplitude contour of temperature in figure 5.35(a) shows the yellow maxima propagating upward with a speed of ~8 km/day, whereas the diurnal amplitude contour of zonal wind in figure 5.35(b) shows that the yellow maxima propagating downward with a speed of ~12 km/day. The different behaviors of tidal variability between temperature and wind can be also seen in our other lidar datasets.

Compared to the September 2003 campaign, the variability of the apparent tidal amplitudes and phases in the August of 2002, 2003, and 2004 is more difficult to analyze. We believe this is due to shorter observation period and smaller signal-to-noise ratio; and interactions with 2-day wave or the planetary waves with other periods on global scales or interactions with gravity waves, or combination of both.

5.3.3 Comparisons of the quasi-two-day wave between Lidar and SABER

Since we observed significant two-day wave activities in August in all three years, we compare our results with those of satellite observations, e.g. TIMED/SABER temperatures for validation and global perspectives. Shown in figure 5.36 are the amplitudes and phases of quasi-two-day wave in temperature, zonal wind, and meridional wind components observed by our lidar at Fort Collins, CO during summer 2002 campaign from UT days 221 to 224. We obtained these profiles by including a 48-hour harmonic term in our tidal analysis. The results shown in Fig. 5.36 are meaningful, as the result of tidal-period oscillations remains basically the same with or without including the 2-day term. We can see that the temperature amplitudes of the quasi-two-day wave are generally around 5K, but can be as large as 8K near 87 km and 97km. Zonal wind amplitudes slightly decrease with increasing altitude below 93km, but remain around 10m/s. The meridional wind amplitude near 90 km is ~35 m/s, three times larger than its zonal wind counterpart. The stronger amplitude of the quasi-two-day wave in the meridional wind component is consistent with previous observations [Meyer, 1998]. Above 95 km, both zonal wind amplitude and meridional wind amplitude increase exponentially with altitude. This is likely due to the exponential decrease of air density and conservation of wave energy. In the meantime, as shown in the phase plots, we can see that the time of maximum zonal wind and meridional wind occurred at earlier times at the higher altitudes, implying a downward phase progression and upward energy propagation. But temperature phase is more like the upward progression. The observed vertical wavelength of quasi-two-day wave is ~120 km estimated by the rate of change of the phase with height between 83 km and 93 km in meridional wind component. The long vertical wavelength observed is consistent with previous radar observations of the quasi-two-day wave by Thayaparan et al. [1997] with vertical wavelength of ~150km and indicative of a near resonant response. The phase plots also show that the meridional component leads the zonal component by ~5-8h at the most altitudes, indicating clockwise rotation of the wind vector (looking from above). However, the radar observations show that the meridional component leads the zonal component by 11-14hr, which is near quadrature relation [Thayaparan et al., 1997]. This is not consistent with our lidar observed relation.

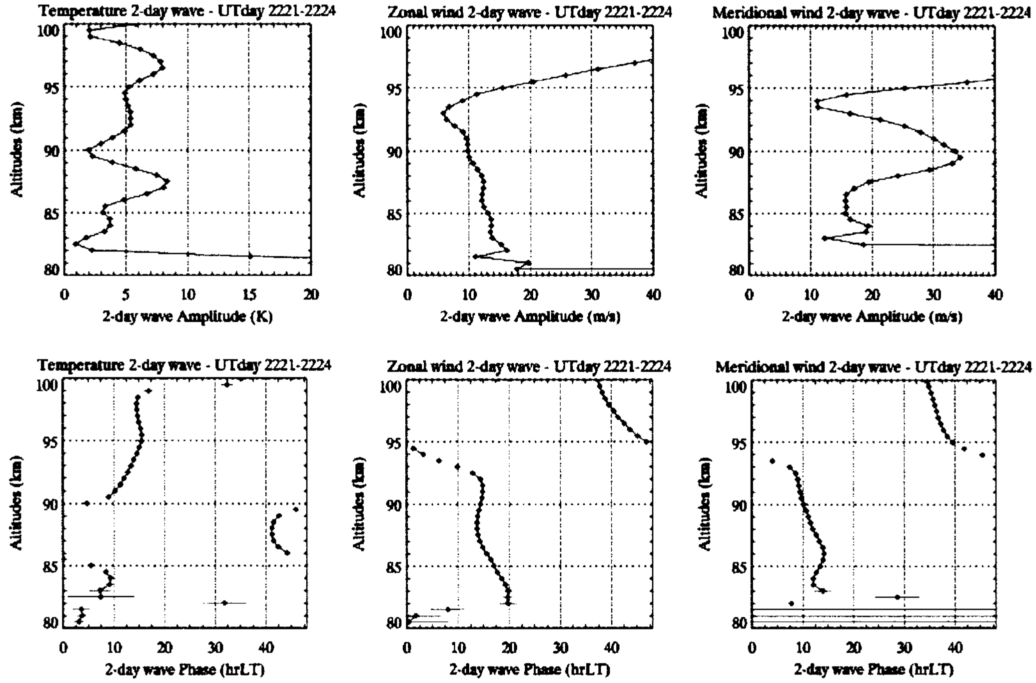

Figure 5.36 Amplitudes (top panel) and phases (bottom panel) of quasi-two-day wave in temperature (left column), zonal wind (middle column), and meridional wind (right column) components observed by our lidar system at Fort Collins, CO during summer 2002 campaign from UT days 221 to 224.

To compare with the quasi-two-day wave observed by SABER, we collaborated with Dr. Scott Palo's group at the University of Colorado. They performed the quasi-two-day analysis on SABER temperature by using a global least-square fitting in time and space for zonal wavenumber 3 and 4 waves. Shown in figure 5.37 are the amplitude contours (blue-2K, light blue-4K, green-6K, yellow-8K) of quasi-two-day waves for both wavenumber 3 (upper) and 4 (bottom) observed by SABER for UT day 221-224, 2002. The two perpendicular red lines marked the latitude of our lidar facility (40.5°N) and the altitude of sodium density peak (91 km). We can clearly see that the wavenumber 4 wave is the most dominant wave and much stronger than the wavenumber 3 wave during the lidar campaign in August 2002. The SABER observed temperature ~6 K amplitude of wavenumber 4 quasi-two-day wave is comparable to that observed by our lidar system. Further, the amplitude of wavenumber 4 wave decreases from ~6 K in day 221 to ~3 K in day 224. The decrease of wave amplitude with time is also observed by our lidar system. As shown in figure 5.29 (data analysis by using 30-80 bandpass filter), the yellow maxima between days 221 and 222 and the blue minima just before are stronger than those between days 223 and 224, indicating the decreasing amplitude of quasi-two-day wave in consistent with the intermittent nature of the quasi-two-day waves.

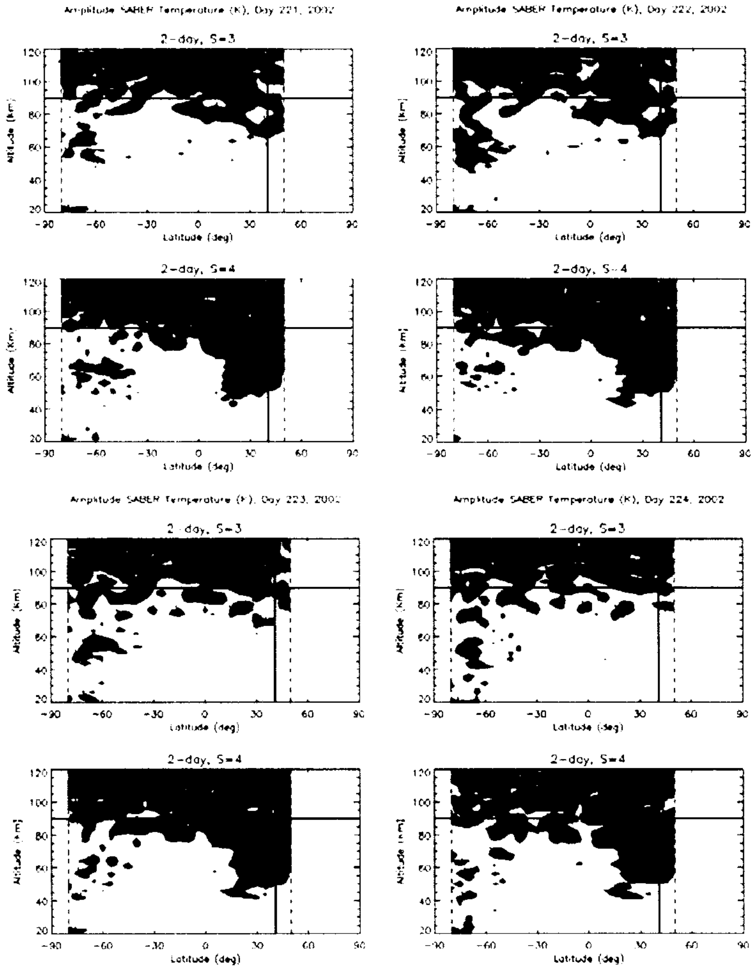

Figure 5.37 Two-day wave amplitudes of SABER temperature obtained by using a linear least squares fit to a wave propagating in time with 48hr and space with both zonal wavenumber -3 and -4 during UT days 221-224, 2002.

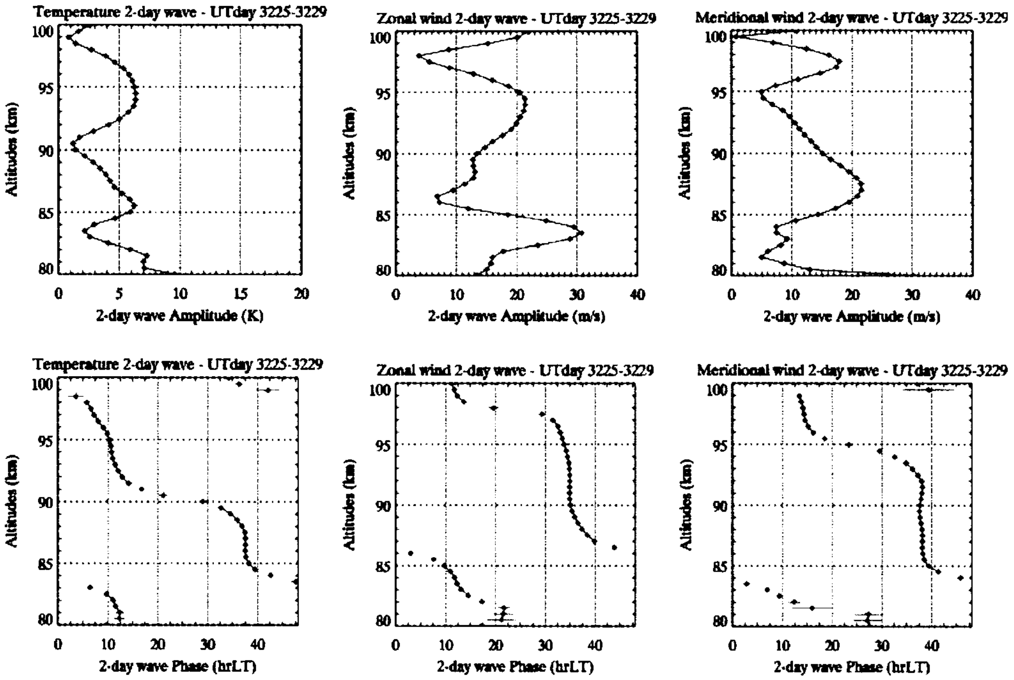

Figure 5.38 Amplitudes (top panel) and phases (bottom panel) of quasi-two-day wave in temperature (left column), zonal wind (middle column), and meridional wind (right column) components observed by our lidar system at Fort Collins, CO during summer 2003 campaign from UT days 225 to 229.

Figure 5.38 shows the amplitudes and phases of quasi-two-day wave in temperature, zonal wind, and meridional wind components observed by sodium lidar during summer 2003 campaign from UT days 225 to 229. The amplitudes of quasi-two-day wave with less than 5K in temperature and 10-15m/s for meridional wind, are generally smaller than those observed in the summer 2002 campaign shown in figure 5.36, except that zonal wind amplitude could be as large as ~30 m/s near 83km and ~20m/s near 95km. The weaker temperature amplitude can also be seen in filtered temperature contours of figure 5.30(a), which is dominated by a 1.5-day wave. The downward phase progression of quasi-two-day wave could be clearly seen in all three components. The observed vertical wavelength of quasi-two-day wave is ~300 km (near evanescent) estimated by the rate of change in meridional wind phase plot between 85 and 92km where the wave amplitude is stronger enough to minimize the aliasing. The much longer wavelength than that observed in August 2002 suggests that the quasi-two-day wave observed in August 2003 was likely a trapped wave. However, the vertical wavelength in temperature component is much shorter than that in wind components. The different vertical wavelength in wind and temperature can be observed in the diurnal tide by our lidar system, such as the diurnal tide observed in our 9-day continuous dataset in Sept. 2003 shown in figure 5.2a. Shown in figure 5.39 are the temperature amplitudes of quasi-two-day wave observed by SABER in days 225 and 229. As shown, temperature amplitudes are very small for both wavenumber 3 and wavenumber 4 waves between 80 km and 100 km.

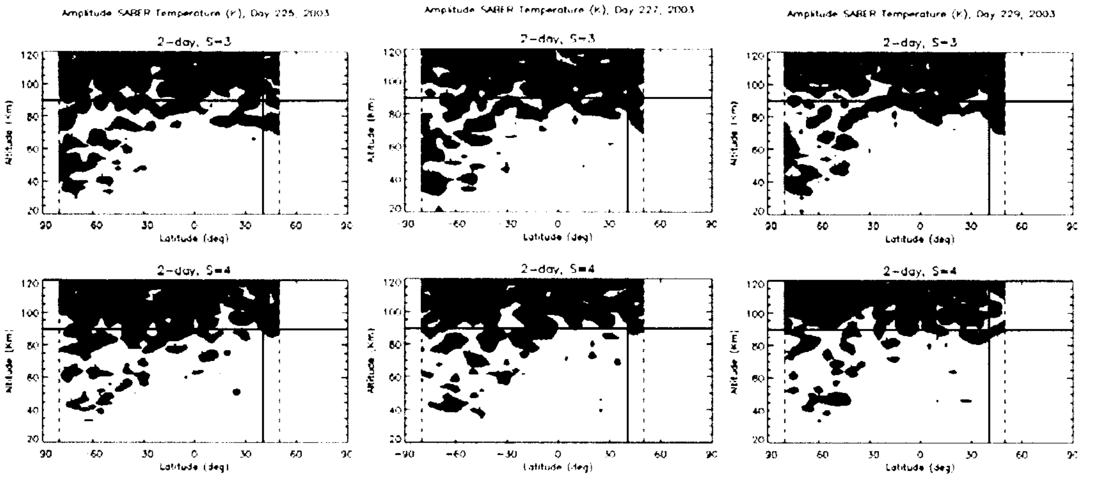

Figure 5.39 Two-day wave amplitudes of SABER temperature obtained by using a linear least squares fit to a wave propagating in time with 48hr and space with both zonal wavenumber -3 and -4 for UT day 225, 227, and 229, 2003.

Similar to figures 5.36 and 5.38, we plot the amplitudes and phases of quasi-two-day wave in temperature, zonal wind, and meridional wind components observed by the CSU lidar system during the summer 2004 campaign from UT days 225 to 229 in figure 5.40 and two-day wave amplitudes of SABER temperature for UT days 225, 227, and 229, 2004 in figure 5.41.

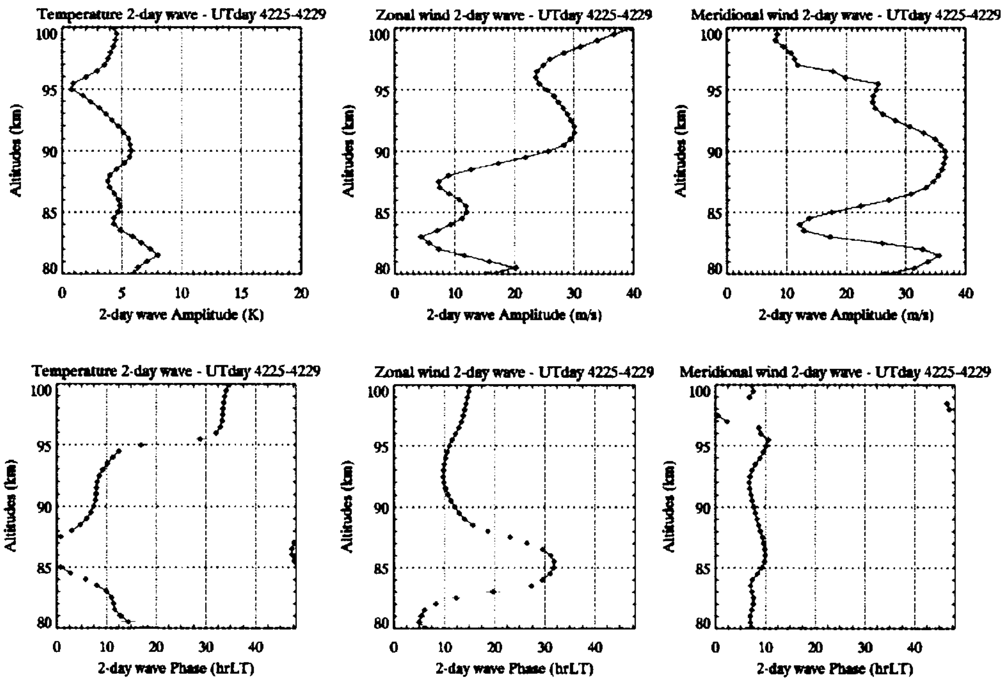

Figure 5.40 Amplitudes (top panel) and phases (bottom panel) of quasi-two-day wave in temperature (left column), zonal wind (middle column), and meridional wind (right column) components observed by our lidar system at Fort Collins, CO during summer 2004 campaign from UT days 225 to 229.

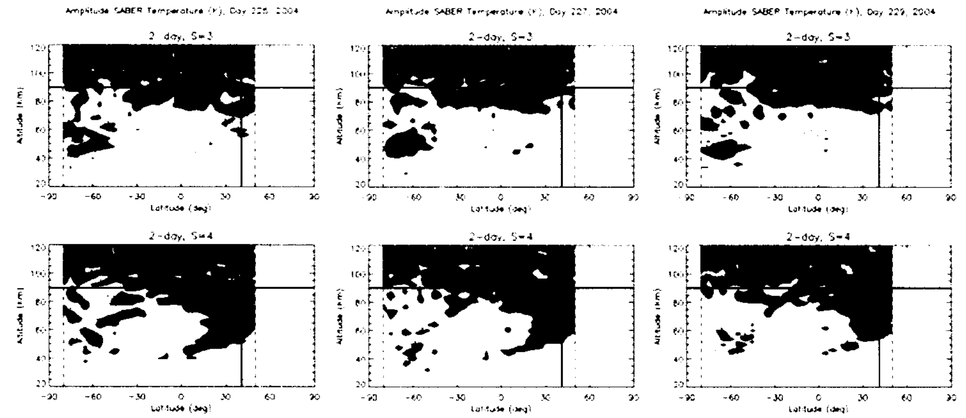

Figure 5.41 Two-day wave amplitudes of SABER temperature obtained by using a linear least squares fit to a wave propagating in time with 48hr and space with both zonal wavenumber -3 and -4 for UT days 225, 227, and 229, 2004.

As shown in figure 5.40, the lidar observed temperature amplitude of quasi-two-day wave is around 5K below 90km and less than 5K above 90km with a minimum of 1K near 95km, whereas the meridional wind amplitude is as large as ~37m/s near 90km, which is comparable to that observed in August 2002 (~35m/s near 90km) and stronger than that observed in August 2003 (~20m/s near 88km), and above 90km the amplitude decreases dramatically with a rate of ~3.5m/s/km. Meanwhile, the meridional wind phase plot shows that the wave phase is still progressing downward in some altitude range, such as 85-93km, with a vertical wavelength of ~160km, longer than that observed in August 2002 and shorter than that observed in August 2003. However, it is difficult to explain what happened in the temperature phase plot. The 2-day wave amplitude of zonal wind could become as large as 30 m/s near 92km, whereas below 90 km the amplitude of zonal wind decreases to ~10 m/s. The contour plots of the temperature amplitude of quasi-two-day wave observed by SABER in figure 5.41 show that the most dominant wave is the wavenumber 4 wave, which is the same as that observed in August 2002. The amplitude of wavenumber 4 wave is ~4 K below 90 km and 1-2 K above 90 km, which is comparable to temperature amplitude observed by lidar. As seen, the wave amplitude decreases from day 225 to day 229.

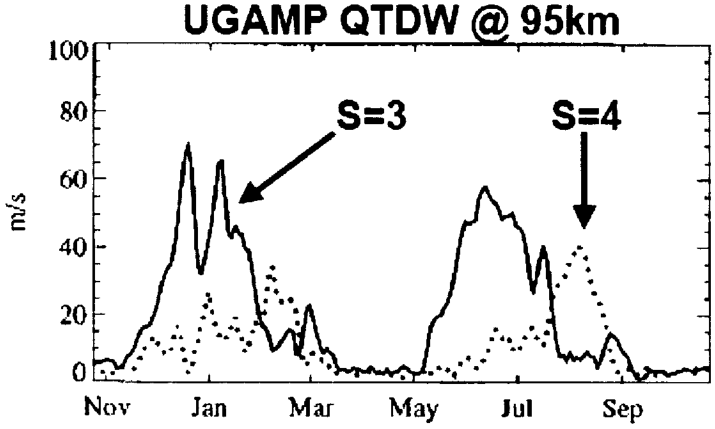

Figure 5.42 Annual evolution of the quasi-two-day wave in the meridional wind field as seen by the UGAMP general circulation model on the equator at 95km. (Taken from Norton and Thuburn [1996])

Shown in figure 5.42 is the annual evolution of the quasi-two-day wave in the meridional wind field as seen by the UGAMP (UK Universities Global Atmospheric Modeling Programme) general circulation model on the equator at 95km. In February and August wavenumber 4 component becomes the dominant wave following the rapidly decreasing of wavenumber 3 component. The model captured the amplification of the quasi-two-day wave in both the northern and southern summers. Although the largest peaks occur for a zonal wavenumber of 3, some wavenumber 4 component is also seen.

In the year 2002, the temperature amplitude of quasi-two-day wave for wavenumber 4 observed by SABER in the middle latitude of the northern hemisphere has the maximum peak of 6-8K in late July and early August, then decreases rapidly to less than 2K within 8 days at a rate of ~0.7 K/day. In the year 2004, the temperature amplitude peak of quasi-two-day wave for wavenumber 4 observed by SABER in the middle latitude of the northern hemisphere occurred in August 8 and 9, and then decreased dramatically from 6-8K to less than 2K in August 20 with a decreasing rate of ~0.5K/day, which is slightly slower than that in 2002. However, in the year 2003, the temperature amplitudes of quasi-two-day waves for both wavenumber 3 and 4 as observed by both lidar and SABER are weak (less than 2K). All these phenomena suggest the consistency between observation and UGAMP model [Palo, private communication]. Comparisons of quasi-two-day wave events observed by SABER and lidar for all three years, 2002, 2003, and 2004 in August, also indicates the possible the modulation by Quasi-Biannual Oscillation (QBO) on the quasi-two-day wave amplitude.

5.3.4 Summary

During three 80-hour campaigns respectively in UT days 221-224, 2002, days 225-229, 2003, and days 225-229, 2004, considerable tidal day-to-day variability and the significant quasi-two-day wave activities were observed by the CSU sodium lidar system at Fort Collins, CO.

Comparisons between the quasi-two-day wave amplitudes of temperature observed by lidar and SABER for all three campaigns show very good agreement. The decreasing amplitudes of quasi-two-day wave observed by both lidar and SABER are consistent with UGAMP-GCM model prediction.

The quasi-two-day wave observed by both SABER and lidar in August of years 2002, 2003, and 2004 with wave amplitude in August 2003 weaker than that in August of 2002 and 2004 indicates the possible the modulation by the Quasi-Biannual Oscillation (QBO) on the quasi-two-day wave amplitude.

5.4 Winter mesospheric inversion layer and tidal day-to-day variability

Mesospheric inversion layer (MIL), with temperature warming above a positive lapse rate in the bottom portion of the temperature profiles, is an interesting but poorly understood feature in the mesosphere and lower thermosphere (MLT) region. The MIL was first discovered in falling sphere observations, reported by Schmidlin [1976]. Since 1980's, the MIL phenomena have been frequently observed by lidar instruments, including Rayleigh lidar [Hauchemcorne et al., 1987], and Na temperature lidar [She et al., 1990; She et al., 1993; Bills and Gardner, 1993; States and Gardner, 1998], along with falling spheres [Schmidlin, 1976; Lubken et al., 1994] launched by rockets. The MIL with observed amplitude typically ranging from 10K to 35K is a persistent feature of the winter thermal structure around 70 km. Since the winter inversions were mostly observed at night, there were suspicions that these features may be simply a manifestation of tidal phase at night, not true thermal inversion. These MILs generally propagate downward with phase speeds comparable to tidal phase speeds. When the same data are averaged over a diurnal cycle (24 hours) to determine the mean temperature profiles, a MIL may no longer be seen in the averaged temperature profiles [Meriwether and Gardner, 2000]. Although the physical mechanism to produce the temperature inversion layer is not yet well understood, it was believed that the gravity wave interaction with tides plays an important role in the development of the inversion layer [Meriwether et al., 1998; Liu and Hagan, 1998]. Earlier, the inversion layer was believed to be caused by turbulence heating layer due to the breaking of high frequency gravity waves accompanied by dynamic cooling on the top side of the layer [Hauchecorne et al., 1987; Whiteway et al., 1995]. The simulation done by Waterscheid and Schubert [1990] showed that the breaking of a gravity wave with 300km horizontal scale could introduce a significant cooling effect, as much as ~30K. More recently, using a numerical simulation with the Whole Atmosphere Community Climate Model (WACCM), Sassi et al. [2002] have shown that "the occurrence of wintertime inversions is a direct consequence of the rapid decay with height of vertically propagating planetary waves, which induces large temperature perturbations in the upper mesosphere to maintain hydrostatic equilibrium". They also demonstrated that gravity waves play an essential indirect role, setting up a critical line in the upper mesosphere where Rossby waves break in the mesospheric surf zone. Using UARS data to provide global perspective with concurrent Rayleigh lidar observations, Salby et al. [2002] showed that both UARS and a numerical simulation with a 3-D model reveal an extensive pattern of inverted thermal structure. "The behavior is closely related to planetary waves, which, in the model, experience strong absorption in the upper mesosphere and lower thermosphere. Inverted thermal structure mirrors the synoptic pattern of potential vorticity, which marks the polar night vortex. Both are strongly distorted during stratospheric warmings, when inverted thermal structure at midlatitudes is favored." That the propagation of a transient quasi-stationary planetary wave (QSPW) can affect tidal amplitude and lead to temperature inversion in the MLT region, has been demonstrated with September TIME-GCM simulation and results were discussed in section 5.2.5.

In this section, we will report a temperature inversion layer observed by our sodium lidar system over Fort Collins, CO in the December 2004 campaign. The peak of this inversion layer persisted near 85km for most of night in UT day 338, 2004. This special event is very interesting due to its difference from those reported in the literatures. Along with the discussion on the mesospheric temperature inversion layer and the possible reason for its formation, we will also discuss tidal day-to-day variability observed and its possible relations with the MIL.

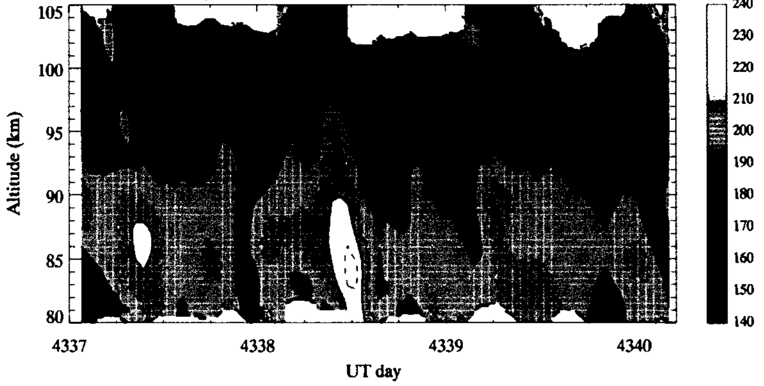
(a) Temperature for UT day 4337-4340, Fort Collins, CO

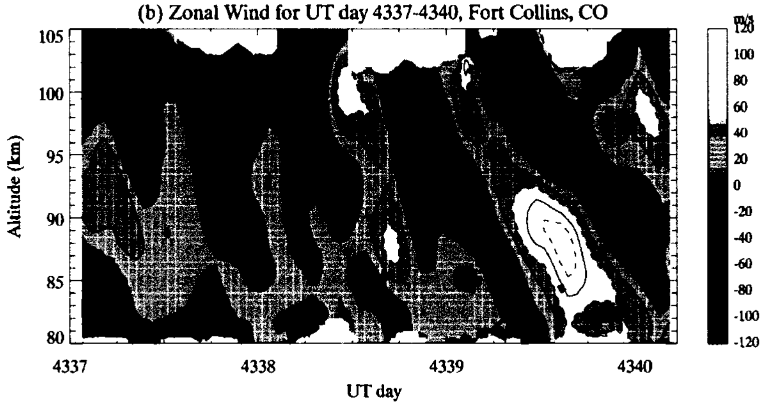
(b) Zonal Wind for UT day 4337-4340, Fort Collins, CO

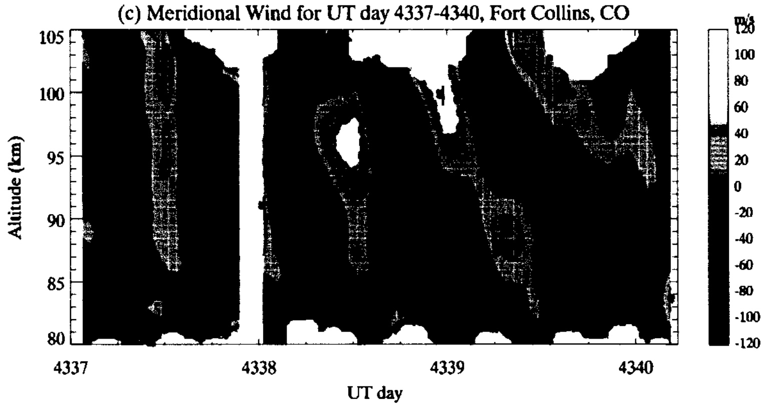
(c) Meridional Wind for UT day 4337-4340, Fort Collins, CO

Figure 5.43 Contour plots of temperature (a), zonal wind (b), and meridional wind (c) observed by our sodium lidar at Fort Collins, CO in December 2004 campaign.

Shown in the figure 5.43 are the contour plots of temperature, zonal wind, and meridional wind simultaneously observed by CSU sodium lidar system in December 2004 winter campaign. The temporal and vertical resolutions of the dataset are 1hour and 2 km (4 km) for nighttime (daytime) respectively. We can clearly see in the temperature contour plot that the strong temperature inversion started from the beginning of UT day 338 at 85-90 km with progressively increased amplitude and finally became a large amplitude anomaly at about 12:00UT extending to a larger altitude region between 80km and 100km. At the same time when the temperature bump is formed, both zonal wind and meridional wind as well as wind shear above 90 km increased dramatically. It is interesting to note that an inversion at ~86 km also existed in the nighttime hours of day 337. In addition, the contour plots also show the diurnal and semidiurnal oscillations with considerable variability. The yellow amplitude maxima at zonal wind component between 90 and 100km indicate the presence of a quasi 1.5-day wave. Unlike the downward phase progression, the significance of the upward phase propagation, also evident in Fig. 5.24, is not yet clear. Furthermore, we also observed a strong zonal wind exceeding ~120m/s at near 85-90km in the daytime of day 339.

5.4.1 Temperature inversion layer observed by sodium lidar

On the night of UT day 338, 2004, a temperature inversion layer near 85 km lasting for most of the night without clear downward phase progression was observed before 09:30UT by our sodium lidar system over Fort Collins, CO. Shown in figure 5.44 is the time series of temperature vertical profiles. For clarity, the vertical profiles are shifted ~8 K for every hour. The temperature inversion layer near 85 km persisted for most of the night and gradually increased in amplitude, as marked by the horizontal light blue dashed line in figure 5.44 of hourly mean temperature profiles. The strongest inversion layer with amplitude of ~50 K and altitude extended from 80 to 100 km can be clearly seen in the temperature vertical profile at 09:30UT highlighted in black solid line. To compare this profile with its neighboring vertical profiles, we re-plotted the profiles from 8:30 to 11:30 UT in figure 5.46(a). As shown, we can see that the temperature inversion layer starts to move downward after 09:30UT. At the same time, the temperature at 10:30UT near 85km is ~15K warmer than that at 09:30UT. Since sodium layer became very weak near 80km, the signal-to-noise ratio is low below 80 km. The decreasing temperature below 80km in the 10:30UT profile could be continuous, implicating a larger temperature inversion. The downward phase progression from 10:30UT suggests that the added inversion may be induced by tides. Above 95 km, we note that temperature gradients for all the profiles approach adiabatic lapse rate of ~9.5K/km. This is consistent with the presence of gravity wave interaction with mean and/or tidal wind as discussed in Section 5.2.6.

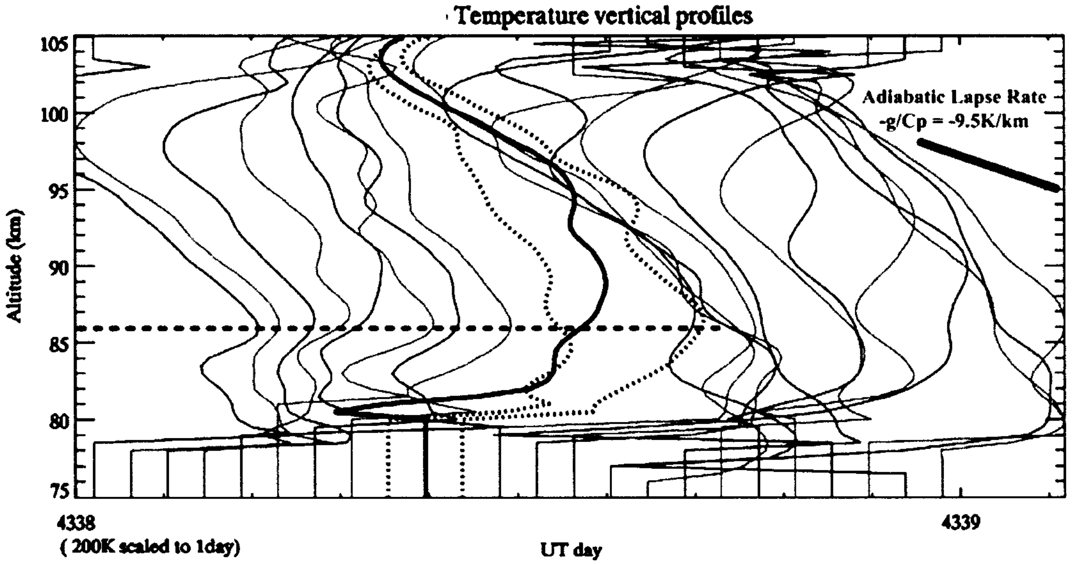

Figure 5.44 Time series of temperature vertical profiles for UT day 338, 2004. The black solid line is the vertical profile at 09:30UT with strong inversion layer extended to a large altitude region from 80km to 100km. The temperature profiles at neighboring hours are shown with black dash lines. The light blue dash line at 86km denotes the peak altitude of temperature inversion which persisted for most of night.

Shown in figure 5.45 are the vertical profiles of temperature observed by our lidar (blue solid line) and SABER (red dot line) at ~07:00UT and ~12:00UT. We can see that at ~07:00UT, SABER observed a strong temperature inversion with amplitude of ~30 K near 90km, whereas lidar observed a ~20 K temperature inversion near 87 km. The different amplitudes and altitudes of the temperature inversions are most likely due to 5° longitude difference of the observation locations. However, the observed profiles at ~12:00UT show very good agreement between lidar and SABER even though there is still 5° longitude difference of the observation locations, indicating that the large regional or global effects dominate both observed profiles.

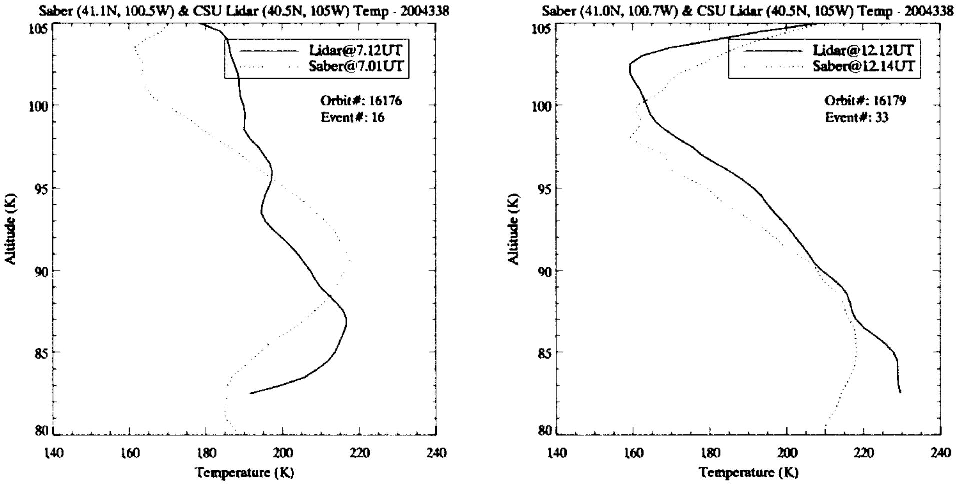

Figure 5.45 Vertical profiles of temperature observed by CSU sodium lidar (Blue solid line) and TIMED/Saber satellite (red dot line) at ~07:00UT (left panel) and ~12:00UT (right panel)

Corresponding to the temperature plots shown in figure 5.46(a), we also plot the vertical profiles of zonal wind and meridional wind from 08:30 to 11:30UT for UT day 338, 2004, respectively shown in figures 5.46(b) and (c). The strong wind shear of ~15 m/s/km in zonal component between 92 km and 100 km without clear downward progression and ~20 m/s/km in meridional component between 89 km and 96 km with clear downward progression can be seen. The large wind shear and large temperature gradient near adiabatic lapse rate indicates possible atmospheric instability at this altitude range. The formation of strong temperature inversion is also possibly related to the atmospheric instability and gravity wave breaking with a mechanism similar to that of Liu and Hagan [1998] depicted earlier in figure 5.17.

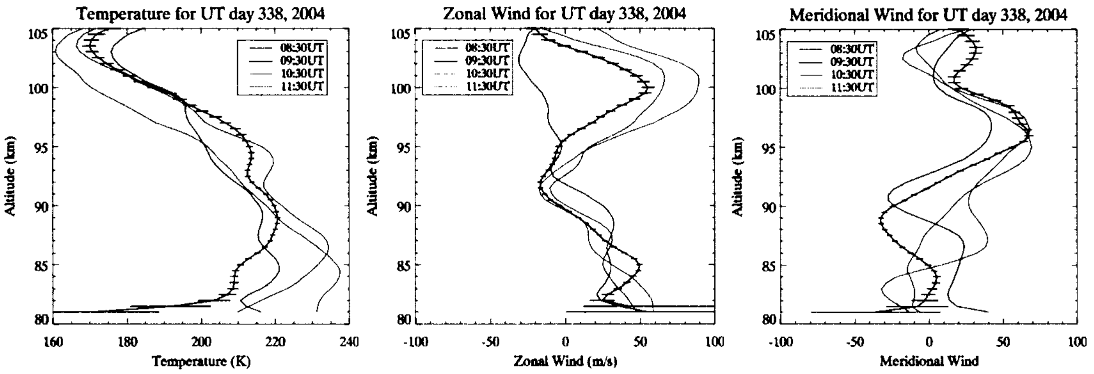

Figure 5.46 Vertical profiles of temperature (a), zonal wind (b), and meridional wind (c) at 08:30, 09:30, 10:30, and 11:30UT.

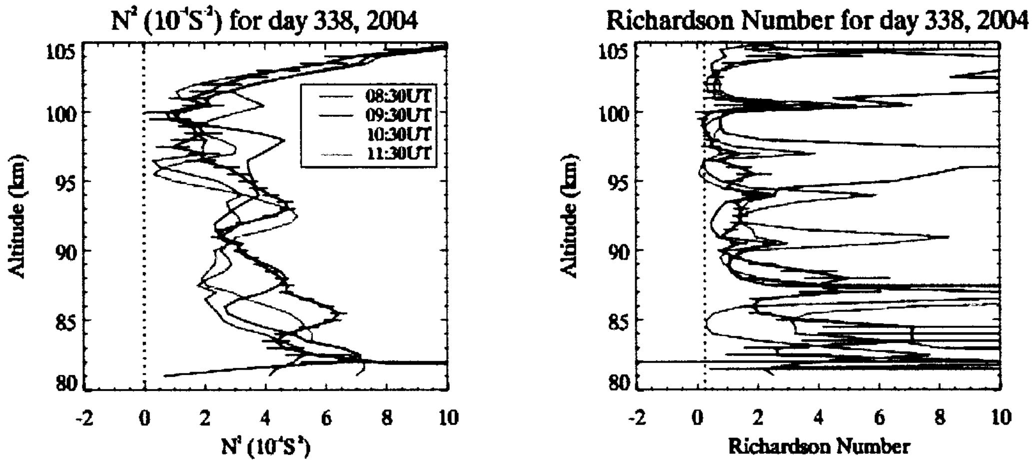

Figure 5.47 Vertical profiles of corresponding Brunt-Vasialla frequency square and Richardson number at 08:30, 09:30, 10:30, and 11:30UT.

To show the possible atmospheric instability, we plot the square of Brunt-Vasialla frequency and Richardson number in figure 5.47. we can see that the square of Brunt-Vasialla frequency is approaching 0 line (marked by black dot line in the left panel of figure 5.47), but still larger than 0, near 100km at 09:30UT and near 95 km at 10:30 and 11:30UT. However, the vertical profiles of Richardson number in the right panel of figure 5.47 shows that Richardson number is less than 0.25 (the atmosphere is dynamically unstable) at 09:30UT between 98.5 and 100 km and at 10:30 and 11:30UT between 95 km and 96.5 km. These plots were derived from hourly mean profiles; at a shorter time scale, both N^2 and Richardson number will be smaller. Once a gravity wave propagates into this region of atmosphere, it becomes dynamically unstable and tends to break. The breaking wave will deposit some of the energy and momentum of the wave packet into mean flow. Therefore, the gravity wave interactions with background and tidal wind could induce a large temperature inversion layer and also a strong wind shear. Since the phases of tidal waves progress downward typically with a speed of ~1 km/hour (~5 km/hour) for diurnal (semidiurnal), the temperature inversion due to gravity wave interaction with tidal waves should also have a phase speed of downward progression. The downward phase progression of the temperature inversion with a speed of ~2 km/hour is indeed seen in figure 5.44 and 5.46 after 09:30UT. This temperature inversion layer after 09:30UT showed downward progression with the amplitude modified by the interaction between gravity waves and tidal waves. In section 5.4.2, we will discuss the tidal day-to-day variability for this campaign and we will see that the temperature diurnal amplitude indeed increases by almost twice that in UT day 338 compared to the previous day.

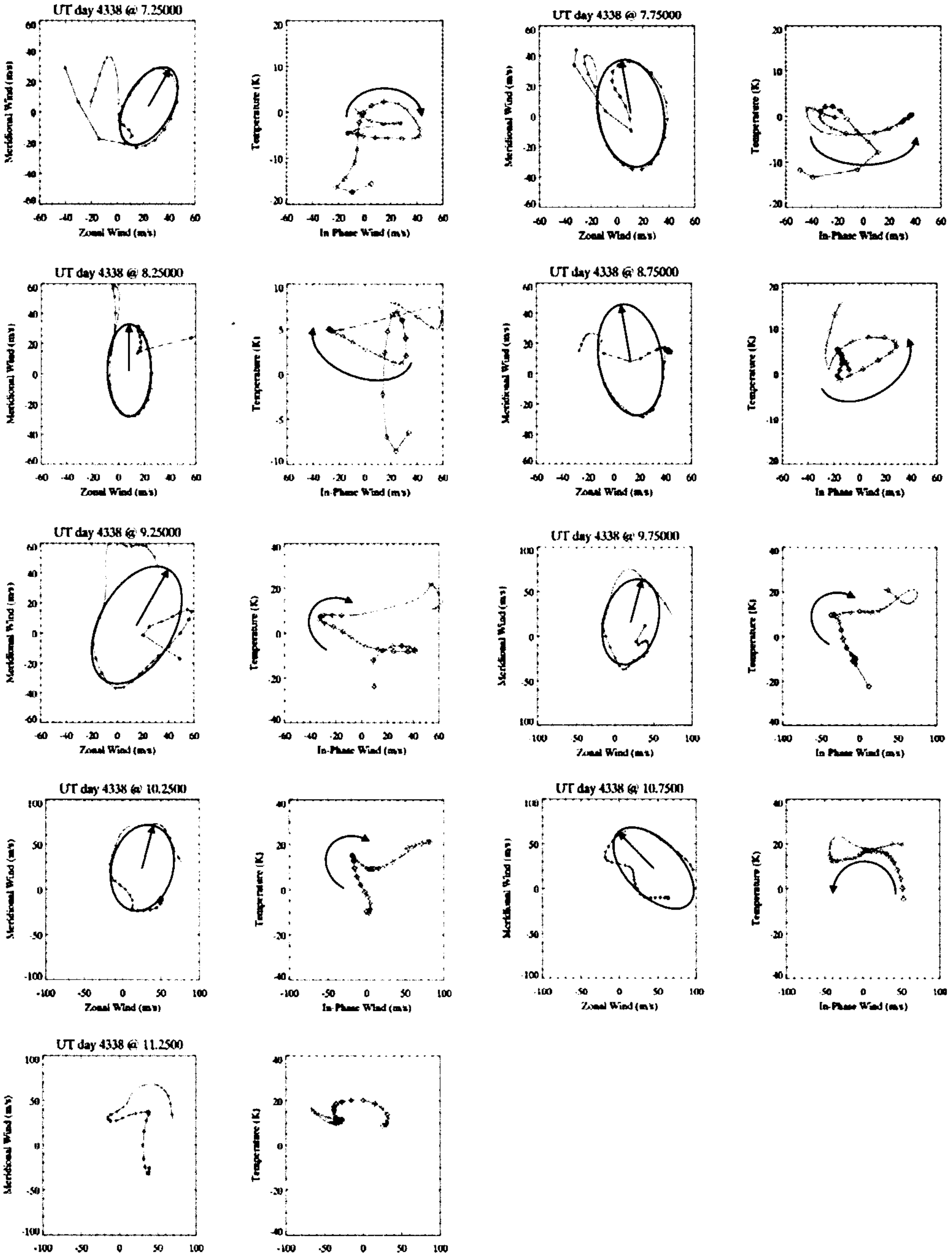

Figure 5.48 Hodographs of zonal wind vs. meridional wind and in-phase wind vs. temperature (30min averaged with diurnal mean removed) at UT 07:15, 07:45, 08:15, 08:45, 09:15, 09:45, 10:15, 10:45, and 11.15 for day 338, 2004. The ellipses are fitted curves, the black solid lines with arrows show the horizontal propagation direction of the wave, and the arcs with arrows show the rotation direction of in-phase wind vs. temperature. The colors from black to red denote that the altitudes increase from 84km to 100km.

Since our sodium lidar observes all three components, temperature, zonal wind, and meridional wind simultaneously, we can plot hodographs of zonal wind vs. meridional wind and in-phase wind vs. temperature to determine both horizontal and vertical propagation direction of a quasi-monochromatic inertial gravity wave that may play an important role in the described dynamic behavior. Shown in Fig. 5.48 are the hodographs from 07:25 to 11:25UT. Based on the fitted ellipses in the plots of zonal wind vs. meridional wind, along with the marked rotation direction in the plots of in-phase wind vs. temperature, one can determine the direction of the in-phase wind. According to the hodograph analysis for inertial gravity wave giving in Section 4.3.2, the wave should propagate upward if the (u′, v′) vector rotates clockwise with increasing altitude, and propagates in the positive x direction (0° ≤ azimuth angle < 180°, azimuth angle is the angle clockwise from True North) if (u′, T′) rotates clockwise with increasing altitude [Hu et al., 2002]. For example, the hodographs in figure 5.48 at UT 07:25, 08:25, 09:25, 09:75, and 10:25 show that the wave propagates upward and in the positive x direction (north or northeast ward). These rotations should be reversed for the wave propagating in the down direction, such as hodographs at UT 07:75, 08:25, 10:75 (upward and northwest ward). As shown in figure 5.48, we could clearly see that before 11:00UT, there is an inertial gravity wave propagating upward and northward, northeast, or northwest with the inertial period of 10-14hr. At the same time, the vertical profile of meridional wind between 08:30 and 11:30UT in figure 5.46(c) shows the strong northward winds are developing between 90 km and 95 km with the peak as large as 70 m/s near 95 km. It is also interesting to note that the propagating direction of the wave changes from 75° north of east at 10:15UT to 45° north of west at 10:45UT. During this period, the zonal wind profile in figure 5.46(b) at 10:30UT show a strong wind (~90 m/s near 100 km) and wind shear (~15m/s) above 95 km. By examining the zonal wind for both 09:30UT and 10:30UT, we find the zonal wind increases dramatically above 90 km with the peak value changing from 55 m/s to 90 m/s near 100km. The dramatic change of zonal wind could cause a change in apparent horizontal propagation direction of the wave. Since there is no clear indication of wave activity in hodographs at 11:15UT, we could conclude that this wave actually disappears after 11:00UT. It is possible that the waves break in the region between 95 km and 100 km around 11:00 UT. Looking at the vertical profile of Richardson number at 10:30UT in figure 5.47, we see a dynamically unstable region near 96km with Richardson number less than 0.25. This could be indicative of the wave breaking via dynamic instability. Wave breaking could cause the dynamic cooling in the breaking region (95-100 km) and turbulence heating below (below 95 km) and further increase the inversion layer and negative temperature gradient above [Werne and Fritts, 1999; Liu et al., 1998]. Therefore, the temperature inversion layer in the night of UT day 338 is likely related to the interactions of gravity waves and tides, and the strong amplitude of this inversion are likely connected with strong tidal structures with downward phase progression.

Since we have nearly 80 hours of data for this winter campaign, we are able to do a spectrum analysis to determine the predominant periods of the waves. Shown in figure 5.49 are the contour plots of Lomb normalized power for temperature (top panel), zonal wind (middle panel), and meridional wind (bottom panel) based on the dataset with the resolutions of 1-hr and 2-km (4km) for night (day). The contour lines are corresponding to 0.5% probability resulting from random noise marked as white solid line and 5% marked as white dot line.

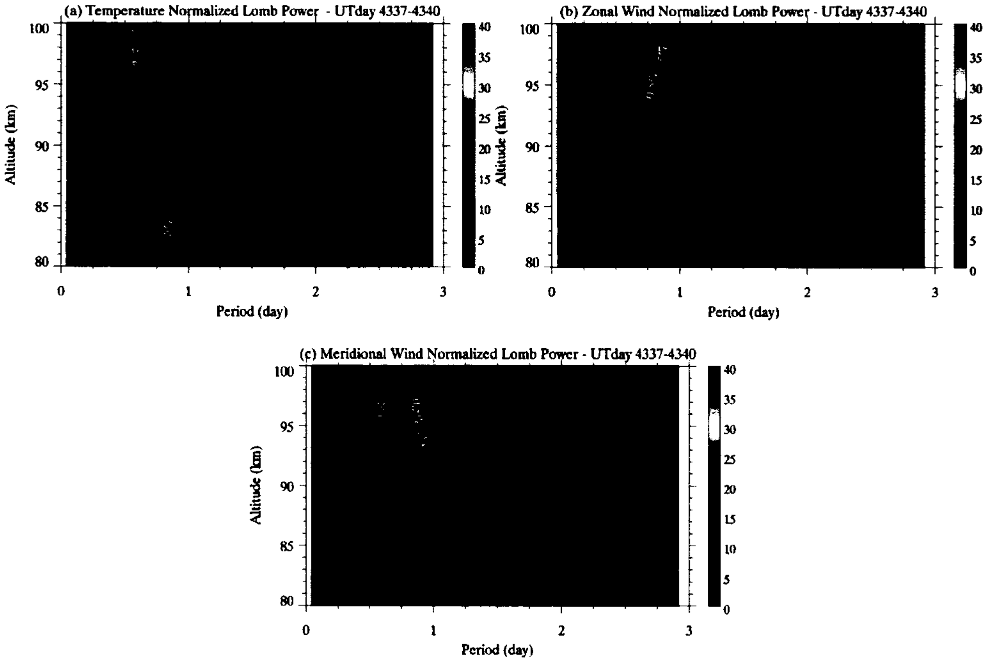

Figure 5.49 Contour plots of Lomb normalized power for temperature (a), zonal wind (b), and meridional wind (c) based on the dataset with the resolutions of 1hr and 2km (4km) for night (day) shown with contour lines corresponding to 0.5% (white dot line) and 5% (white solid line) probability resulting from random noise.

In addition to significant powers for diurnal and semidiurnal oscillations in all three components, we also see some other periods with significant powers, such as 9-hr period from 82 km to 96 km, 13-hr period below 85 km and above 95 km, 22-hr period below 85 km respectively in the temperature component, and 13-hr period above 95 km and 18-hr period above 83 km and quasi-1.5 day period below 85 km respectively in zonal wind component, and 13-hr period above 92 km and 18 above 90 km respectively in meridional wind component. The period of 13-hr with significant Lomb power observed in all three components above ~90 km are comparable to the inertial period we derived from the hodograph analysis for gravity waves in figure 5.48, suggesting that the inertial gravity waves with period of 10-14hr are persistent for most of the campaign. Another interesting point to note is that the altitude region where the period of 13-hr in Lomb contours appears with significant power in figure 5.49 is comparable to the altitude region where dynamic instability is observed in figure 5.46, suggesting that in the night of day 338, the inertial gravity waves with period ~13-hr very likely break in this region and deposit their momentum and energy into the flow, and furthermore modify the temperature and wind structures for that night. Some of the wave energy is also dissipated into three-dimentional turbulence [Werne and Fritts, 1999].

Since the temperature inversion was persistent for most of night in UT day 338, 2004, we should see it in the vertical profile of mean temperature. Shown in the figure 5.50 are the vertical profiles of mean temperature (top panel), mean zonal wind (middle panel), and mean meridional wind (bottom panel) averaged over UT day 338 (left panel) and the whole campaign from day 337 to 340 (right panel). We could clearly see the temperature inversion with amplitude of ~5 K between 81 and 90 km in the one-day mean temperature plot (top left panel) and amplitude of ~2 K between 82 and 88 km in the near four-day mean temperature plot (top right panel). At the same time, although the mean zonal winds are stable with ~25 m/s at the altitude region where the temperature inversion appears, the mean meridional winds vary with positive and negative wind shear in that region. There also exists a clear wave pattern with vertical wavelength of ~12 km and amplitude of ~6 m/s in the vertical profiles of mean meridonal wind. It is not clear what this pattern is. However, the mean wind directions of zonal and meridional components are eastward and southward respectively at most altitudes. Therefore, the directions of horizontal mean winds at most of altitudes are southeast.

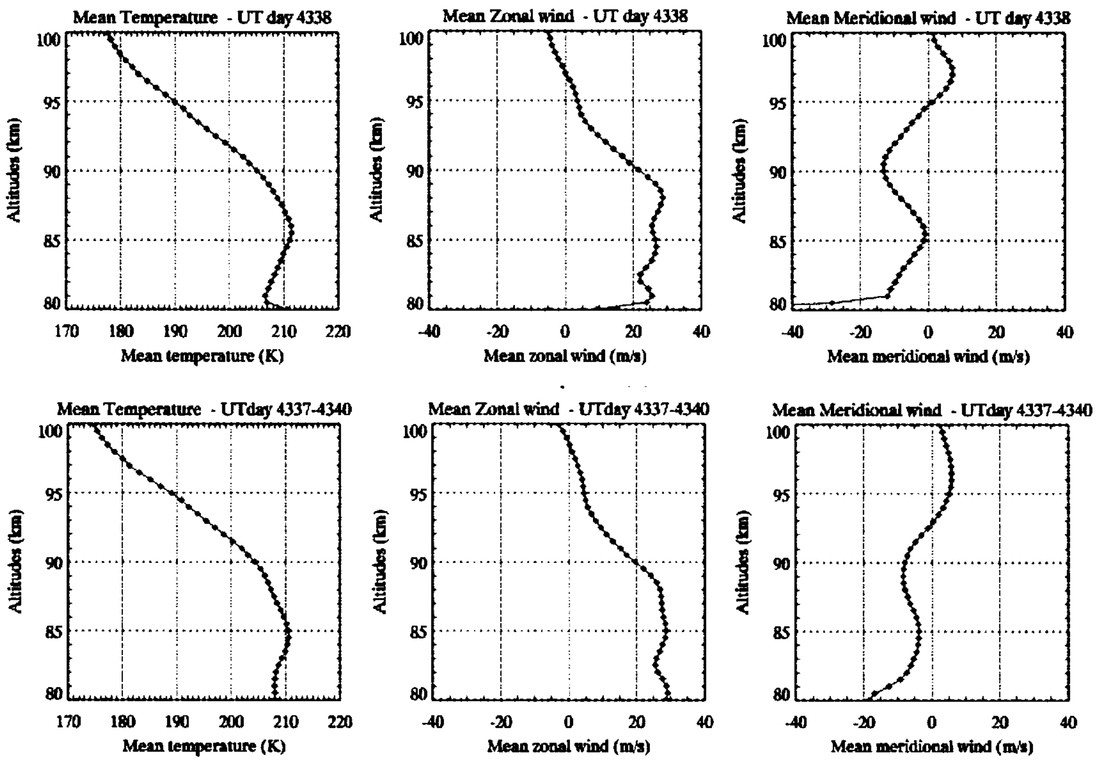

Figure 5.50 Vertical profiles of mean temperatures (left column), mean zonal wind (middle column), and mean meridional wind (right column) averaged over day 338, 2004 (top panel) and the whole campaign from 337 to 340, 2004 (bottom panel).

5.4.2 Tidal day-to-day variability

Since the strong temperature inversion layer observed in the night of UT day 338 is likely due to the tidal/gravity wave interactions, we should expect considerable day-to-day variability of tidal structure in this winter campaign. To access the tidal variability, we use the method discussed in section 5.1.2 to perform tidal fitting within a running 24-hr window centered at every hour for this near 80-hour dataset with resolutions of 1-hour and 2-km (4-km) for night (day). In this way, we investigate the time series change of tidal amplitudes and phases. Figure 5.51 presents the contour plots of variability observed by our lidar system in the winter campaign of December 2004 from UT day 337 to 340 with near 80 hour continuous observations. The diurnal (a, b, c) and semidiurnal (d, e, f) amplitudes (left panel) and phases (right panel) of temperature (a, d), zonal wind (b, e), and meridional wind (c, f) in the mesopause region are shown. As shown, the diurnal tidal amplitude of temperature dramatically increases in day 338 with maxima of ~10 K near 85 km persistent for most of night, whereas the semidiurnal tidal amplitude of temperature only slight increases in the day 338 with high amplitude of 10-15K persistent during the whole campaign, which indicates that the temperature inversion layer observed at night of day 338 is most likely due to the interactions between diurnal tide and gravity waves. By examining the tidal variability in zonal wind component, we find that the variability of diurnal amplitude suggest wave behavior with a phase speed of ~10 km/day progressing downward. This is consistent with the temperature diurnal amplitude being modulated by a planetary wave with a period longer than the duration of our campaign. The diurnal tidal amplitude with ~60 m/s is observed in the nighttime of day 339. However, the semidiurnal tidal amplitude of zonal wind has small variability with amplitude of less than 20 m/s below 95 km, and large variability with amplitude as strong as ~60 m/s near 100 km in the daytime of day 338. Unlike the tidal variability in the zonal wind component, the diurnal amplitude of meridional wind does not vary in a wavelike pattern, but increases more abruptly near 85-90 km starting from the daytime of day 338. However, the yellow maxima in the contour of semidiurnal amplitude of meridional wind moves upward with a speed of ~8 km/day and with a value more than 60 m/s above 95 km between daytime of 338 and nighttime of 339. This is nearly opposite to what we observed in the variability of diurnal amplitude in the zonal wind component. In addition to the considerable variability of tidal amplitudes, we find that the changes in the tidal phases for all three components are within 1-2hr at all altitudes, except that the semidiurnal phase of zonal wind varies considerably above 90 km in the day 339. The reason for the big diurnal enhancement in zonal and meridional wind components in UT day 339 is unclear at this time and requires further investigation.

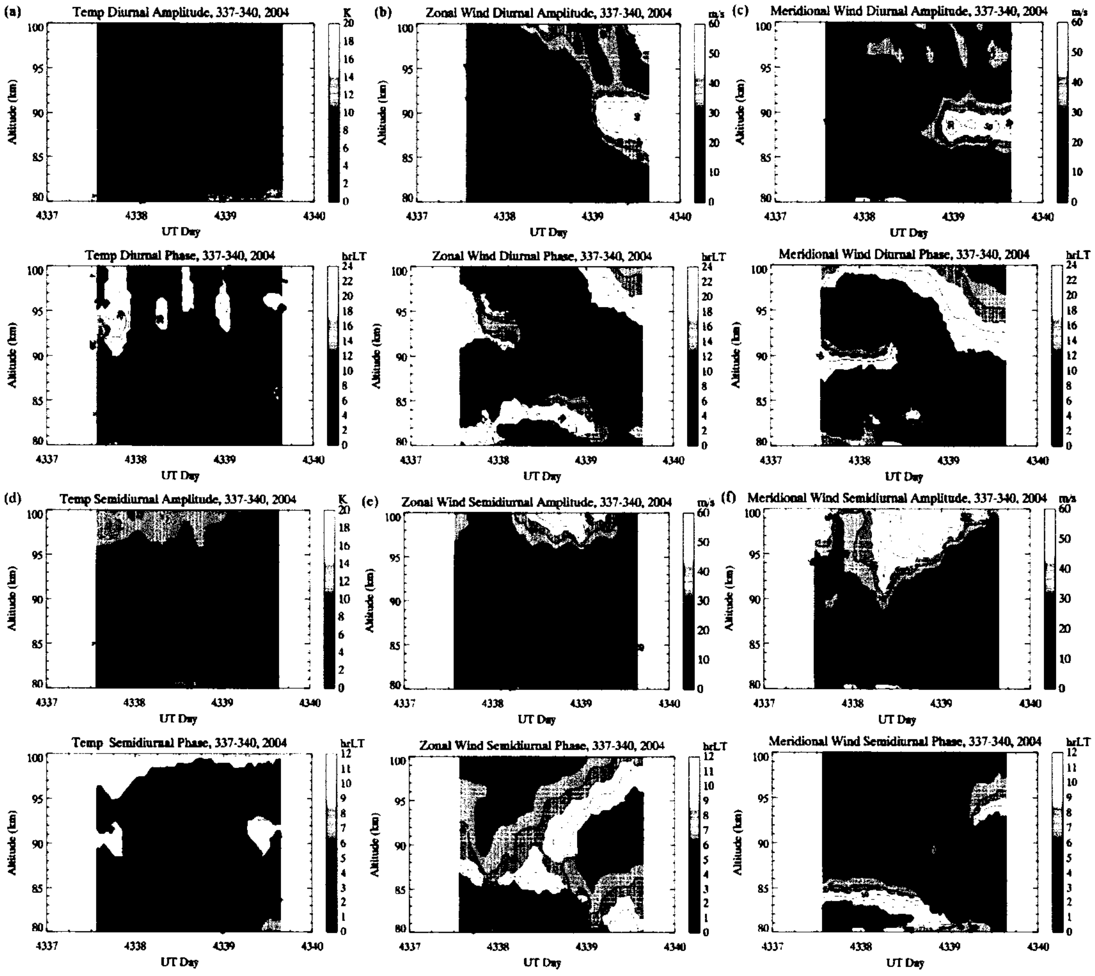

Figure 5.51 Contour plots of variability in diurnal (a, b, c) and semidiurnal (d, e, f) amplitudes (top) and phases (bottom) of temperature (a, d), zonal wind (b, e), and meridional wind (c, f) during the winter campaign in December 2004.

Shown in figure 5.52 is the contour plot of variability of diurnal mean temperature. We can clearly see that the temperature inversion exists in the diurnal mean profile for the whole day of 338 with amplitude of ~5 K and slight downward progression with speed of 2 km/day.

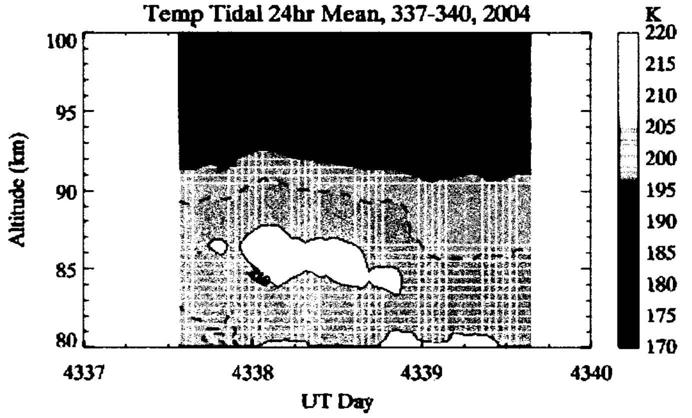

Figure 5.52 Variability of diurnal mean temperature

5.4.3 Summary

The temperature inversion layer in the mesosphere is observed to reach amplitude as large as ~50 K and persist for most of the night in day 338 during winter 2004 campaign. This is most likely due to the interactions between gravity waves and tides as well as the background flow.

The observed evolution of the temperature inversion is somewhat different. Unlike those reported in the literature, this temperature inversion layer starting at the beginning of night in day 338 remains constant near 86km without clear downward phase progression related to tidal waves. However, after 9:30 UT, it extends to most of altitudes of the sodium layer in the late night with large amplitude, and indeed propagates downward with phase speed comparable to that of tidal waves. The temperature inversion exists even in the mean temperature profiles averaged over day 338 and the whole campaign with amplitude of ~5K and ~2K respectively.

The observed considerable tidal day-to-day availability with tidal amplitude dramatically increasing in day 338 further suggests the existence of strong wave-wave interactions. The vertical profiles of square of the Brunt-Vasialla frequency and Richardson number shows that instability regions are developing in the nighttime of day 338. Hodograph analysis suggests an inertial gravity wave with period of ~13hr is active in the mesopause region. All these are evidence for a tidal/gravity wave interaction.

Reference:

Bills, R. E., and C. S. Gardner, Lidar observations of the mesopause region temperature structure at Urbana, *J. Geophys. Res.*, 98, 1011-1021, 1993.

Dickinson, R. E., E. C. Ridley, R. G. Roble, A 3-Dimensional General-Circulation Model of the Thermosphere, *J. Geophys. Res.*, 86, 1499-1512, 1981.

Fritts, D. C., and T. J. Dunkerton, A quasi-linear study of gravity wave saturation and self acceleration. *J. Atmos. Sci.* 41, 3272 – 3289, 1984.

Fritts, D. C., and R. A. Vincent, Mesospheric momentum flux studies at Adelaide, Australia: Observations and a gravity wave/tidal interaction model, *J. Atmos. Sci.*, 44, 605–619, 1987.

Fritts, D. C., and M. J. Alexander, Gravity wave dynamics and effects in the middle atmosphere, *Rev. Geophys.*, 41(1), 1003,doi:10.1029/2001RG000106, 2003.

GSWM Website, High Altitude Observatory, National Center for Atmospheric Research, March 17, 2004, < http://web.hao.ucar.edu/public/research/tiso/gswm/gswm.html>

Hagan, M. E., and R. G. Roble, Modeling diurnal tidal variability with the National Center for Atmospheric Research thermosphere-ionosphere-mesosphere-electrodynamic general circulation model, *J. Geophys. Res.*, 24,869-24,882, 2001.

Hauchecorne, A., M. L. Chanin, and R. Wilson, Mesospheric temperature inversion and gravity wave dynamics, *Geophys. Res. Lett.*, 14, 935-939, 1987.

LeLong, M. P., and T. J. Dunkerton, Inertia–Gravity Wave Breaking in Three Dimensions. Part I: Convectively Stable Waves, *J. Atmos. Sci.,* 55 (15), 2473 – 2488, 1998.

Liu, H., and M. E. Hagan, Local heating/cooling of the mesosphere due to gravity wave and tidal coupling, *Geophys. Res. Lett.*, 25(15), 2941–2944, 1998.

Liu, H., Temperature changes due to gravity wave saturation, *J. Geophys. Res.*, 105(D10), 12,329-12,336, 2000.

Liu, H.-L., Jr., Mesospheric planetary waves at northern hemisphere fall equinox, *Geophys. Res. Lett.*, 28(9), 1903–1906, 2001.

Lomb, N.R. 1976, *Astrophysics and Space Science*, vol. 39, pp. 447–462.

Lubken, F. –J, W. Hillert, G. Lehmacher, U. von Zahn, M. Bittner, D. Offermann, F. Schmidlin, A. Hauchecorne, M. Mourier, and P. Czechowsky, Intercomparison of density and temperature profiles obtained by lidar, ionization gauges, falling spheres, datasondes, and radiosondes, during the DYANA campaign, *J. Atmos. Sol. Terr. Phys.*, 56, 1969-1984, 1994.

Meriwether, J. W., C. S. Gardner, A review of the mesosphere inversion layer phenomenon, *J. Geophys. Res.*, 105, 12,405-12416, 2000.

Mertens, C. J., M. G. Mlynczak, M. Lopez-Puertas, P. P. Wintersteiner, R. H. Picard, J. R. Winick, L. L. Gordley, and J. M. Russell III, Retrieval of mesospheric and lower thermospheric kinetic temperature from measurements of CO2 15-um Earth limb emission under non-LTE conditions, *Geophys. Res. Lett.*, 28, 1391-1394, 2001.

Meyer, C. K., and J. M Forbes, A 6.5-day westward propagating planetary wave: Origin and characteristics, *J. Geophys. Res.*, 26,173-26,178, 1997.

Meyer, C. K., Gravity Wave-Tidal and Gravity Wave-Planetary Wave Interactions in the Mesosphere and Lower Thermosphere, *PhD Dissertation*, Univ. of Colo., 1998.

Nappo, C. J., An Introduction to Atmospheric Gravity Waves, *Intern. Geophy. Ser.*, vol. 85, p120, 2002.

Norton, W.A. and J. Thuburn, The two-day wave in a middle atmosphere GCM, *Geophys. Res. Lett.*, 23, 2113-2116, 1996.

Palo, S. E., R. G. Roble, M. E. Hagan, Middle atmosphere effects of the quasi-two-day wave determined from a General Circulation Model, *EARTH PLANETS AND SPACE*, 51 (7-8): 629-647 1999.

Press, W. H., S. A. Teukolsky, W. T. Vetterling, and B. P. Flannery, *Numerical Recipes in C: The Art of Scientific Computing*, Second Edition, Cambridge University Press, 1997.

Roble, R., E. C. Ridley, A Thermosphere-Ionosphere-Mesosphere-Electrodynamics General Circulation Model (TIME-GCM), *Geophys. Res. Lett.*, 21, 417-420, 1994.

Saber Website, Langley Research Center, National Aeronautics and Space Administration, February 27, 2005, <http://saber.larc.nasa.gov/>

Salby, M.L. and P.F. Callaghan, Seasonal amplification of the 2-day wave: Relationship between normal mode and instability, *J. Atmos. Sci.*, 58, 1858-1869, 2001.

Salby, M., F. Sassi, P. Callaghan, D. Wu, P. Keckhut, and A. Hauchecorne, Mesospheric inversions and their relationship to planetary wave structure, *J. Geophys. Res.*, 107(D4), 4041, doi:10.1029/2001JD000756, 2002.

Salby, M.L. and P.F. Callaghan, Dynamics of the 2-day wave in a nonlinear model of the middle and upper atmosphere, *J. Geophys. Res.*, 108, doi:10.1029/2003JD003648, 2003.

Sassi F., R. R. Garcia, B. A. Boville, and H. Liu, On temperature inversions and the mesospheric surf zone, *J. Geophys. Res.*, 107, 4380, doi:10.1029/2001JD001525, 2002.

Schmidlin, F. J., Temperature inversions near 75km, *Geophys. Res. Lett.*, 3, 173-176, 1976.

She, C. Y., H. Lafiti, J. R. Yu, R. J. Alvarez II, R. E. Bills, and C. S. Gardner, Two-frequency lidar technique for mesospheric Na temperature measurements, *Geophys. Res. Lett.*, 17, 929-932, 1990.

She, C. Y., J. R. Yu, and H. Chen, Observed thermal structure of a midlatitude mesopause, *Geophys. Res. Lett.*, 20, 567-570, 1993.

She, C. Y., Initial full-diurnal-cycle mesopause region lidar observations: Diurnal-means and tidal perturbations of temperature and windsover Fort Collins, CO (41N, 105W), PSMOS 2002, *J. Atmo. Solar-Terr. Phys.*, 66, 663-674, 2004.

She, C. Y., T. Li, R. L. Collins, T. Yuan, B. P. Williams, T. Kawahara, J. D. Vance, P. Acott, D. A. Krueger, H.-L. Liu and M. E. Hagan, Long-period lidar observation of mesopause region temperature and wind vector over Ft. Collins, CO (40°N, 105°): Study of tidal-period perturbation and variability, *Geophys. Res. Lett.*, 31, L24111, doi:10.1029/2004GL021165, 2004.

States, R. J., and C. S. Gardner, Influence of the diurnal tide and thermosphere heat sources on the formation of mesospheric temperature inversion layers, *Geophys. Res. Lett.*, 25, 1483, 1998.

Taylor, M. J., Jr., H.-L. Liu, C. Y. She, L. C. Gardner, R. G. Roble, and V. Vasoli, Large amplitude perturbations in mesospheric OH Meinel and 87-km Na lidar temperatures around the autumnal equinox, *Geophys. Res. Lett.*, *28*(9), 1899–1902, 2001.

Thayaparan, T., W. K. Hocking and J. MacDougall, Observational evidence of tidal/gravity wave interaction using the UWO 2MHz radar, *Geophys. Res. Lett.*, 22, 373-376, 1995.

Thayaparan, T, W. K. Hocking1, J. MacDougall1, A. H. Manson, C. E. Meek Simultaneous observations of the 2-day wave at London (43°N, 81°W) and Saskatoon (52°N, 107°W) near 91 km altitude during the two years of 1993 and 1994, Ann. Geophysicae, 15, 1324-1339, 1997.

Walterscheid, R. L., Inertio-gravity wave induced accelerations of mean flow having an imposed periodic component: Implications for tidal observations in the meteor region, *J. Geophys. Res.*, 86, 9698–9706, 1981.

Walterscheid, R. L., and G. Schubert, Nonlinear evolution of an upward propagating gravity wave: Overturning, convection, transience and turbulence, *J. Atmos. Sci.*, 47, 101-125, 1990.

Werne and Fritts, Stratified shear turbulence: Evolution and statistics, *Geophys. Res. Lett.*, 26 (4): 439-442, 1999.

Whiteway, J. A., I. Carswell, and W. E. Ward, Mesospheric temperature inversions with overlaying nearly adiabatic lapse rate: An indication of well-mixed turbulent layer, *Geophys. Res. Lett.*, 22, 1201-1204, 1995.

Chapter 6: Conclusion and future work

The CSU sodium lidar system at Fort Collins, CO (40.6N, 105W), after a decade of mesopause temperature observation [She et al., 2000], was upgraded in 1999 from a one-beam system to a two-beam system, capable of simultaneous and continuous observations of mesopause region temperature, zonal wind, and meridional wind, over full diurnal cycles, weather permitting. Regular observations in this mode of operation began May, 2002. By now, the sodium lidar has completed 3 years of simultaneous observations of temperature and horizontal wind over full diurnal cycles, weather permitting. Using these datasets, we can study not only the seasonal variations of tides [Yuan, 2004], but also the tidal day-to-day variability [She, et al., 2004] as well as the effect of planetary waves (PW) and gravity waves (GW).

In this dissertation, we described the details of the CSU sodium lidar system setup, and provided an overview of the lidar transmitter subsystem, receiving subsystem, and control and timing electronics subsystem in chapter 2. Atomic sodium hyperfine spectrum, the lidar equation for a sodium lidar system, and temperature and wind ratios as well as 2-D calibration curves were qualitatively discussed in chapter 3. Chapter 4 presented a brief review of the atmospheric solar tides, planetary waves, and gravity waves, as well as their interactions.

Chapter 5 presented several multiple-day continuous and simultaneous observations of dynamic variability in the mesosphere and lower thermosphere with very high temporal resolution (15 minutes for nighttime and 30 minutes for daytime) and vertical resolution (2km). Firstly we presents the dramatic tidal day-to-day variability based on our longest campaign (14 day duration with 9-day continuous observation) near fall equinox, then followed by the observation of two-day wave activities with considerable tidal day-to-day variability in August of three consecutive years. Finally, the observation of strong winter temperature inversion is discussed along with the associated tide-gravity wave interactions.

Our longest campaign near fall equinox revealed dramatic day-to-day variations in diurnal and semidiurnal tidal amplitudes and a large increase (by factors of ~2) in diurnal (as large as 20K) and semidiurnal (as large as 24K) amplitudes in days 266-268. In addition to the tidal periods, spectral analyses identified a quasi 1.5-day, a 3-day and a 5-day planetary wave. The origins and characteristics of these waves are not presently known. Spectral analyses also identified periods of ~20, ~14 and ~10 hours, which are believed to be the products of nonlinear interactions between tides and PW. TIME-GCM simulation demonstrated that the presence of a Quasi-Stationary Planetary Wave can introduce strong short term variability in tides, due presumably to tide-planetary wave interaction. The temperature, zonal wind, and meridional wind tides (diurnal and semi-diurnal) all increase and decrease rapidly as a result of the QSPW perturbations. The interaction also produces an inversion layer between 90 and 100 km at certain longitude, though not as strong as that observed by the lidar. Lidar observed temperature and SABER overpass temperatures over Fort Collins showed very good agreement on both UT day 267 and 268. SABER observations also revealed that the inversion covered over a global region, suggesting the presence of tide/planetary wave interaction. However, tide/gravity wave interactions are still needed to account for the more than 2-fold increase in tidal amplitudes. Our examination of both unusual nights of day 267 and 268 suggests that the tidal/gravity wave interactions are more important for tidal amplitude enhancement in the night of day 267, whereas the tidal/planetary interactions play more important roles on the tidal increase in the night of day 268.

Diagnostic studies of three 80 hour plus campaigns, respectively in UT days 221-224 (2002), days 225-229 (2003), and days 225-229 (2004), showed significant quasi-two-day wave activities as well as considerable tidal day-to-day variability observed by CSU sodium lidar system. Comparing the quasi-two-day wave amplitudes in temperature observation between the CSU lidar and TIMED/SABER for all three campaigns showed very good agreement. The Quasi-two-day waves observed by both instruments are consistent with UGAMP-GCM model prediction [Norton and Thuburn, 1996]. The quasi-two-day wave observed by both SABER and lidar in August of years 2002, 2003, and 2004 with wave amplitude in August 2003 weaker than that in both Augusts of 2002 and 2004 indicates possible modulation by the Quasi-Biannual Oscillation (QBO) on the quasi-two-day wave amplitude.

The mesospheric temperature inversion layer, with inversion amplitude gradually increased to as large as ~50 K and persisted for most of night in day 338 observed by our lidar during winter 2004 campaign is most likely due to the interactions between gravity waves and tides, as well as background flow. Unlike what has been reported in the literature, this temperature inversion layer starting at the beginning of night in day 338 remains near 86km without clear downward phase progression related to tidal waves. However, after 9:30 UT (02:30am LT), it extended to most altitudes of the sodium layer in the late night with large amplitude, and indeed propagated downward with phase speed comparable to that of tidal waves. The temperature inversion exists even in the mean temperature profiles averaged over day 338 and the whole 3-day campaign with amplitude of ~5K and ~2K, respectively. The observation of considerable tidal day-to-day availability with tidal amplitude dramatically increasing in day 338 further suggests the existence of strong wave-wave interactions. The vertical profiles of square of the Brunt-Vaisala frequency and Richardson number showed that instability regions were developing in the nighttime of day 338. Hodograph analysis suggests an inertial gravity wave with period of ~13 hr is active in the mesopause region. All of these findings support the hypothesis of a tidal/gravity wave interaction.

Atmospheric instabilities were investigated in each case to help understand tide-GW and tide-PW interactions. In General, we found that tidal waves and planetary waves themselves are unable to cause local atmospheric instability without the superposition of short scale gravity waves, consistent with earlier observations [Fritts et al., 1997; Hecht et al., 1997; Li et al., 2005].

With all these examples shown in chapter 5, we have demonstrated the power of multiple-day continuous and simultaneous observations of temperature, zonal and meridional winds. These observations were possible (only) at CSU since May 2002.

These data revealed the richness in dynamical interactions in the MLT region. Various scenarios of wave-wave interactions were prior considered only in model studies. These include tidal variability, short-period planetary waves, as well as tide-gravity and tide-planetary wave interactions. The combination of high-resolution local observations and global satellite observations, which often reveal scenarios beyond expectation, further motivate new synergistic studies and model simulations. Indirectly, these realistic studies will provide constraints on and help to evaluate gravity wave parameterization schemes that are required for any general circulation model.

Initial comparison studies between observations and modeling of the tidal day-to-day variability are reported in this dissertation. But this beginning is neither sufficient nor extensive enough to cover the broad and still largely little understood field of tidal day-to-day variability. Further studies can be made in many data sets employed in this thesis, as well as in other data sets already acquired. Therefore,in future work we plan to pursue the variability studies with the combination of lidar observations and modeling. CSU sodium lidar will achieve better day-night datasets once the new big telescopes with 4.6 times aperture are operational. We anticipate more long-period multiple-day observations allowing a more extensive study on the tidal day-to-day variability. These lidar observations will be compared with TIMED/SABER observed global temperature tidal structure and variability and TIDI observed global wind tidal structure and variability, as well as data from other ground-based instruments, such as radars in different locations. On the theoretical side, we would like to work with colleagues at HAO/NCAR, to further and diagnose the TIME-GCM simulation and the mesoscale two-dimensional gravity wave model, in order to better identify the mechanisms of the tidal day-to-day variability and to explain the variability in the observations.

In a broader perspective, we hope to engage other modeling groups as well, and to get them interested and excited about the unique data sets the CSU lidar has collected. Once the larger telescope has been installed in the lidar observatory, limited observations vertical flux of horizontal momentum will then be possible in winter night when the Na layer is thicker and more abundant. The momentum flux measurements will provide quantification of gravity wave activities and the extent of their interactions with background mean flow and tide.

Reference:

Fritts, D. C., J. R. Isler, J. H. Hecht, R. L. Walterscheid, and Ø. Andreassen, Wave breaking signatures in OH airglow and sodium densities and temperatures: 2. Simulation of wave and instability structures, J. Geophys. Res., 102, 6669– 6684, 1997.

Hecht, J. H., R. L. Walterscheid, D. C. Fritts, J. R. Isler, D. C. Senft, C. S. Gardner, and S. J. Franke, Wave breaking signatures in OH air-glow and sodium denstities and temperatures. 1: Airglow imaging, Na lidar, and MF radar observations, J. Geophys. Res., 102, 6655– 6668, 1997.

Li, T., C. Y. She, B. P. Williams, T. Yuan, R. L. Collins, L. Kieffabar, and A. Peterson, Concurrent OH imager and sodium temperature/wind lidar observation of localized ripples over Northern Colorado, *J. Geophys. Res.*, in press, 2005.

Norton, W.A. and J. Thuburn, The two-day wave in a middle atmosphere GCM, *Geophys. Res. Lett.*, 23, 2113-2116, 1996.

She, C. Y., S. S. Chen, Z. L. Hu, J. Sherman, J. D. Vance, V. Vasoli, M. A. White, J. R. Yu, and D. A. Krueger, Eight-year climatology of nocturnal temperature and sodium density in the mesopause region (80 to 105 km) over Fort Collins, CO (41oN, 105oW), *Geophys. Res. Lett.*, 27, 3289 – 3292, 2000.

She, C. Y., T. Li, B. P. Williams, T. Yuan, and R. H. Picard, Concurrent OH imager and sodium temperature/wind lidar observation of a mesopause region undular bore event over FortCollins/Platteville, Colorado, *J. Geophys. Res.*, 109, D22107, doi:10.1029/2004JD004742, 2004.

Yuan, T., Seasonal variations of Diurnal and semidiurnal tidal-period perturbations in mesopause region temperature and zonal and meridional winds above Ft. Collins, CO (40°N, 105°W) based on Na-Lidar observation over full diurnal cycles, *PhD Dissertation*, Colorado State University, 2004.